

STUDY OF STRUCTURAL AND MAGNETIC CHARACTERISTICS OF Cr SUBSTITUTED Fe-BASED NANOCRYSTALLINE ALLOYS

(Ph.D. research works have been performed under sandwich program with Uppsala University, Sweden)

Ph. D. Thesis

By

MD. SULTAN MAHMUD



**DEPARTMENT OF PHYSICS
KHULNA UNIVERSITY OF ENGINEERING AND TECHNOLOGY
KHULNA-9203, BANGLADESH
APRIL-2008**

Study of Structural and Magnetic Characteristics of Cr Substituted Fe-based Nanocrystalline Alloys

BY

MD.SULTAN MAHMUD

Roll No: 0155701

Session: 2001-2002

A THESIS SUBMITTED TO THE DEPARTMENT OF PHYSICS,
KHULNA UNIVERSITY OF ENGINEERING & TECHNOLOGY, KHULNA-9203
IN PARTIAL FULFILMENT OF THE REQUIREMENT FOR THE DEGREE OF
DOCTOR OF PHILOSOPHY



DEPARTMENT OF PHYSICS
KHULNA UNIVERSITY OF ENGINEERING & TECHNOLOGY
KHULNA-9203, BANGLADESH

APRIL-2008

DECLARATION

This is to certify that the thesis work entitled as “**Study of Structural and Magnetic Characteristics of Cr Substituted Fe-based Nanocrystalline Alloys**” has been carried out in partial fulfillment of the requirement for Ph.D. degree in the department of Physics, Khulna University of Engineering & Technology, Khulna-9203, Bangladesh. The above research work or any part of this work has not been submitted anywhere for the award of any degree or diploma. No other person’s work has been used without due acknowledgement.

1. Supervisor

Candidate

Prof. Dr. S. S. Sikder

(Md. Sultan Mahmud)

2. Joint-Supervisor

Dr. A.K.M. Abdul Hakim

External Examiners:

- 1. Professor Dr. Per Nordblad**
Department of Engineering Sciences
Uppsala University, Uppsala, Sweden
- 2. Professor Dr. G. M. Bhuiyan**
Department of Physics
University of Dhaka

Acknowledgements

I have had a lot of help with this thesis work from many individuals in various selfless ways. I take this opportunity here to express my gratitude.

It is a great pleasure to express my deepest sense of gratitude and sincere appreciation to my reverend supervisors Dr. S. S. Sikder, Professor of Physics, Khulna University of Engineering & Technology, Khulna and Dr. A. K. M. Abdul Hakim, Chief Engineer, Materials Science Division, Atomic Energy Centre, Dhaka for their scholastic supervision, erudite discussion, invaluable suggestions and constructive guidance through the progress of this research work. They were always ready to provide a lucid explanation of the different concepts involved. Their critical reading of the script and subsequent corrections are much appreciated. Any mistakes that remain are of course mine.

I am indebted to Dr. M. Ali Asgar, Professor, Rashid Chair (Ex.), BUET, Dr. Md. Mahbub Alam, Professor, Department of Physics, KUET, Dr. Fouzia Rahman, Professor, Department of Mathematics, KUET and Dr. Feroz Alam Khan, Professor, Department of Physics, BUET for their help, suggestion and inspiration.

I am really grateful to the International Programme for Physical Sciences (IPPS), Uppsala University, Sweden for their financial support and giving me facilities to do my research works in the Angstrom laboratory, Sweden. My thanks are due to Prof. Peter, Svedlindh and other researchers, Engineering Physics Department, Angstrom Laboratory, Uppsala University, Sweden for their sincere help and cooperation for using SQUID magnetometer for low temperature measurements of my research works.

I would like to thank Prof. Chau, Centre for Materials Science (CMS), Vietnam National University, Hanoi for his valuable suggestions when I worked in his laboratory. My special thanks are for Mr. The, Mr. Tho, Mr. Hoa and many other research fellows of the Vietnam National University for their help for preparing my samples and also for doing experimental works in their laboratory. I would like to extend my thanks to Dr. N. H. Dan, Vietnam National Research institute for his help for performing high temperature measurements with VSM in the laboratory.

I am very much grateful to the Director of Atomic Energy Centre, Dhaka (AECD) for his kind permission to do experimental works at the laboratory of Materials Science

Division, Atomic Energy Centre, Dhaka. My heartiest thanks are for Dr. Dilip Kumar Saha, Ms. Shireen Akhter, Principal Scientific Officer, Materials Science Division, Atomic Energy Centre (AEC), Dhaka for their suggestions and encouragement when I worked in the Materials Science Division's laboratory.

I am extremely grateful to Ms. Sk. Manjura Hoque, Senior Scientific Officer, Materials Science Division, (AEC), Dhaka for her tireless help during the experimental work and preparing the thesis manuscript.

My thanks are also for Mr. Md. Nazrul Islam Khan, Scientific Officer, Materials Science Division (AEC), Dhaka for his help and support when I was writing my thesis. I am grateful to Mr. Md. Manjurul Hoque, Ph.D. student and Associate Professor, Islamic University of Kushtia and Engr. Asit Kumar Gain for their assistance and interaction at the time of preparing this thesis. I would like to give thanks to Ms. Alhamra Parveen, Ms. Anjuman Ara Begum, Ms. Nazmunnahar Begum, Mr. Mohsin, Mr. Mostafizur Rahman, Mr. Ferozur Rahman and Ms. Halima Sadia for their help during my experimental works at the Materials Science laboratory of AEC.

I would like to extend my special thanks to the Vice-Chancellor, Pro-Vice-Chancellor and the Registrar, the University of Asia Pacific (UAP), Dhanmondi R/A, Dhaka for having given me permission and granting me leave to pursue my research at home and abroad. I am very grateful to my respected teacher Prof. Sadruddin Ahmed Chaudhury, Vice-Chancellor, Sylhet International University, Sylhet for his blessings and encouragement to do my research works. My thanks are due to Dr. A.A. Ziauddin Ahamad, Visiting Professor of Physics, BRAC University, Dhaka for his encouragement and interest in my research works. I would like to give thanks to Dr. Abu Hasan Bhuiyan and Dr. Jiban Podder, Professors of Physics, BUET, for their inspiration in doing my research works. My special thanks are for Prof. Minufar Chaudhury, Coordinator, Interdepartmental courses, the University of Asia Pacific, Dhanmondi R/A, Dhaka for her encouragement to finish my research works timely. My thanks are for my colleagues Mr. Sanjit Kumar Paul, Ms. Tahmina Akhter, Ms. Nafisa Sultana, Mr. Takad Ahmed Chawdhury and Dr. Dinak Shohani Kabir for their inspiration when I was doing my research works. I would like to give very special thanks to Dr. Iftekhar Anam, Associate Professor, Department of Civil Engineering, the University of Asia

Pacific for his keen interest and encouragement in my research works. My thanks are for Mr. Shahriar Anam, Head, Department of Business Administration, UAP for his inspiration. I would like to thank to Dr.Fayyaz Khan, Head of the Department of Computer Science & Engineering, UAP for his encouragement in my research work. My thanks are for Dr. Mir Shamsur Rahman, Head, Department of Law and Human Rights, UAP for his moral support and encouragement in my thesis works.

Finally I record my sincerest gratitude to Khulna University of Engineering & Technology, Khulna for providing with the financial assistance during the period of the research work. My thanks are also for Mr. Abdullah Elias Akhter, Mrs. Jolly Sultana Md. Kamrul Hasan Reza, Md. Mahbubur Rahman, Assistant Professors, Enamul Hoque Bhuiyan, Md. Asaduzzaman, Lecturers, Department of Physics, KUET for their moral support. My thanks are also for Saroat Noor, Mr.Zakir Hossain, Pritish Kumar Roy, Sumon Kumar Nath, and Siba pada Mondal Research fellows and other staffs of the Department of Physics, KUET, for their corporation.

My special thanks are for Nandita Boudi and Mrs Mahfuza Hakim, who inspired me a lot during the period of my research works.

I am very much grateful to my parents, father in law and mother in law for their support during the period when I was doing research in Sweden and Vietnam.

There are numerous people who could not be mentioned individually but their interesting discussions have prompted much thought on various aspects, I would also like to thank them.

I would like to mention the name of my wife Shahnaj Parvin whose constant and volatile inspiration has inspired me a lot to undergo this thesis work. I posses an everlasting soft corner for my loving daughter, Faria Mahmud, who has been deprived of my company during the research period.

Md. Sultan Mahmud

To

My Beloved Daughter

Faria Mahmud Nova

CONTENTS

	Page no.
CHAPTER 1	
INTRODUCTION	1
CHAPTER 2	
LITERATURE REVIEW	5
2.1 Introduction to Metallic Glass.	5
2.2 Nanocrystalline Soft Magnetic Alloys	7
2.2.1 Introduction	7
2.2.2 Classification of Soft Nanocrystalline Alloys	8
2.2.3 Technical Requirement for Soft Nanocrystalline Alloys	10
2.3 Review of the Properties of Finemet Type of Soft Nanocrystalline Alloys	13
2.3.1 Nanocrystallization of Finemet Type of Soft Magnetic Alloys	13
2.3.2 Effect of Substitution and Addition of Various Elements on the Properties of Finemet Alloys	17
2.3.3 Low temperature Magnetization of Finemet Alloys	23
2.3.4 Application of Amorphous Magnetic Alloys	24
CHAPTER 3	
THEORETICAL ASPECTS	25
3.1 Nature and Formation of Amorphous Alloys	25
3.2 The Glass Transition Temperature	27
3.3 Stability of the Amorphous Phase	29
3.4 Crystallization of the Amorphous State	30
3.5 Theory of Magnetism	33
3.5.1 Introduction to Magnetic Ordering	33

3.5.2	Ferromagnetism and Magnetic Domain	34
3.5.3	Random Anisotropy Model (RAM) and Strongly Exchanged Coupled Nanocrystalline alloys	39
3.5.4	AC Magnetic Response to the Soft Magnetic Materials	42
3.5.5	Temperature Dependence of Magnetization	44
3.6	Initial Permeability of Nanocrystalline Alloys	47
3.6.1	Theories of Permeability	47
CHAPTER 4		
EXPERIMENTAL		50
4.1	Sample Preparation	
4.1.1	Master alloy preparation	50
4.1.2	Preparation of ribbon by rapid quenching	51
4.1.3	Thermal Treatment of the Amorphous Ribbons	
	53	
4.2	Differential Scanning Calorimetry	53
4.3	X-ray Diffraction	57
4.3.1	Introduction	57
4.3.2	Electromagnetic Radiation	57
4.3.3	Production of X-ray	58
4.3.4	X-ray Diffractometer	59
4.3.5	Determination of Nanometric Grain Size by X-ray Diffraction	63
4.4	Magnetization Measurement Techniques	65
4.4.1	Vibrating Sample Magnetometer (VSM)	65
4.4.2	SQUID magnetometer	68
4.5	Components of Complex Permeability Measurements	72
4.6	Preparation of the samples for complex permeability measurement	75

CHAPTER 5	
RESULTS AND DISCUSSION	76
5.1 Crystallization behavior of $\text{Fe}_{73.5-x}\text{Cr}_x\text{Cu}_1\text{Nb}_3\text{Si}_{13.5}\text{B}_9$ alloys	76
5.1.1 Study of Crystallization Behavior of Amorphous $\text{Fe}_{73.5-x}\text{Cr}_x\text{Cu}_1\text{Nb}_3\text{Si}_{13.5}\text{B}_9$ Alloys	76
5.1.2 Determination of Crystallization Products and Grain Size	83
5.2 Magnetization Measurements	87
5.2.1 Saturation Magnetization	87
5.2.2 Curie Temperature	90
5.2.3 Temperature Dependence of Magnetization	101
5.2.4 Variation of Magnetization $M(0)$ and T_c with Cr Concentration for the $\text{Fe}_{73.5-x}\text{Cr}_x\text{Cu}_1\text{Nb}_3\text{Si}_{13.5}\text{B}_9$ Alloys	106
5.2.5 Field Cooled and Zero Field Cooled Magnetization Behavior of Higher Cr Content Amorphous Alloys	108
5.2.6 Low Temperature Magnetic Behavior of the Amorphous Alloys	111
5.2.7 Variation of Magnetization and Curie temperature with Isothermal Annealing of Higher Cr Content Amorphous Alloys	118
5.3 Permeability Measurements on Amorphous and Annealed Samples of $\text{Fe}_{73.5-x}\text{Cr}_x\text{Cu}_1\text{Nb}_3\text{Si}_{13.5}\text{B}_9$ Alloys	131
CHAPTER 6	
CONCLUSION	138
CHAPTER 7	
BIBLIOGRAPHY	143

LIST OF THE SYMBOLS USED

A	Exchange constant
a	Lattice constant
ASS	Anti scatter slit
ABK	Arrot-Belov-Kouvel
A_{ex}	Exchange stiffness constant
APFIM	Atom probe field ion microscope
B	Flux density
B_0	Magnetic induction in free space
BMGS	Bulk metallic glasses
c	Lattice parameter
CMS	Centre for materials science
D_g	Grain size
d	Average diameter
D	Spin-wave stiffness constant
D_s	Shape dependent demagnetization
DSC	Differential scanning calorimetry
DTA	Differential thermal analysis
E	Activation energy
EXAFS	Extended X-ray absorption fine structure
FWHM	Full width half maximum
FC	Field-cooled
ZFC	Zero-field-cooled
GMI	Giant magneto impedance
H	Magnetic field
H_c	Coercivity
H_0	Magnetic field in free space
HRTEM	High-resolution transmission electron microscope

H_a	Applied magnetic field
H_i	Internal field
H_{ac}	AC driving field
ΔH	Enthalpy of transition
I	X-ray beam intensity
J_{ij}	Exchange coupling constant
J_j	Average saturation magnetization of the material
k	Magnetic hardness parameter
K_{eff}	Effective magnetic anisotropy constant
L	Self inductance of the sample core
L_0	Inductance of the winding coil without sample
L_{ex}	Ferromagnetic exchange length
M_s	Saturation magnetization
M_r	Remanent magnetization
M	Magnetization
$M(0)$	Saturation magnetization at 0 K
MPMS	Magnetic properties measurement system
M_{FC}	Field-cooled magnetization
M_{ZFC}	Zero-field-cooled magnetization
m	Moment
nm	nano meter
NM	Nobel metal
N	Number of planes
n_B	Bohr magnetic moment
μ_B	Magnetic moment in Bohr magneton
μm	Micrometer
PDS	Paramagnetic divergent slit
PRS	Paramagnetic receiving slit
Q	Quality factor
R	Resistance / Gas constant
RF	Radio frequency

RAM	Random anisotropy model
R_H	Hall coefficient
R_c	Critical cooling rate
$\langle r^2 \rangle$	Mean square value of the range of exchange interaction
r_a	Atomic radius
S	Cross sectional area
SRO	Short-range order
SQUID	Super conducting quantum interference device
SEM	Scanning electron microscopy
TE	Rarely transition metal
TEM	Transmission electron microscope
TMA	Thermo magnetic analysis
TTT	Temperature, time & transformation
TL	Ferromagnetic transition metal
T_c	Curie temperature
T_a	Annealing temperature
T_g	Glass transition temperature
T_x	Crystallization temperature
T_{x1}	Primary crystallization temperature
T_{x2}	Secondary crystallization temperature
T_g^0	Ideal glass transition temperature
T_m	Melting point
t_0	Time constant
t	Characteristic time
T_{op}	Optimization of annealing temperature
T_p	Crystallization peak temperature
T_{p1}	Primary crystallization peak temperature
T_{p2}	Secondary crystallization peak temperature
VSM	Vibrating sample magnetometer

V_x	Volume fraction
XRD	X-ray diffraction
X	Reactance
Z	Complex impedance
λ	Wave length
λ_s	Saturation magnetostriction
μ	Permeability
μ_0	Vacuum magnetic permeability
μ_i	Initial permeability
μ'	Real part of the complex permeability
μ''	Imaginary part of the complex permeability
$\tan\delta$	Loss factor or loss tangent
δ_w	Bloch domain wall thickness
χ_{ac}'	ac susceptibility
χ_i	Initial susceptibility
ω	Frequency
ρ	Resistivity
β	Heating rate
θ	Scattering angle
σ	Effective stress
λ	Wave length
γ	Domain wall energy density
γ_k	Anisotropy energy per unit area

Abstract

This thesis focuses on the experimental investigations of the structural, crystallization and magnetic behavior of $\text{Fe}_{73.5-x}\text{Cr}_x\text{Cu}_1\text{Nb}_3\text{Si}_{13.5}\text{B}_9$ ($x = 0, 1, 2, 3, 4, 5, 6, 7, 8, 9, 10, 12.5, 15$ & 17.5) alloys in the amorphous and annealed states. The samples are initially prepared in the amorphous state in the form of thin ribbons by rapid-quenching technique and subsequently annealed. The Characterization of the samples is performed by X-ray diffraction. The crystallization behavior has been studied by Differential Scanning Calorimetry (DSC). Magnetic properties have been measured using Superconducting Quantum Interference Device (SQUID) magnetometer, Vibrating Sample Magnetometer (VSM), Permagraph and LCR meter.

$\text{Fe}_{73.5-x}\text{Cr}_x\text{Cu}_1\text{Nb}_3\text{Si}_{13.5}\text{B}_9$ amorphous alloys upon annealing undergoes phase transformation due to primary crystallization of bcc-Fe(Si) and secondary crystallization of Fe-B phases respectively revealed by DSC and confirmed by X-ray diffraction. The primary crystallization temperature shifts to higher temperature with Cr content implying the enhancement of thermal stability of the amorphous alloys against crystallization due to increasing amount of Cr. The average grain size of the Fe(Si) phase decreases under identical annealing condition as the Cr content is increased. The saturation magnetization and the Curie temperature of the amorphous alloys decrease linearly with the increase of Cr content for the entire composition range due to dilution of Fe magnetic moment and weakening of exchange interaction between magnetic atoms. The critical concentration for the onset of ferromagnetism of the studied system has been found to be 24 ± 1 at.% Cr by linear extrapolation of saturation magnetization and Curie temperature to zero as a function of Cr concentration. A decrease of magnetic moment of $0.055 \mu_B$ and Curie temperature of 26°C per atomic percent of Cr substitution are determined. Higher Cr content amorphous alloys show magnetic hardening at low temperature with the manifestation of divergence between field-cooled and zero field-cooled magnetization, which increases with decreasing temperature as

well as with the increase of Cr content. Temperature dependence of magnetization of the amorphous alloys in the temperature range $0 \leq \frac{T}{T_c} \leq 0.8$, follow the Bloch's spin-wave theory. The spin-wave stiffness constant, D decreases monotonically together with the T_c with the increase of Cr content having a constant value of $\frac{D}{T_c} \approx 0.18$ in whole concentration range. The smaller value of D in the studied system compared with the crystalline ferromagnet indicates that the range of exchange interaction is shorter in these amorphous alloys as expected. Magnetization and Curie temperature of amorphous alloys increase with annealing temperature well below the crystallization temperature due to irreversible structural relaxation. However the depression of T_c is observed for the sample annealed at temperature close to the crystallization temperature. Initial permeability strongly depends on the annealing temperature, which sharply increases with the nanocrystallization of bcc-Fe(Si) phase. An enhancement of initial permeability by two orders of magnitude and a subsequent decrease of relative loss factor $\frac{\tan \delta}{\mu'}$ have been observed for the optimum annealed samples. This occurs because randomly oriented anisotropy is averaged out by exchange interaction between Fe(Si) nanograins mediated by thin intergranular ferromagnetic amorphous layer.

INTRODUCTION

1.1 Introduction

The present state of development of new materials and their understanding on a smaller and smaller length scale is at the root of progress in many areas of materials science. As the size reduces into the nanometer range, the materials exhibit peculiar and interesting physical, chemical, mechanical, magnetic and electrical properties compared to conventional coarse-grained counterparts [1.1]. This is particularly true in the development of new magnetic materials for a variety of important technological application [1.2, 1.3]. Nanomaterials are experiencing a rapid development in recent years due to their existing and/or potential applications in a wide variety of technological areas such as electronics, catalysis, ceramics, magnetic data storage, structural components etc. To meet the technological demands in these areas, the size of the materials should be reduced to the nanometer scale. For example, the miniaturization of functional electronic devices like transistor, diodes, inductors and sensors demand the placement or assembly of nanometer scale components into well-defined structures [1.4]. This new field based on nanomaterials has been named as nanotechnology and emerged as a new branch of science and technology, which is quite diverse and incorporates fields ranging from microelectronics to molecular biology [1.5]. The nanotechnology has its roots date back to a 1959 talk given by Richard Feynman (<http://nano.xerox.com/nanotech/feynman.html>) in which he said, “The principles of Physics, as far as I can see, do not speak against the possibility of maneuvering things atom by atom. It is not an attempt to violate any laws; it is something in principle, that can be done; but in practice it has not been done because we are too big”. But with the tremendous advancement of science and technology for the last two decades the idea that we should be able to economically arrange atoms in most of the ways permitted by physical law has gained fairly general acceptance. The recent advances in materials synthesis, characterization techniques and methods of advance

measurement facilities on the nanometer scale have greatly assisted the expansion of nanotechnology.

Nanomaterials can be classified into nanocrystalline materials and nanoparticles. The former are polycrystalline bulk materials devitrified from the previously synthesized amorphous precursor through appropriate thermal treatment with grain sizes in the nanometer range (less than 100 nm) while the later refers to ultra fine dispersive particles with diameters below 100 nm.

Magnetism is a discipline, which is stimulated by both basic and practical motivations for the study of different nanostructures. Those nanostructured materials are distinguished from conventional polycrystalline materials by the size of the crystallites that compose them. Defined broadly the term nanostructured is used to describe materials characterized by structural features in the range of $\approx 1-100$ nm corresponding typically to $\approx 50-5 \times 10^7$ atoms respectively.

Nanoparticles are interesting from the fundamental point of view due to their extremely small size. The increasing surface to volume ratio with decreasing size results in an increased significance of the grain boundaries (i.e. surface energies) especially in the “real” nanometer range (≤ 10 nm).

Magnetic nanoparticles show a variety of unusual magnetic behaviors when compared to the bulk materials mostly due to the surface / interface effects including symmetry breaking, electronic environment / charge transfer and magnetic interactions. Nanocomposite / nanocrystalline magnetic materials have been developed through appropriate heat treatment of the initial amorphous precursors of the Fe-Si-B and Co-Si-B based alloys for the ultra-soft magnetic properties with extraordinary high permeability and Fe-Nd-B based alloys for the spring exchange hard magnets with high energy product. These technically important materials have enormous applications such as transformers, sensors for the soft and motors, actuators or generators for the hard nanocomposite magnetic materials have already been envisaged [1.6]

There are various methods of preparing nanoparticles and / or nanostructured materials which include: (i) plasma processing [1.7, 1.8] (ii) deposition technique [1.9, 1.10] and (iii) rapid quenching and subsequently crystallized to nanometric grains embedded in a still amorphous matrix [1.11].

In the present thesis work we are dealing with the third variant for the processing of nanocrystalline magnetic materials. In this method an amorphous precursor in the form of ribbons typically 20-30 μm thick (metallic glass) is first obtained from the melt of the parent ingot with appropriate composition using a melt-spinning machine by rapid solidification technique. Since amorphous state is metastable, upon controlled crystallization above the crystallization temperature develops nanocrystalline grains dispersed in a residual amorphous matrix. Magnetic nanocomposites composed of nano-sized magnetic crystals of 10-15 nm embedded in an amorphous matrix have been shown to display excellent soft magnetic properties and found their applications in transformers inductive devices etc. [1.12, 1.13].

Amorphous materials are characterized by a lack of long-range atomic order, similar to that of liquid state. The lack of crystallinity causes amorphous materials to have a very low anisotropy based on random anisotropy model [1.14]. The lower anisotropy of the soft magnetic atoms allows that ferromagnetic exchange length to become larger. This enables a larger volume to be considered for randomizing anisotropy. In magnetic materials the ferromagnetic exchange length expresses the characteristic distance over which a magnetic atom influences its environment and the exchange energy starts to dominate over the anisotropy energy. This characteristic distance is on the order of 100 nm. Thus if the magnetic materials have microstructure with grain diameters smaller than the ferromagnetic exchange length, it becomes possible to “average” the anisotropy of the grains to a very low bulk value by random walk consideration. Such a material then realizes the high saturation magnetization of the crystalline state, low coercivity and high permeability due to randomized anisotropy. In the case of nanocrystalline soft magnetic materials with trade name FINEMET obtained from the careful control of crystallization of their amorphous precursor, it has been determined

that an important averaging of the magnetocrystalline anisotropy over many grains with structural feature 10-15 nm coupled within an exchange length is the root of magnetic softening [1.12, 1.13]. The fact that the ferromagnetic exchange length of this nanometric grain is typically ≈ 35 nm, which illustrates the underlying importance of this length scale in this magnetic system.

The aim of the present work was to study in detail the effect of Cr substitution for an extended range for Fe in the $\text{Fe}_{73.5-x}\text{Cr}_x\text{Cu}_1\text{Nb}_3\text{Si}_{13.5}\text{B}_9$ ($x = 0, 1, 2, 3, 4, 5, 6, 7, 8, 9, 10, 12.5, 15$ & 17.5) alloys on the crystallization behavior, structural and magnetic properties especially on the low temperature range. Although few reports are available on the effect of Cr substitution for Fe in a limited range, low temperature magnetization and higher Cr content Finemet alloys have not been done in much detail. In the present work a detail study of the low temperature magnetization including the evolution of magnetic properties of higher Cr content alloys, which are normally paramagnetic in the as-cast state would be performed.

Literature Review

This chapter explains the development of amorphous alloys and some metallic system termed as metallic glass as well as the properties of metallic glass. It presents in detail a novel type of material known as Finemet prepared from Fe-Si-B based metallic glass with the addition of Cu and Nb exhibiting ultrasoft magnetic properties after partial crystallization. An extensive literature review of the FINEMET type of alloys with wide range of composition, additions and substitutions with various elements and their effects on the overall microstructural and magnetic properties is presented here. In the present thesis the term metallic glass and amorphous alloys will be used interchangeably.

2.1 Introduction to Metallic glass

Amorphous alloys are interesting because they do not have any long-range atomic order. As a result these materials have high resistivities, low magnetocrystalline anisotropy and no microstructural inhomogeneities. The formation of the first metallic glass of $\text{Au}_{75}\text{Si}_{25}$ was reported by Duwez at Caltech, USA, in 1960 [2.1]. They developed the rapid quenching techniques for chilling metallic liquids at very high rates of 10^5 - 10^6 K/s. Their work showed that the process of nucleation and growth of crystalline phase could be kinetically bypassed in some alloy melts to yield a frozen liquid configuration, that is, metallic glass. The significance of Duwez's work was that their method permits large quantities of an alloy to be made into glassy state comparing to other methods, for instance, vapor condensation. Formation, structure and property investigations of metallic glasses have attracted increasing attention because of their fundamental scientific importance and engineering application potential [2.2-2.5]. The techniques of melt quenching have been extensively developed and elaborated for the purpose of producing a wide variety of metallic glasses.

The research on metallic glasses gained more momentum in the early 1970s and 1980s when the continuous casting process for commercial manufacture of metallic glasses ribbons, lines and sheets [2.5] was developed. An expression of academic and industrial research has resulted in that period. However, the high cooling rate limited the amorphous alloys geometry to thin sheets and lines, which are unlikely to find wide applications.

Accordingly, the work of Turnbull and Coworker had made crucial contribution to the discipline. They illustrated the similarities between metallic glasses and other non-metallic glasses such as silicates, ceramic glasses and polymers. It was shown in their work that, a glass transition manifested in conventional glass-forming melts could also be observed in rapid quenched metallic glasses [2.6, 2.7]. The glass transition was found to occur at a rather well defined temperature, which varied only slightly as the heating rate was changed [2.8]. Turnbull predicted that a ratio, referred to as the

reduced glass transition temperature $T_{rg} = \frac{T_g}{T_m}$, of the glass transition temperature T_g to

the melting point, or liquidus temperature T_m of alloy, can be used as a criterion for determining the glass forming ability (GFA) of an alloy [2.9]. According to Turnbull's

criterion [2.10], a liquid with $\frac{T_g}{T_m} = \frac{2}{3}$ becomes very sluggish in crystallization within

laboratory time scale and can only crystallize within a very narrow temperature range. Such liquid can thus be easily undercooled at a low cooling rate into the glassy state. Up to now, the Turnbull criterion for the suppression of crystallization in undercooled melts remains one of the best "rule of thumb" for producing the GFA of any liquid [2.11]. It has played a key role in the development of various metallic glasses including bulk metallic glasses (BMGS) [2.12].

There is no doubt that metallic glasses (amorphous metallic alloys), discovered in the 1970s, are arguably the most important development in magnetic materials in that decade. Besides the significant contribution to the technological progress, which has been made by metallic glasses, they have also widened the knowledge of basic magnetism [2.13].

2.2 Nanocrystalline Soft Magnetic Alloys

2.2.1 Introduction

The present thesis focuses on the detail study of magnetic properties of nanocrystalline alloys of composition $\text{Fe}_{73.5-x}\text{Cr}_x\text{Cu}_1\text{Nb}_3\text{Si}_{13.5}\text{B}_9$ prepared from Fe-Si-B based alloy with addition and substitution of Cu, Nb and Cr respectively. The development of Fe-Si-B soft magnetic metallic glasses made it possible to discover in the late 1980s a new class of magnetic materials termed as nanocrystalline soft magnets having excellent soft magnetic properties. In 1988 Yoshizawa *et al.* [2.14] discovered that excellent soft magnetic properties are obtained when the grain size is reduced to a nanometer scale by crystallizing Fe-Si-B-Cu-Nb amorphous alloys. The alloy composition originally proposed and subsequently has extensively been studied is $\text{Fe}_{73.5}\text{Cu}_1\text{Nb}_3\text{Si}_{13.5}\text{B}_9$ with the trade name FINEMET. The alloy has been developed by Hitachi Metals Company, Japan. The enormous interest in this novel material is driven due to promising technological applications as well as for studying basic magnetic phenomena. The proposed alloy by Yoshizawa is a typical Fe-Si-B metallic glass composition with the addition of Cu and Nb. It has been subsequently demonstrated that the composition Fe-Cu-M-Si-B (M = Cr, V, Mo, Ta, Nb & W) where M elements can be substituted with group V and VI metals for effective improvement of soft magnetic properties [2.15]. These alloys are rapidly quenched from the liquid state into ribbons of 20-30 μm thickness and solidify in the amorphous state. An appropriate heat treatment (annealing) at temperature range of 500°C and 600°C produces a homogeneous ultrafine grain structure of bcc-Fe(Si) with grain sizes of $D_g = 10\text{-}15$ nm embedded in the residual amorphous matrix. The formation of the nanocrystalline microstructure is ascribed to the combined addition of Cu and Nb and their low solubility in bcc-Fe(Si). Copper is thought to enhance the nucleation of bcc grains while Nb act as grain refiner. Nb that segregates to the grain boundaries acts as a diffusion barrier preventing grain growth. Thus Cu and Nb play an important role in nanocrystallization process in these alloys through nucleation and growth mechanism [2.16]. The best soft magnetic properties i.e. low coercivity and high permeability are achieved when grain sizes are between 10-12 nm [2.16-2.18].

2.2.2 Classification of Soft Nanocrystalline Alloys

Choice of soft magnetic materials for applications has been guided by recent developments in the field of soft magnetic materials. Amorphous and nanocrystalline magnetic materials, in terms of combined induction and permeabilities are now competitive with Fe-Si bulk alloys and the Fe-Co alloys. In Fig.2.1 [2.19], figures of merit for Fe-based amorphous alloys, Co-based amorphous alloys and nanocrystalline alloys are summarized. Co-based amorphous alloys, Fe-based amorphous alloys and nanocrystalline alloys have evolved over the past decades with soft magnetic properties which now exceed those of the bulk alloys based on Fe, Co and Fe-Co.

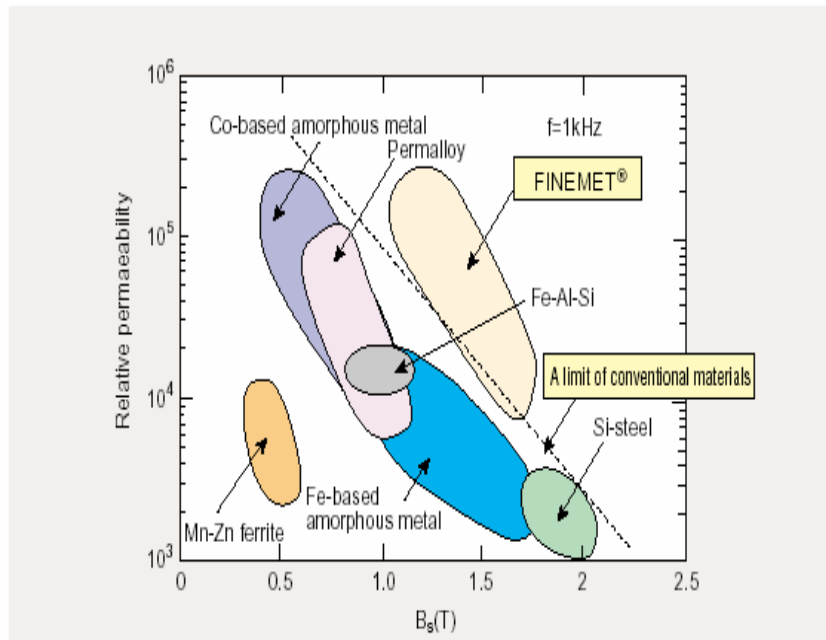


Fig. 2.1 Phase diagram of various types of materials

Nanocrystalline alloys can be described in general as $TL_{1-x}(TE - M - NM)_x$, where TL denotes a late (ferromagnetic) transition metal element, TE is an early transition metal element, M is a metalloid, and NM is a noble metal. This composition usually has $x < 0.20$ i.e. with as much late ferromagnetic transition metals (TL of Co, Ni, or Fe) as possible. The remaining early transition metals (TE = Zr, Nb, Hf, Ta, etc.) and

metalloids (M = B, P, Si etc.) are added to promote glass formation in the precursor. The noble metal elements (NM = Cu, Ag, Au, etc.) serve as nucleating agents for the ferromagnetic nanocrystalline phase. The compositions are limited by where glass formation can occur prior to the nanocrystallization route. These alloys may be single phase (Type I) but are generally two-phase materials with a nanocrystalline ferromagnetic phase and a residual amorphous phase at the grain boundaries (Type II). The Type II nanocrystalline alloys might have general properties (i) relatively high resistivity (50-80 $\mu\Omega$ cm) (ii) low magnetocrystalline anisotropy (iii) increased mechanical strength. With properties such as these, nanocrystalline alloys have great potential as soft magnetic materials.

Nanocrystalline Fe-Si-B-Nb-Cu alloys have been patented under trade name Finemet and have been mentioned above and will continue in the rest of the thesis.

In 1990 Suzuki *et al.* [2.20] reported the development of the Fe₈₈Zr₇B₄Cu₁ alloy, which was named NANOPERMTM. Zr and B act as glass forming agents in this alloy and the microstructure consists of α -Fe grains embedded in an amorphous matrix. By eliminating Si, higher saturation induction is achieved than FINEMET, but the H_c are also higher. The amorphous intergranular phase in both FINEMET and NANOPERM has Curie temperatures lower than that of the nanocrystalline grains.

In 1998 Willard *et al.* [2.21] reported the development of HITPERM, an alloy based on the composition Fe₄₄Co₄₄Zr₇B₄Cu₁. The key distinction is the substitution of Co for Fe. HITPERM forms α -FeCo grains in a Co enriched amorphous matrix has a Curie temperature higher than the primary crystallization temperature of the alloy. This allows the α -FeCo grains to remain exchange coupled at high operating temperatures. Due to the presence of Co, HITPERM alloy has an M_s higher than FINEMET or NANOPERM as well as a higher H_c.

2.2.3 Technical Requirement for Soft Nanocrystalline Alloys

Magnetic hysteresis is a useful attribute of permanent magnet material in which we wish to store a large metastable magnetization. On the other hand, a large class of applications requires small hysteresis losses per cycle.

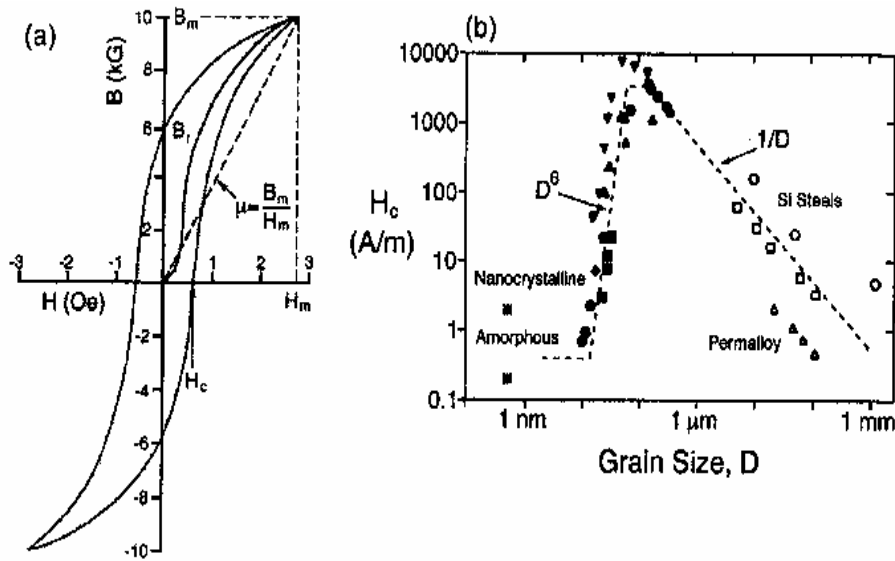


Fig.2.2(a) Hysteresis curve for a soft Fig.2.2 (b) Grain size (D) vs. coercivity (H_c) curve
Magnetic materials

These include applications as inductors, low and high frequency transformers, alternating current machines, motors, generators and magnetic amplifiers. The desired technical properties of interest for soft magnetic materials include [Fig. 2.1(a)].

(i) **High permeability: Permeability:** $\mu = \frac{B}{H} = (1 + \chi)$, is the material's parameter which describes the flux density (B), produced by a given applied field (H).

In high permeability materials, we can produce very large changes in magnetic flux density in very small fields.

(ii) **Low hysteresis loss:** Hysteresis loss is the energy consumed in cycling a material between a field H and $-H$ and then back again. The energy consumed in one cycle is $W_h = \oint MdB$ or the area inside the hysteresis loop. The power loss of AC device includes a term equal to the frequency multiplied by the hysteretic loss per cycle. Also of concern at high frequencies are eddy current losses that are intimately related to the material's resistivity (ρ).

(iii) **Large saturation and remanant magnetizations:** A large saturation magnetization (M_s), induction (B_s) and small remanant magnetization (M_r) are desirable in applications of soft magnetic materials.

(iv) **High Curie temperature:** The ability to use soft magnetic materials at elevated temperatures is intimately dependent on the Curie temperature or magnetic ordering temperature of the material.

Conventional physical metallurgy approaches to improving soft ferromagnetic properties involve tailoring the chemistry and optimizing the microstructure. Significant in the optimizing of the microstructure is recognition of the fact that a measure of the magnetic hardness (coercivity, H_c) is roughly inversely proportional to the grain size (D_g) for grain sizes exceeding $\sim 0.1-1 \mu\text{m}$ (where the grain size exceeds the Bloch domain wall thickness (δ_w)). In such cases grain boundaries act as impediments to domain wall motion, and thus fine-grained materials are usually magnetically harder than large grain materials. Significant recent developments in the understanding of magnetic coercivity mechanisms have lead to the realization that for very small grain sizes $D < \sim 100 \text{ nm}$ [2.17, 2.18, 2.22-2.25], H_c decreases rapidly with decreasing grain size shown in Fig. 2.2 (b). This can be understood by the fact that the domain wall, whose thickness δ_w , exceeds the grain size, now samples several (or many) grains so that fluctuations in magnetic anisotropy on the grain size length scale are irrelevant to domain wall pinning. This important concept suggests that nanocrystalline and amorphous alloys have significant potential as soft magnetic materials. Soft magnetic properties require that nanocrystalline grains be exchange coupled and therefore any of

the processing routes yielding free standing nanoparticles must include a compaction method [2.28-2.30] in which the magnetic nanoparticles end up exchange coupled. Similar ideas have been stated for so called spring exchange hard magnetic materials [2.26-2.28].

The issues, which are pertinent to the general understanding of the magnetic properties of amorphous and nanocrystalline materials, are explored here along with the recent developments. The development of soft magnetic materials for applications requires attention to a variety of intrinsic magnetic properties (some of them ancillary) as well as development of extrinsic magnetic properties through an appropriate optimization of the microstructure. As intrinsic properties we take to mean microstructure insensitive properties. Among the fundamental intrinsic properties (which depend on alloy chemistry and crystal structure) the saturation magnetization, Curie temperature, magnetocrystalline anisotropy and the magnetostrictive coefficients are all important. In a broader sense, magnetic anisotropy and magnetostriction can be considered as extrinsic in that for a two-phase material (in aggregate) they depend on the microstructure. The desire for large magnetic inductions typically limits choices to alloys of Fe and Co (the elemental transition metal magnets with the largest atomic dipole moments). Curie temperatures are also largest for elemental Fe (770°C) and Co (1100°C), suggesting the use of Fe or Co (or Fe-Co) alloys especially in high temperature applications. Magnetocrystalline anisotropy and magnetostriction, which are determining factors in the ease in which the magnetization vector can be rotated into the direction of the applied field, are also sensitivity dependent on alloy chemistry. Many important soft magnetic alloy systems have zero crossings of the magnetocrystalline anisotropy, or magnetostriction coefficients, which can be exploited in the development of soft magnetic materials. The development of advanced and newer magnetic materials with enhanced properties is closely related to the fundamental understanding and exploitation of influence of microstructures on the extrinsic magnetic properties.

Important microstructural features include grain size, shape and orientation, defect concentrations, compositional inhomogeneities, magnetic domains and domain walls. The interaction of magnetic domain walls with microstructural impediments to their motion is of particular importance to the understanding of soft magnetic properties. Extrinsic magnetic properties, which are important in soft magnetic materials, include the magnetic permeability and the coercivity, which typically have an inverse relationship. Remanant magnetization, squariness of the hysteresis loop and magnetic anisotropy (crystalline, shape or stress related) are also important in determining magnetic softness.

2.3 Review of the Properties of Finemet Type of Soft Nanocrystalline Alloys

2.3.1 Nanocrystallization of Finemet Type of Soft Magnetic Alloys

The crystallization of amorphous solids into nano-meter sized polycrystalline phases generally less than 100 nm is referred as nanocrystallization. Synthesis of nanocrystalline materials can be done by variety of techniques such as rapid solidification from the liquid state and subsequent controlled crystallization, mechanical alloying, plasma processing and vapor deposition [2.29]. But the microstructure necessary for the soft magnetic properties cannot be obtained by the later two processes mentioned above [2.30-2.31]. It has been established that controlled crystallization of the amorphous alloys in the form of thin ribbons prepared by rapid solidification technique using melt-spinning machine appeared to be the most suitable method available until now to synthesize nanocrystalline alloys with attractive soft magnetic properties. The basic principle for the crystallization method from amorphous solids is to control the crystallization kinetics by optimizing the heat treatment conditions such as annealing temperature and time, heating rate, etc. so that the amorphous phase crystallizes completely into a polycrystalline material with ultra-fine crystallites. Nanocrystallization can be realized upon either isothermal or anisothermal annealing in various amorphous metallic alloys in the form of ribbons. Controlled crystallization of FINEMET type of Fe-Cu-Nb-Si-B alloys can be used to obtain partially crystallized materials with nano-meter size crystallites embedded in residual amorphous matrix. This special nano-crystal / amorphous composite structure with appropriate

compositions allow the material to exhibit extraordinary soft magnetic properties [2.14-2.18]. FINEMET alloys crystallized at temperatures above their primary crystallization temperature but below the secondary crystallization temperature can yield nanocrystalline grains with average grain size 10-50 nm as a result of primary crystallization of α -Fe(Si) phase embedded in a still remaining amorphous matrix. The excellent soft magnetic properties only occur when the grain size of the primary crystallization product of α -Fe(Si) is limited to 10-15 nm. Also the secondary crystallization phase like Fe-B should be completely avoided. This is to note that to obtain an appropriate nanoscale microstructure necessitates very high nucleation rate and very slow growth of the crystalline precipitates simultaneously. It has long been established that when the conventional metallic glasses based on Fe-Si-B are crystallized for the optimization of soft magnetic properties, it has been found that relatively coarse grain microstructure having various crystalline phases have been evolved that dramatically deteriorated the soft magnetic properties. Therefore, in the FINEMET composition Fe-Cu-Nb-Si-B, the important role of Cu and Nb in the formation of nanometric grain size of 10-15 nm is well understood. It has been established that Cu acts as nucleating agent for the nanograins formation while Nb acts as retarding agent for the growth of nanograins. Nb also inhibits the formation of detrimental intermetallic phase like Fe-B. This iron-boride phase is the product of secondary crystallization generally takes place at relatively higher temperature that deteriorates soft magnetic properties drastically.

The nanocrystalline state is achieved by annealing Finemet alloys at temperatures typically between about 500⁰C and 580⁰C, which leads to primary crystallization of bcc Fe. The resulting microstructure is characterized by randomly oriented, ultrafine grains of bcc Fe-Si (20 at.%) with typical grain sizes of 10-15 nm embedded in a residual amorphous matrix which occupies about 20-30% of the volume and separates the crystallites at a distance of about 1-2 nm. These features are the basis for the excellent soft magnetic properties indicated by the high values of the initial permeability of about 10⁵ and corresponding low coercivities of less than 1 A/m.

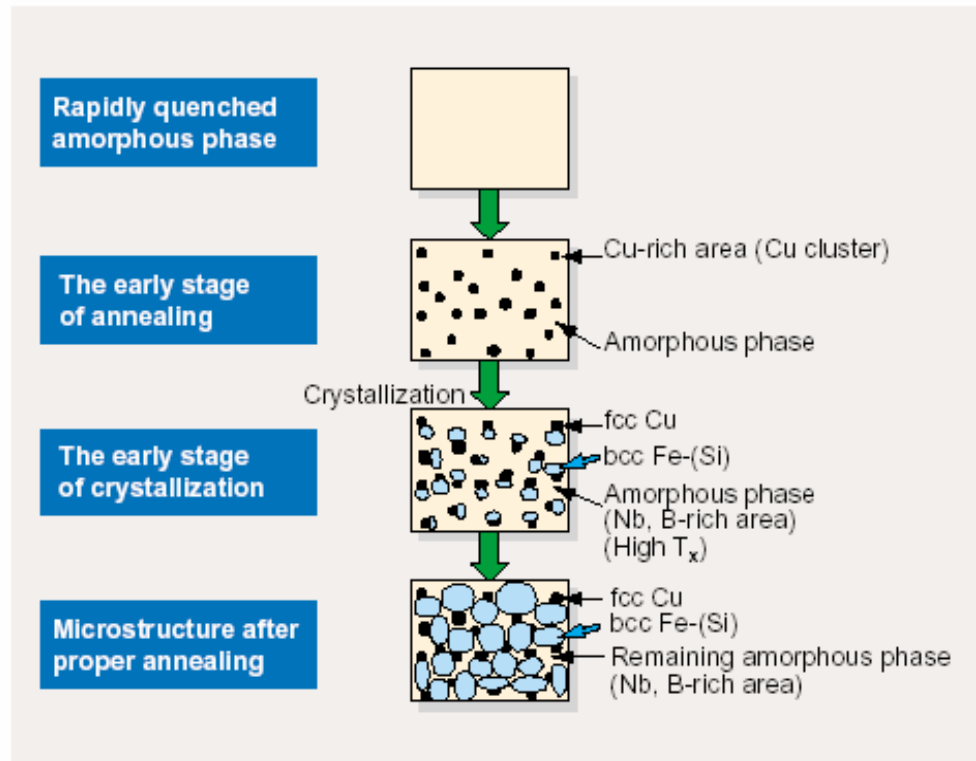


Fig.2.3 Microstructure of different phases of nanocrystalline alloys

A characteristic feature is that the nanocrystalline microstructure and accompanying soft magnetic properties are rather insensitive to the precise annealing conditions within a wide range of annealing temperatures, T_a , about $\Delta T_a \approx 50\text{-}100^\circ\text{C}$. They develop in a relatively short period of time (about 10-15 min) and does not much alter even after prolonged heat treatment of several hours [2.32]. A typical heat treatment like 1h at 540°C in most cases yields a nanocrystalline microstructure close to the quasi-equilibrium state

Only annealing at more elevated temperatures above about 600°C leads to the precipitation of small fractions of boride compounds like Fe_2B or Fe_3B with typical dimensions of 50 nm to 100 nm, while the ultrafine grain structure of b.c.c Fe-Si still persists. Further increases of the annealing temperature above about 700°C , finally

yields grain coarsening. Both the formation of Fe borides and grain coarsening deteriorates the soft magnetic properties significantly. The evolution of microstructure during annealing is depicted schematically in Fig.2.3 and summarized as follows according to Hono *et.al* [2.33, 2.34].

In the as-quenched state the alloy $\text{Fe}_{73.5}\text{Cu}_1\text{Nb}_3\text{Si}_{13.5}\text{B}_9$ has been found both structurally and chemically homogeneous amorphous solid solution as confirmed by the combined use of atom probe field ion microscope (APFIM) and high-resolution transmission electron microscope (HRTEM). At the initial stage of the annealing, Cu rich clusters are formed by either a spinodal process or nucleation in the amorphous state. Each cluster formation causes a concentration fluctuation of iron also, since Cu substitutes for iron. Because of this concentration fluctuation, the density for the nuclei of the bcc crystalline phase is increased significantly although the evidence of concentration fluctuation in the fully amorphous state has not been observed because the investigators [2.34] observed the Cu clusters and bcc phase simultaneously at the early stage of the nanocrystallization. Annealing slightly at higher temperature at the initial stage of crystallization $\alpha\text{-Fe}(\text{Si})$ phase forms. At this stage Nb and B are excluded from $\alpha\text{-Fe}(\text{Si})$ and are enriched in the remaining amorphous phase, because they are insoluble in the $\alpha\text{-Fe}(\text{Si})$ phase. This happens when the annealing treatment is carried out at around 550°C when Cu clusters are formed with a few nanometer diameters. Thus the regions in between the Cu rich clusters provide a significantly increased density of nucleation sites for the crystallization of bcc Fe. The consequence is an extremely fine nucleation of bcc Fe-Si crystallites at a high rate, which subsequently grow in a diffusion-controlled process as the annealing proceeds further [2.35]. As annealing goes on the grain size of the $\alpha\text{-Fe}(\text{Si})$ increases. At the same time the Si content of this phase keeps increasing since Si tends to be partitioned to the bcc $\alpha\text{-Fe}(\text{Si})$ phase. Since the Nb and B enrichment in the amorphous phase stabilizes the remaining the amorphous phase, the grain growth of the bcc phase eventually stops. The presence of Nb at the same time inhibits the formation of Fe-B compounds. The Cu concentration of the clusters also increases as the crystallization proceeds. They will go to around 5 nm and the concentration of Cu increases to 60 at.%. This phase should eventually loose

ferromagnetism at room temperature and becomes the paramagnetic phase. However, since the size is too small compared to the domain wall width, the precipitation of such a paramagnetic phase does not adversely affect the soft magnetic properties.

At the optimum stage, three distinct phases are present based on the chemical compositions. One phase is the Fe-Si bcc solid solution containing approximately 20 at.% Si with virtually no Nb and Cu partitioning with average grain size 10-15 nm. A few percent of B is, however contained in this phase. The second phase is the residual amorphous phase containing approximately 10-15 at.% of Nb and B. In this amorphous phase, approximately 5 at.% of Si is partitioned but virtually no Cu is contained. The third phase is significantly enriched in Cu (~ 60 at.%) with less than 5 at.% of each Si, B and Nb. As a result, the content of Fe in this phase is only 30 at.%. The size of this Cu rich particle is approximately 5 nm.

2.3.2 Effect of Substitution and Addition of Various Elements on the Properties of Finemet Alloys

It has been well established by the time through extensive research work that the addition of Cu and Nb simultaneously with Fe-Si-B based amorphous alloys is the necessary condition for the extraordinary soft magnetic properties of the Finemet alloy. This addition extends the temperature range between the primary crystallization α -Fe(Si) temperature, T_{x1} and secondary crystallization Fe-B temperature T_{x2} premiere for achieving superior magnetic properties [2.36]. It should be stressed again that good soft magnetic properties require not only a small grain size but at the same time the absence of boron compounds. The separation between the primary crystallization of bcc Fe and the precipitation of Fe-B compounds not only is determined by the Cu and Nb additions but, decrease with increasing boron content. This puts a further constraint on the alloy composition namely that the boron content should be kept at a low or moderate level in order to obtain an optimum nanoscaled structure.

In summary, the behavior of the onset of crystallization temperature and composition shows that a basic condition for the formation of typical nanocrystalline structure is given by a primary crystallization process before stable or meta-stable intermetallic phases are formed. Obviously, this can be attained by (i) alloying additions which lead clearly separated stages of crystallization at T_{x1} and T_{x2} and (ii) by annealing at $T_{x1} < T_a < T_{x2}$ such that only the phase forming at and above T_{x1} is crystallizing. Murillo *et al.* [2.37] studied the influence of Cu/Nb content and annealing conditions on the microstructure and the magnetic properties of FINEMET alloys. Grain size, phase composition and transition temperatures were observed to depend on the ratio of Cu/Nb content. The magnetic properties are strongly correlated to the microstructural features. Numerous research works have been carried out to improve the properties of $Fe_{73.5}Cu_1Nb_3Si_{13.5}B_9$ FINEMET alloy by investigating the effects of substitution and addition of various elements.

Kwapulinski *et al.*[2.38] have studied the effect of Cr, Mo, Zr substituted for Nb of $Fe-Cu-X-Si_{13}B_9$ ($X = Cr, Mo \& Zr$) amorphous alloys on the optimization of annealing temperature (T_{op}) corresponding to the maximum permeability and found that it varies linearly with the atomic radius (r_a) of the substituted elements in the order of $T_{op} = Zr > Mo > Cr$. This result to a certain extent reflects the dependence of the crystallization temperature (T_x) on the atomic radius [2.39]. Niobium can be substituted by other group V or VI refractory elements, like Cr, V, Mo, W or Ta which act similarly on the crystallization process and on the magnetic properties [2.15]. Like for Nb, the atomic volumes of these refractory elements are larger than that of Fe, which reduces the diffusion coefficients and, thus stabilizes the amorphous matrix and slows down the kinetics of grain coarsening [2.40]. Accordingly the efficiency of these elements for grain size refinement increases in the order of their atomic volumes, i.e., $Cr < V < Mo \approx W < Nb \approx Ta$. Thus, finest grain structures and superior magnetic properties in practice require at least a certain amount of the elements Nb or Ta.

Zhi *et al.* [2.41] studied the influence of the silicon and boron contents on the structure and magnetic properties of $Fe_{73.5}Cu_1Nb_3Si_xB_{22.5-x}$ (at. %) nanocrystalline alloys, with $x = 9.5-17.5$. The results show that the lattice constants and Curie temperatures of the

nanocrystalline alloys decreases linearly with increasing x . The saturation magnetostriction (λ_s), values of the alloys decrease with increasing Si content for the nanocrystalline state, but increase for the as-quenched state. For the alloys annealed at a certain temperature, the volume fraction (V_x) of nanoscale grains is related to the Si and B contents of the alloys. V_x increases with increasing x as well as decreasing B content. Within the range of compositions studied, the nanocrystalline alloy has the optimum soft magnetic properties when $x = 14$.

The saturation magnetization in the $\text{Fe}_{74.5}\text{Cu}_1\text{Nb}_3\text{Si}_x\text{B}_{22.5-x}$ (at.%) system indeed increases up to about 1.6T if boron is substituted for silicon. However, this benefit is accompanied by a severe degradation of the soft magnetic properties due to high boron content, which favors the formation of boron compounds that deteriorate the soft magnetic properties. Therefore boron content is kept at a moderate level below 10 at.%. However, a corresponding reduction of the boron content at low Si contents, for the sake of glass forming ability, is only possible if other good glass forming elements are added simultaneously. Such elements, which extend the glass forming range at low Si and B elements, are group IVa to VIa transition metals [2.42]. The glass forming range is the widest for Hf containing alloys and decreases in the order of $\text{Zr} > \text{Nb} \approx \text{Ta} > \text{Mo} \approx \text{W} > \text{V} > \text{Cr}$. The most stable amorphous phase is, thus, obtained in alloys containing refractory metals with large atoms and low d-electron concentrations, i.e., particularly Zr, Hf, Nb & Ta. The effect of substitution of Co for Fe in FINEMET $\text{Fe}_{73.5-x}\text{Co}_x\text{Nb}_3\text{Si}_{13.5}\text{Cu}_1\text{B}_9$ alloys has been studied in detail on the magnetic properties [2.43-2.49]. Chau *et al.* [2.43] found that Curie temperature (T_c) of the amorphous and the crystalline phases increase gradually with the increase of Co concentration while the primary crystallization temperature decreases with Co. Crystallization activation energy of α -Fe (Si) increases as the Co content is increased. It has been shown by the authors that the grain size, D_g and the Curie temperature of the Fe-Si phase increase with the increase of Co content. Ohnuma *et al.* [2.44] studied the effect of Co replacement up to high concentration for Fe on the magnetic properties of $\text{Fe}_{73.5-x}\text{Co}_x\text{Nb}_3\text{Si}_{13.5}\text{Cu}_1\text{B}_9$ nanocrystalline alloys and found that the permeability decreases and the coercivity increases with Co content x , because of increase of the grain size. It was also found that

high Co content enables the alloys for their applications to much higher frequency range than conventional FINEMET alloy. Zbroszyk *et al.* [2.45-2.47] have examined the influence of small Co additions to FINEMET alloy on microstructural and magnetic properties. They compared $\text{Fe}_{73.5}\text{Cu}_1\text{Nb}_3\text{Si}_{13.5}\text{B}_9$ and $\text{Fe}_{66.5}\text{Co}_7\text{Cu}_1\text{Nb}_3\text{Si}_{13.5}\text{B}_9$ alloys. It was concluded that Co accelerated the crystallization process, though the nanocrystalline phase remains as the bcc $\alpha\text{-Fe}(\text{Si})$. Generally improved magnetic properties were noted with Co additions. Effect of galvanomagnetic and magnetoelastic behavior of amorphous and nanocrystalline $\text{Fe}_{73.5-x}\text{Co}_x\text{Cu}_1\text{Nb}_3\text{Si}_{13.5}\text{B}_9$ ($x = 0-3$) alloys have been studied by Maria *et al.* [2.48]. An improvement of Hall coefficient (R_H) and a substantial decrease of saturation magnetostriction (λ_s) is observed with Co addition in the amorphous as well as in the nanocrystalline state.

Partial substitution of Al for Fe in $\text{Fe}_{73.5-x}\text{Al}_x\text{Cu}_1\text{Nb}_3\text{Si}_{13.5}\text{B}_9$ has been studied with wide range of Al concentration to see the effect on the structural, magnetic and other properties [2.50-2.54]. Todd *et al.* [2.50] studied the effect of Al from 0-6 at.% and observed that 2 at.% Al substitution showed the best magnetic properties corresponding to highest permeability, lowest coercivity and magnetostriction as compared with the conventional FINEMET. Higher substitution of Al for Fe leads to a deterioration of permeability as a result of saturation magnetization. Phan *et al.* [2.51] found that small addition of Al in the $\text{Fe}_{73-x}\text{Al}_x\text{Si}_{14}\text{B}_{8.5}\text{Cu}_1\text{Nb}_{3.5}$ ($x = 0, 2$) alloys leads to an improved magnetic softness and hence the giant magnetoimpedance (GMI) effect as well as its field sensitivity when compared to the Al-free nanocomposite. This finding is beneficial for developing high performance GMI sensors. However, very small amount of Al substitution for Fe up to 1 at.% is found to increase the permeability and decreases the coercivity with the manifestation of better magnetic properties corresponding to 0.1 at.% of Al along with a slight sacrifice of magnetic induction [2.52]. It has also been demonstrated by the authors that the crystallization temperature related to the formation of the $\alpha\text{-Fe}(\text{Si})$ solid solution phase is decreased while that related to the formation of the Fe-boride is increased with Al addition. Zorkovska *et al.* [2.53] studied the Al substitution up to 7 at.% in the FINEMET alloy $\text{Fe}_{73.5-x}\text{Al}_x\text{Nb}_3\text{Cu}_1\text{Si}_{13.5}\text{B}_9$ ($x = 0, 1, 2, 3, 5 \& 7$). In as-quenched state Al decreased linearly the magnetization, but up to 3 at.

% enhanced the Curie temperature of the alloy. The Curie temperature of the crystalline phase and the magnetization in annealed samples abruptly decreased, when there was more than 5 at.% of Al in the alloy due to the ordered DO₃ like structure (Fe₃Si) leading to paramagnetic behavior.

Tate *et al.* [2.54] have examined the influence of Al additions on nanostructure and soft magnetic properties of FINEMET alloys. They studied Fe_{73.5-x}Al_xSi_{13.5}B₉Cu₁Nb₃ alloys with $0 \leq x \leq 10$. A reduction in the (bulk-line) magnetocrystalline anisotropy for α -Fe(Si) was used to explain a reduced coercivity in alloys with $2 \leq x \leq 8$. A nearly linear reduction in the induction was observed from 1.5 T ($x = 0$) to 0.9 T ($x = 10$) with Al addition.

Vojtanik *et al.* [2.55, 2.56] have investigated the influence of Ni substitution for Fe on the intrinsic magnetic properties in FINEMET alloys. Fe_{73.5-x}Ni_xSi_{13.5}B₉Cu₁Nb₃ ($x = 0, 5, 10, 15, 20$ & 25 at.%) amorphous and nanocrystalline alloys were studied by X-ray diffraction, Mössbauer spectroscopy and thermodynamic analysis. Small additions of Ni were shown to increase the Curie temperature and the room temperature saturation magnetization of amorphous samples. Ni caused a suppression of the secondary crystallization temperature (T_{x2}). A nanocrystalline structure was observed after crystallizing the $x = 0, 5, 10$ & 15 alloys but not for the $x = 20$ & 25 at.% alloys. The 5 at.% Ni addition increase the room temperature B_s from 1.19 to 1.39T and T_c of the amorphous phase from 332⁰C to 337⁰C. Both quantities decrease for higher Ni concentrations. Magnetic and structural properties of FINEMET alloy and with the substitution of Nb by Ta, Mo, Cr, W have been studied by several investigators [2.57-2.59]. Results show that FINEMET composition with Nb and Ta show similar soft magnetic characteristics while alloy with substitution of Nb and Cr, Mo and W display somewhat lower soft magnetic properties. Hakim *et al.* [2.57] found with the T_a substituted alloy superparamagnetic and superferromagnetic behavior depending upon the volume fraction of the nanocrystallites from the temperature dependence of permeability of the samples annealed in the temperature range 500-575⁰C. Similar behavior of superparamagnetic/superparamagnetic has been observed in the FINEMET

alloy with higher content of Cr substituted for Fe [2.60, 2.61]. Magnetic properties of partial substitution of Fe by Cr have been studied by several investigators with a limited concentration of Cr between 1 & 5 at.% substituted for Fe in the FINEMET alloy [2.62-2.64]. The authors found that Cr enhances the crystallization temperature, controls the volume fraction and particle size of α -Fe(Si) phase and reduces the Curie temperature. The giant magnetocaloric effect has been observed in the studied samples [2.63]. The influence of Cr content with higher percentage of Cr on the magnetization behavior of $\text{Fe}_{73.5-x}\text{Cr}_x\text{Cu}_1\text{Nb}_3\text{Si}_{13.5}\text{B}_9$ alloys have been studied [2.65]. It has been found that magnetic moment and the Curie temperature decreases linearly with Cr concentration. The onset of ferromagnetism for the alloy system studied has been claimed to be Cr < 27 at.% and the alloys have been found to follow the Bloch's $T^{3/2}$ law in their temperature dependence of magnetization. Investigations have been carried out on the effect of substitution of Au and Ag for Cu in the Finemet on the crystallization behavior and magnetic properties [2.66-2.69]. It has been found that Au behaves similarly as Cu on the crystallization behavior and magnetic properties while Ag shows slightly inferior properties.

Magnetic properties and magnetoimpedance effects have been studied of Mn substitution for Fe in the Finemet alloy $\text{Fe}_{73.5-x}\text{Mn}_x\text{Cu}_1\text{Nb}_3\text{Si}_{13.5}\text{B}_9$ in the amorphous and nanocrystalline state [2.70, 2.71]. Gomez-Polo *et al.* [2.70] showed that the partial substitution of Fe by Mn in FINEMET alloys plays an important role in the evolution of magnetic properties of the alloy. This has been manifested through the enhancement of magnetic hardening of the nanocrystalline state attributed to the migration of the Mn atoms to the grain boundary region, which reduces the exchange coupling between the crystalline and residual amorphous phases. Tho *et al.* [2.71] found a decrease of Curie temperature (T_c) and saturation magnetization (M_s) due to the substitution of Fe by Mn in the FINEMET composition $\text{Fe}_{73.5-x}\text{Mn}_x\text{Cu}_1\text{Nb}_3\text{Si}_{13.5}\text{B}_9$ ($x = 1, 3 \text{ \& } 5$). The authors found that the presence of Mn affects the shape of the magnetic hysteresis loops causing a decrease in coercivity and maximum magnetization in the amorphous and annealed samples. The frequency dependence of magnetoimpedance (MI) as a function of frequency has been measured. The correlation between MI effect and soft magnetic

properties has been sought in which the giant magnetoimpedance effect corresponding to the ultrasoft magnetic properties has been well established.

2.4 Low temperature Magnetization of Finemet Alloys

Low temperature magnetization behavior as a function of field and temperature is important to understand the magnetization mechanism at the ground state. Although much not detailed, some low temperature measurement on amorphous and nanocrystalline alloys has been reported. Holtzer *et al.* [2.72] have measured low temperature behavior of magnetic properties such as coercivity, magnetization and magnetostriction of original FINEMET $\text{Fe}_{73.5}\text{Cu}_1\text{Nb}_3\text{Si}_{13.5}\text{B}_9$ samples at different stages of crystallization and have been compared to the amorphous counterpart. The authors found that the temperature dependence of magnetization in the low temperature range for the amorphous and annealed samples follows the well-known Bloch's $T^{3/2}$ law. The saturation magnetization (M_s) at 5 K decreases continuously with the increase of annealing temperature, which contradicts the results of Lovas *et al.* [2.73]. The M_s value measured at 12 K by ref. [2.73] has been found to increase until the initial stage of crystallization ($525^\circ\text{C}/4\text{min}$) attaining maximum value of M_s and thereafter decreases gradually as the annealing time and/or temperature increases. However the room temperature M_s values show the similar trend in agreement with the M_s value of Holzer *et al.* [2.72] and have been interpreted as due to structural relaxation. It has also been depicted that the Curie temperature (T_c^{am}) of the amorphous phase increases continuously with annealing temperature up to the beginning of nanocrystallization due to irreversible structural relaxation.

According to Holtzer [2.72] the spin-wave stiffness constant (D) and the exchange constant (A) increase with increasing of annealing temperature. The temperature dependence of magnetostriction (λ_s) in the low temperature range has been approximately described by $T^{3/2}$ behavior in the light of temperature dependence of magnetization by Bloch's law. Ponpandian *et al.* [2.74] also studied the low temperature magnetization of original FINEMET composition and found that the $M(T)$ in the low

temperature region follows the spin-wave theory. The authors also concluded that the range of exchange interaction $\langle r^2 \rangle$ is shorter in the amorphous state in comparison with that of the crystalline state. A low temperature magnetization study of amorphous $\text{Fe}_{73}\text{Cu}_1\text{Mo}_3\text{Si}_{13.5-x}\text{Al}_x\text{B}_9$ alloys by Prabhu *et al.* [2.75] revealed a linear fit with $T^{3/2}$ law. The calculated value of the exchange stiffness constant (D) decreased from $116 \text{ meV}\text{\AA}^2$ for 0 at% Al to $107 \text{ meV}\text{\AA}^2$ for 5% Al, which is typical for amorphous solids and is in good agreement with the reported literature values [2.76, 2.77].

2.5 Application of Amorphous Magnetic Alloys

Some of the attractive technical characteristics of amorphous alloys and their nanocrystalline composites are as follows:

- ▶ Amorphous magnetic alloys exhibit high electrical resistivities due to electron scattering from the atomic disorder. High resistivity results in reduced eddy currents.
- ▶ These alloys theoretically possess zero macroscopic magnetocrystalline anisotropy, which implies reduced anisotropy field.
- ▶ They have no microstructural discontinuities such as dislocations, grain boundaries or precipitates. This significantly reduces the possible pinning sites for domain walls, reducing the coercivity.
- ▶ The highly elastic behavior of these alloys makes them less prone to degradation during handling.
- ▶ The absence of microstructural discontinuities resulted in improved corrosion resistance. The general presence of elements such as B, Si and C also improves the corrosion resistance.

Theoretical aspects

3.1 Natures and Formation of Amorphous Alloys

The term “amorphous” defines a non-crystalline body while a “glass” refers to a molten mass that is cooled rapidly to prevent crystallization. By analogy, the term “metallic glass” usually refers to a metallic alloy rapidly quenched in order to “freeze” its structure from the liquid state.

The expression “glass” in its original sense refers to an amorphous or nanocrystalline solid formed by continuous cooling of a liquid while a solid is defined somewhat arbitrary as object having a viscosity greater than 10^{14} Pa.s [3.1]. A glass lacks three-dimensional atomic periodicity beyond a few atomic distances. It is characterized by limited number of diffuse halos in X-ray, electron and neutron diffraction and no sharp diffraction contrast in high-resolution electron microscopy. Glasses have been found in every category of materials and of various bond types: covalent, ionic, Van der Waals, hydrogen and metallic. The glass-forming tendency varies widely. Some oxide mixtures form a glass at normal slow cooling rates of ~ 1 K/min while monoatomic metals with possible incorporation of impurities require rates as high as $\sim 10^{10}$ K/s [3.2].

During the solidification no essential change in spatial atomic configuration occurs. A glass may be considered as a solid with frozen-in liquid structure. It is in general not in an internal equilibrium state and thus relaxes structurally to a more stable equilibrium state whenever atoms attain an appropriate mobility. Furthermore, a glass is metastable with respect to crystalline phase(s) and transform to the latter through nucleation and growth. On heating, a glass would transform to the liquid phase provided that the rates of crystallization are sluggish enough.

Glasses are generally formed if upon cooling of a melt crystal nucleation and/or growth are avoided. At a temperature called glass transition temperature (T_g) the liquid freezes to a rigid solid, however without crystalline order. Thus, glasses and amorphous solids in general are structurally characterized by the absence of long-range translational

order. But a short-range order is still present and may be similar to that found in the crystalline counterpart.

Synthesizing amorphous alloys requires rapid solidification, in order to by-pass the crystallization [3.3]. The metastable structure thus achieved nevertheless may possess a short-range order (SRO) that resembles the equilibrium crystal structure [3.4]. This indicates that the thermodynamic forces that drive crystallization in metals are extremely strong and in most cases, overpowering. Thus the search for alloy systems that allow formation of amorphous structures is of keen technological importance.

Fig. 3.1 shows schematically, the time taken for a small amount of crystalline phase to form in an undercooled liquid as a function of temperature. The Temperature-Time-Transformation (TTT) diagram shows a characteristic C curve behavior. At the temperature close to melting point T_m there is little driving force for crystallization, so that the crystal nucleation and growth rates are small, and the crystallization onset time t_0 is large. As the temperature decreases, the crystallization onset time reaches a minimum value t_0^* at a temperature T_n , and then increases again as the thermal energy becomes insufficient for atomic motion. Close to the glass transition temperature (T_g) atomic motion is completely suppressed and the amorphous structure is frozen in, so that the crystallization onset time t_0 becomes large. Therefore, critical cooling rate R_c to avoid crystallization is given below:

$$R_c = \frac{T_m - T_n}{t_0^*} \quad (3.1)$$

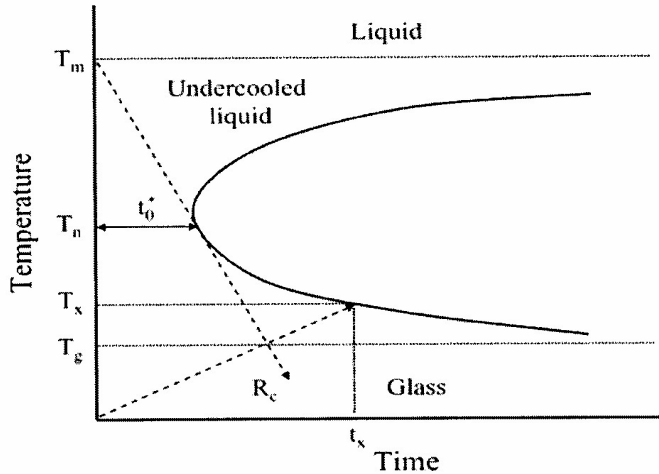


Fig.3.1 Schematic TTT diagram for the onset of crystallization

The absence of long-range order is easily determined using X-ray diffraction (XRD) or transmission electron microscopy (TEM). In XRD for example, broad diffuse halo peaks are observed ($2\theta \sim 10^\circ$) broadness with Cu- $K\alpha$, instead of the sharp Bragg peaks shown by crystalline phase.

3.2 The Glass Transition Temperature

Apart from the lack of LRO, an important characteristic of any amorphous structure is the glass transition temperature (T_g). The glass transition is the phenomenon in which a glass exhibits a more or less abrupt change in derivative thermodynamic modulus from crystal-like to liquid-like values with change of temperature. When a liquid is cooled, one of the following two events may occur; either crystallization may take place at the melting point T_m or the liquid will become supercooled below T_m . If the liquid is supercooled sufficiently, its density gradually falls and its viscosity gradually rises. Thus macroscopic flow of the liquid becomes progressively more difficult. These changes can be observed by monitoring the volume of the supercooled liquid as a function of temperature and a typical result is shown schematically in fig.3.2 [3.5].

The crystallization process is manifested by an abrupt change in volume at T_m , where glass formation is characterized by a gradual break in slope. The region over which the change of slope occurs is termed the glass transition temperature T_g .

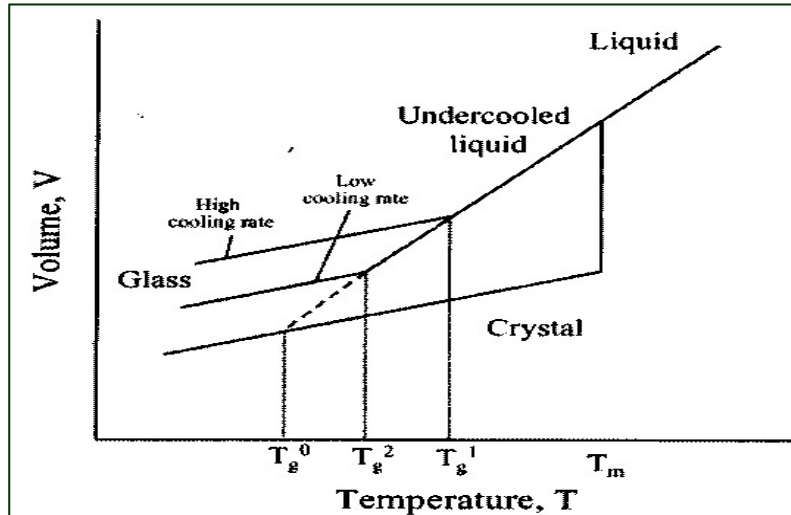


Fig. 3.2 Volume-Temperature relationship in solid, liquid and glassy state

The glass transition temperature is the point at which the alloy finally solidifies with frozen-in amorphous atomic structure. Freezing the amorphous structure at the glass transition temperature is a kinetic rather than a thermodynamic transition. Decreasing the cooling rate gives more time for atomic motion, allowing the liquid to maintain its equilibrium structure to lower glass transition temperature, with a denser, lower entropy structure. The temperature of the glass transition is not a constant of the material, but is a function of experimental conditions. The volume (ΔV) and entropy (ΔS) difference between the liquid and the crystal decrease progressively as the temperature falls, and approach zero at a temperature called the ideal glass transition temperature T_g^0 .

Kauzmann [3.6] was the first to point out that an amorphous structure with higher density and lower entropy than the corresponding crystal is impossible, so T_g^0 is the

natural lower limit of the range of possible glass transition temperatures, corresponding to a condition of an infinitely slow cooling rate. In general the glass transition temperature, T_g is defined as the temperature at which an amorphous solid, such as glass or a polymer, becomes brittle on cooling, or soft on heating. More specifically, it defines a pseudo second order phase transition in which a supercooled melt yields, on cooling, a glassy structure and properties similar to those of crystalline materials e.g. of an isotropic solid material [3.7]. The glass transition temperature can be measured by using differential scanning calorimetry (DSC)

3.3 Stability of the amorphous phase

Amorphous materials are always in a metastable state, which tend to transform into more stable crystalline phases. There are three kinds of stability of significance for amorphous magnetic alloys: their resistance to the initiation of crystallization, structural relaxation effects and the relaxation or reorientation of directional order. At temperature below the crystallization temperature, structural relaxation takes place due to atomic rearrangement. The formation and resultant stability of amorphous alloys are important topics both theoretically and technologically. The theoretical analysis of the factors controlling the ease of formation and the stability of the resultant amorphous alloys have been extensively reviewed [3.8-3.10] From the thermodynamic view point [3.9-3.10], the ability of an alloy to be quenched into the glassy state is generally measured by the magnitude of the quantity.

$$\Delta T_g = T_m - T_g, \quad (3.2)$$

where T_m and T_g are the melting and glass transition temperature respectively. In a similar manner the stability of the glass after formation is generally measured by the magnitude of the quantity.

$$\Delta T_x = T_x - T_g \quad (3.3)$$

where T_x is the temperature for the onset of crystallization. As the temperature decreases from T_m the rate of crystallization will increase rapidly and then fall rapidly as the temperature decreases below T_g . Thus if one quenched a molten alloy rapidly

enough to temperature below T_g a quasi-equilibrium amorphous phase is obtained. There is no direct relation between the ease of formation and the resultant stability of an amorphous alloy.

3.4 Crystallization of the amorphous state

The basic principle for the crystallization method from amorphous solids is to control the crystallizations kinetics by optimizing the heat treatment conditions (annealing temperature and time, heating rate, etc) so that the amorphous phase crystallizes completely into a polycrystalline material with ultrafine crystallites. Crystallization of amorphous alloy solid has been successfully applied in producing nanometer –sized polycrystalline materials in various alloy systems, e.g. in Fe-, Ni-, and Co- based alloys [3.11-3.15]. The complete crystallization of amorphous solids is being established as a promising method for synthesis of nanocrystalline materials because it possesses some unique advantages:

- (i) It is very simple and convenient to control in preparation procedures. Conventional annealing can realize the nanocrystallization in most alloy and element systems provided they are formed into grain sizes with a wide size range (from a few nanometers to submicrometers) can be easily obtained in the as-crystallized nanocrystalline specimens by simply modifying the heat treatment conditions [3.16];
- (ii) The complete crystallization method is an efficient way to produce porosity-free nanocrystalline materials [3.17]. As no artificial consolidation process is involved and the nanometer-crystallites and their boundaries are formed via a solid-state phase transformation, the nanocrystalline samples are dense and clean in the internal interfaces;
- (iii) The nanocrystallization itself provides us with a unique chance to study the interface formation process from the amorphous state experimentally. The nanocrystallization kinetics and thermodynamics of the amorphous solids are strongly affected by the presence of plenty interfaces in the crystallization products [3.18, 3.19].

Consequently, it is possible to reveal some fundamental features of the interfaces in the nanocrystalline materials from the transformation kinetic and thermodynamic signals [3.20].

The crystallization is associated with nucleation and growth process. The kinetics of loss of metastability of the amorphous state (disordered system) above the glass transition, i.e. under far from equilibrium conditions, is a key subject since it provides new opportunities for structure control by innovative alloy design and processing strategies. Several examples include soft and hard magnets and high strength materials [3.21-3.22]. Most studies focus on the crystallization onset as a measure of kinetic stability under heat treatment and recognize the product phase selection involved in nucleation and the role of competitive growth kinetics in the evolution of different microstructural morphologies [3.23]. The transition to the crystalline state is accompanied by an exothermic heat effect-giving rise to a sharp peak in the temperature dependence of the exothermic heat. Therefore, differential scanning calorimetry (DSC) is a widely used technique to study thermally induced transformations in amorphous alloys and to determine the crystallization temperature (T_x). The magnitude of T_x is very different for amorphous materials and depends strongly on composition. The activation energy ranges typically between 2 and 6 eV. Calorimetric measurements are, however, integral techniques, which give no information about the microstructural development. DSC measurement under continuous heating is quite straightforward; where as isothermal measurements are time consuming and can be performed only in a limited temperature range because of the thermally activated nature of the process. The continuous heating calorimetric signal shows a significant increase in the maximum value of the exothermic heat flux with increasing heating rate. Such a behavior is typical of a thermally activated process.

Activation energy is one of the important parameters describing the transformation kinetics. The activation energy for the isothermal nanocrystallization is usually determined according to the Arrhenius relation:

$$t = t_0 \exp\left(\frac{E}{RT}\right), \quad (3.4)$$

where t is a characteristic time, t_0 is a time constant, R is the gas constant and E is the activation energy for the transformation [3.19]. For the anisothermal nanocrystallization process, where the heating rate dependence of DSC thermogram is recorded the Kissinger relation is frequently used for determination of activation energy, which is expressed as: [3.24]

$$\ln\left(\frac{\beta}{T^2}\right) = -\frac{E}{RT} + \text{Constant} \quad (3.5)$$

where β is the heating rate and T is a characteristic temperature corresponding to peak temperature. By plotting $\ln\left(\frac{\beta}{T^2}\right)$ against $\frac{1}{T}$ one can derive the value of E from the slope of the straight line. Using the characteristic temperatures measured from the DSC, one can make Kissinger plots according to the above equation. It was also found that the value of E is smaller in the beginning of the transformation (about 225 KJ mol^{-1}) than that in the later stages (about 260 KJmol^{-1})[3.25]. Although the values of activation energy for the nanocrystallization process determined from the Arrhenius plot and from the Kissinger plot are different, a common behavior of the variation in activation energy at different stages is obtained.

The activation energy for the crystallization is also found to be related to the nature of the amorphous state and temperature as well. A decrease of the degree of amorphism in the original amorphous state will reduce the value of E . E values are found to be larger at higher temperatures in crystallization. These features probably originate from the crystallization micromechanism [3.26]

3.5 Theory of Magnetism

3.5.1 Introduction to Magnetic Ordering

The basic criteria for the onset of magnetic order in solids are (i) individual atoms should have magnetic moments (spins) and (ii) exchange interactions must exist between the atoms that couple them together. Exchange coupling originates from the overlapping of the electronic wave functions with those of neighboring atoms. The exchange interactions depend sensitively upon the interatomic distance and the nature of the chemical bonds, particularly of nearest neighbor atoms.

A system is characterized by its energy in order to describe the magnetic configuration of a system as proposed by Heisenberg according to the following Hamiltonian [27].

$$H_j = - \sum_{i,j} J_{ij} \vec{S}_i \cdot \vec{S}_j \quad , \quad (3.6)$$

where J_{ij} is the exchange-coupling constant between the spins \vec{S}_i and \vec{S}_j distributed on a regular lattice. Only nearest neighbors are included in the summation. The magnetic property of the system is thus dependent on the sign and strength of the interaction between the spins. If $J_{ij} = J > 0$, parallel orientation of the spins is favored and at low temperatures all spins will be aligned ferromagnetically. At high temperatures the entropy dominates the interaction energy and the spins will fluctuate independently with the manifestation of paramagnetic phase, while at lower temperatures the interaction energy dominates and the system will order at the critical temperature (T_c) with all the spins pointing in the same direction with the appearance of ferromagnetic phase.

For if $J_{ij} = J < 0$, the low temperature phase is antiferromagnetic with the spins aligned antiparallel to their neighbors below a characteristic temperature T_N , called the Neel temperature. Above T_N the material exhibit paramagnetic behavior. In the simplest case, the lattice of an antiferromagnet is divided into two sublattices with the magnetic moments of these in antiparallel alignment. This gives rise to zero net magnetization. A

special case of antiferromagnetism is ferrimagnetism. In ferrimagnetism there are also two sublattices with magnetic moments in opposite directions, but the magnetization of the sublattices are of unequal strength resulting in a non-zero magnetization and therefore has net spontaneous magnetization. At the macroscopic level of domain structures, ferromagnetic and ferrimagnetic materials are therefore similar. The Curie and Neel temperatures characterize a phase transition between the magnetically ordered and disordered (paramagnetic) states.

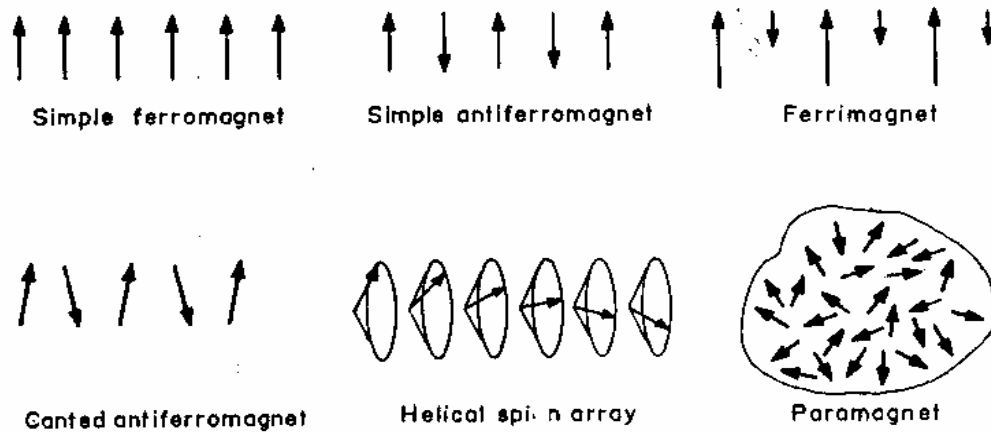


Fig.3.3 Examples of different types of magnetic order using a linear array of localized moments, including paramagnet

If $J_{ij} = J = 0$, the Hamiltonian describes a system being paramagnetic at all temperatures with all the spins pointed at random resulting in zero magnetic moment. Besides these common type of magnetic ordering, various other type of magnetic structures such as canted, helical and conical spin arrangements may exist which are shown in the above fig. 3.3

3.5.2 Ferromagnetism and Magnetic domain

At a first glance the coexistence of long-range ferromagnetic ordering with a structurally disordered material seems to be incompatible. However, the very short-range ordered structure in the glassy state does not differ significantly from that in the corresponding crystalline material. The ferromagnetism is supposed to arise from interactions between neighboring atomic moments, which make them to align parallel. In 1928 Heisenburg [3.27] described the quantum mechanical origin of ferromagnetism, by considering the interaction between electronic spins. The spins of the neighboring electrons are coupled and in this way all the spins are oriented in the same direction. This parallel alignment of the spins gives rise to a macroscopic magnetic moment. The coupling can be expressed as shown in equation (3.6).

In the demagnetized state, ferromagnets show no net magnetization. But they are spontaneously decomposed in small regions named magnetic domains within which the magnetic moments are ordered. The magnitude of magnetization in all domains is the same but the direction varies from one domain to the other. Thus, a demagnetized state with zero net magnetization is possible fig.3.4 (a)

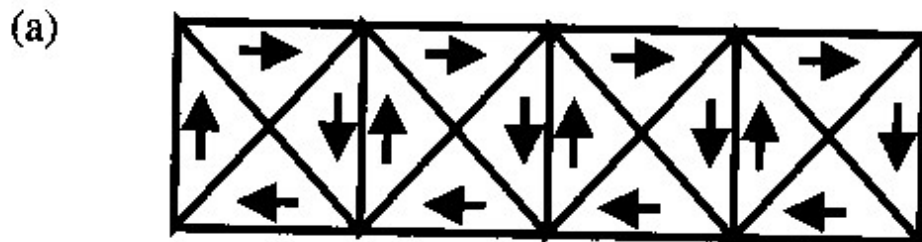


Fig. 3.4(a) Magnetic domains in a ferromagnetic material in the demagnetized state

A ferromagnetic body has magnetostatic energy. The magnetic domains are generated spontaneously in order to minimize this energy until the energy consumed for the formation of a new domain is higher than the corresponding lowering of the magnetostatic energy. The directions of the magnetic moments are not changed

suddenly from one domain to another but rotate gradually within the domain walls as shown in fig.3.4 (b) [3.28].

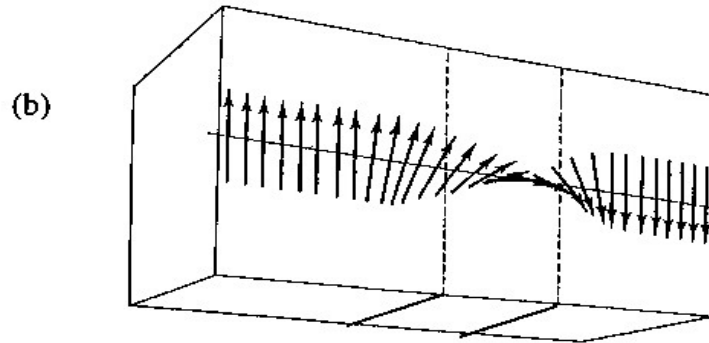


Fig.3.4 (b) Rotation of magnetic moments within a domain wall

The domain wall width can be even of the order of 100 nm. The vectorial sum of all moments \vec{m} relative to the entire volume of the ferromagnetic body is called volume magnetization \vec{M}_v . In the demagnetized state, the magnetic moments are randomly oriented. The vectorial sum of the magnetic moments is zero and therefore, the total magnetization is zero [3.28].

In the magnetic domains, atomic magnetic moments are aligned due to the internal Weiss field or alternatively the ferromagnetic exchange interaction. The magnetization process involves the growth of domains that are favorably oriented with the applied magnetic field at the expense of those that are not.

Having more than one domain requires an interfacial region between domains called a domain wall. Associated with this interface is positive domain wall energy. A balance between the volume, magnetostatic and interfacial domain wall energies determines the ultimate number and size, of magnetic domains in a sample. In soft materials, which have been optimized to have very low rotational energy barriers, the major determinant of the shape of the magnetization curve is domain wall motion.

We will find it useful to describe several length scales that are associated with domains and domain walls. These are expressed through consideration of domain wall energetic.

The energy per unit area in the wall can be expressed as a sum of exchange and anisotropy energy terms:

$$\gamma_{\text{wall}} = \gamma_{\text{ex}} + \gamma_{\text{k}} , \quad (3.7)$$

where A_w is area of the domain wall, δ_w is domain wall width, the anisotropy energy per unit volume, K_1 , is multiplied by volume contained in a domain wall, $A_w \delta_w$, and divided by cross-sectional area to arrive at an anisotropy energy per unit area:

$$\gamma_{\text{k}} = K_1 \left(\frac{A_w \delta_w}{A_w} \right) = K_1 \delta_w = K_1 (N_p a) , \quad (3.8)$$

where $\delta_w = Na$ (a is the lattice constant in the direction of rotation and N is the number of planes over which the rotation takes place) is the thickness of the wall.

Thus γ_{wall} can be expressed:

$$\gamma_{\text{wall}} = \frac{\pi^2 J_{\text{ex}} S^2}{N_p^2} + K_1 N_p a , \quad (3.9)$$

where the first term considers the cost in exchange energy in rotating magnetic dipole moments in a 180° domain wall as illustrated in the above fig. 3.4 (b). To determine the optimal wall thickness we differentiate γ_w with respect to δ_w

$$\frac{1}{a} \frac{\partial \gamma_{\text{wall}}}{\partial N_p} = 0 = \frac{\pi^2 J_{\text{ex}} S^2}{N_p^2 a^2} + K_1 \quad (3.10)$$

yielding:

$$N_{\text{eq}} = \sqrt{\frac{\pi^2 J_{\text{ex}} S^2}{K_1 a^3}} \quad (3.11)$$

For Fe, $N_{\text{eq}} \sim 300$ and the equilibrium thickness, $t_{\text{eq}} = N_{\text{eq}} a \sim 50$ nm. Expressed in terms of the exchange stiffness, A_{ex} , the domain wall width, δ_w is:

$$\delta_w = \pi \sqrt{\frac{A_{\text{ex}}}{K_1}} \quad (3.12)$$

Another important length scale is the distance over which the perturbations due to the switching of a single spin decays in a soft material. This length is called the ferromagnetic exchange length (L_{ex}) and can be expressed:

$$L_{ex} = \sqrt{\frac{A_{ex}}{\mu_0 M_s^2}} \quad (3.13)$$

The ferromagnetic exchange length is $\sim 3\text{nm}$ for ferromagnetic iron or cobalt-based alloys. The ratio of the exchange length to $\frac{\delta_w}{\pi}$ is a dimensionless parameter (k) called the magnetic hardness parameter:

$$K = \frac{\pi L_{ex}}{\delta_w} = \sqrt{\frac{K_1}{\mu_0 M_s^2}} \quad (3.14)$$

For hard magnetic materials k is in the order of unity and thus there is little difference between the ferromagnetic exchange length and the domain wall width. On the other hand, for good soft magnetic materials, where K_1 approaches zero, can deviate substantially from unity.

Structure sensitive magnetic properties may depend on defect concentration (point, line and planar defects), atomic order, impurities, second phases, thermal history, etc. In multi-domain materials, the domain wall energy density,

$$\gamma = 4(AK_1)^{\frac{1}{2}} = \gamma(x) \quad (3.15)$$

is spatially varying as a result of local variations in properties due to chemical variation, defects, etc. A domain wall will prefer to locate itself in regions where the magnetic order parameter is suppressed, i.e. pinning sites. Since changes in induction in high-permeability materials occur by domain wall motion, it is desirable to limit variation of $\gamma(x)$ (pinning). This is one of the key design issues in developing soft magnetic materials.

3.5.3 Random Anisotropy Model (RAM) and Strongly Exchanged Coupled Nanocrystalline Alloys

In a discussion of the benefits of nanocrystalline alloys for soft magnetic applications the extrinsic properties the coercivity and the permeability need to be considered. Reductions of coercivity increase in permeability are both desirable properties that can be considered in selecting amorphous and nanocrystalline alloys.

The concept of a magnetic exchange length and its relationship to the domain wall width and monodomain size is important in the consideration of magnetic anisotropy in nanocrystalline soft magnetic materials [3.29]. As described above, these can be defined by appealing to a Helmholtz free energy function as described by Coey [3.30]. These length scales are:

$$\delta_w = \pi \sqrt{\frac{A}{K}}, \text{ and } L_{ex} = \sqrt{\frac{A}{4\pi M_s^2}} \quad (3.16)$$

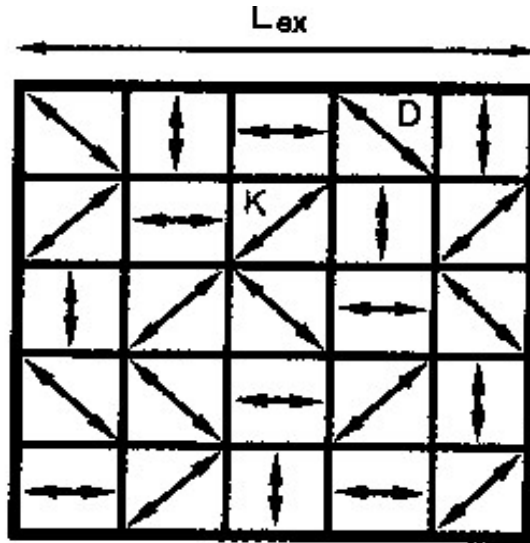


Fig.3.5 Schematic representation of the random anisotropy model. The arrows indicate the randomly fluctuating magnetocrystalline anisotropies

The extension of the random anisotropy model (RAM) by Herzer [3.31-3.35] to nanocrystalline alloys has also been used as the premise for explaining the soft magnetic

properties of these materials. RAM has been originally developed by Alben *et al.*(3.36) in order to explain the soft magnetic properties of amorphous ferromagnets. The Herzer argument for effective anisotropies in nanocrystalline materials builds on the arguments of the random anisotropy model presented for amorphous alloys presented above. Herzer considers a characteristic volume, whose linear dimension is the magnetic

exchange length, $L_{ex} \sim \left(\frac{A}{K_1} \right)^{1/2}$ as shown in fig. 3.5.

Given the discussion above the unstated constant of proportionality should be k/π , which for materials with very small k can in fact be quite large. Ignoring this constant of proportionality, the Herzer arguments consider N grains, with random easy axes, within a volume of L_{ex}^3 to be exchange coupled. Since the easy axes are randomly oriented, a random walk over all N grains will yield an effective anisotropy, which is reduced by a factor of $\frac{1}{(N_p)^2}$ from the value k_1 for any one grain, thus $K_{eff} = \frac{K}{(N_p)^2}$.

Now the number of grains in this exchange-coupled volume is just $N = \left(\frac{L_{ex}}{D_g} \right)^3$, where

D_g is the average diameter in individual grains. Treating the anisotropy self-consistently, then:

$$K_{eff} \sim \left(\frac{K_1^4 D_g^6}{A^3} \right) \quad (3.17)$$

Since the coercivity can be taken as proportional to the effective anisotropy, this analysis leads to Herzer's prediction that the effective anisotropy and therefore the coercivity should grow as the 6th power of the grain size:

$$H_c \sim H_k \sim D_g^6 \quad (3.18)$$

For such a reduction in the coercivity to be realized, Herzer noted that the nanocrystalline grains must be exchange coupled.

The most significant feature predicted by the random anisotropy model is the strong variation of K_{eff} with the sixth power of the grain size. Thus $D \approx \frac{L_0}{3}$ i.e., grain sizes in the order of 10-15 nm, the magneto-crystalline anisotropy is reduced by three orders of magnitude towards a few J/m^3 , i.e., small enough to enable superior soft magnetic behavior. Correspondingly the renormalized exchange length (L_{ex}), expands into the μm -regime and thus, is almost two orders of magnitude larger than the natural exchange length L_0 . High-resolution Kerr effect studies of nanocrystalline $\text{Fe}_{73.5}\text{Cu}_1\text{Nb}_3\text{Si}_{13.5}\text{B}_9$ indeed reveal very wide domain walls of about $2 \mu\text{m}$ in thickness indicative of the low effective anisotropy of the material [3.37]

If there are no other anisotropies, coercivity and initial permeability are closely related to K_{eff} by

$$H_c = p_c \frac{K_{\text{eff}}}{J_s} \quad (3.19)$$

$$\mu_i = p_\mu \frac{J_s^2}{\mu_0 K_{\text{eff}}} \quad (3.20)$$

where J_s is the average saturation magnetization of the material, p_c and p_μ are dimensionless pre-factors close to unity. These relations, obvious for coherent magnetization rotation, in the regime $D \ll L_{\text{ex}}$, also apply for domain wall displacements [3.32], on the scale of the 10 nm small grains the magnetization vector appears to rotate coherently if a $2 \mu\text{m}$ ($\ll L_{\text{ex}}$) wide domain wall passes by. Besides very low or vanishing magnetocrystalline anisotropy, another major requirement for superior soft magnetic properties is that the saturation magnetostriction (λ_s) should be very low to avoid magnetoelastic anisotropies arising from internal mechanical stresses. The low magnetostriction of nanostructured materials can be understood from the balance of the magnetostriction between the $\alpha\text{-Fe}(\text{Si})$ crystallites with negative and amorphous matrix with positive value and usually given by [3.38]:

$$\lambda_s^{\text{nano}} = V_{\text{Fe}(\text{Si})} \lambda_s^{\text{Fe}(\text{Si})} + (1 - V_{\text{Fe}(\text{Si})}) \lambda_s \quad (3.21)$$

where $\lambda_s^{Fe(Si)}$ and λ_s^{am} stands for the magnetostriction constants of the α -Fe-Si grains and the residual amorphous matrix, respectively. The higher permeability of the nanocrystalline samples in the first approximation can be expressed in terms of effective magnetic anisotropy constant $\langle K_{eff} \rangle$ and magneto-elastic energy according to Stoklosa et al. [3.39].

$$\mu_i = \frac{M_s^2}{\left\{ 2\mu_0 \left(\langle K_{eff} \rangle + \frac{3\lambda_s \sigma}{2} \right) \right\}} \quad (3.22)$$

where, M_s is the saturation magnetization, μ_0 is the vacuum magnetic permeability, σ is the effective stress.

The analysis of the experimental data of Yoshizawa et al. [3.40] and Herzer [3.32-3.34] show $\lambda_s^{amor} = 20 \times 10^{-6}$ (for as cast), $\lambda_s^{Fe(Si)} = -6 \times 10^{-6}$ for conventional polycrystalline α -Fe(Si) and $\lambda_s^{nano} = 2 \times 10^{-6}$ for nanocrystallized samples at 550°C, Thus λ_s for annealed sample is about one order of magnitude lower. Moreover, the effective stress (σ) is substantially reduced if not completely eliminated by heat treatment. Thus the increase of initial permeability on the formation of the nanocrystalline state is closely related to a simultaneous decrease of λ_s . However, the best soft magnetic properties are not necessarily to be found on the $\lambda_s = 0$ line but for compositions where the total amount of magnetoelastic and effective magnetic anisotropy is minimized.

3.5.4 AC Magnetic Response to the Soft Magnetic Materials

Soft magnetic material's magnetic loss mechanisms include: (i) hysteresis loss due to irreversible domain wall motion and rotational out of easy axes loss mechanism, (ii) eddy current losses and (iii) anomalous losses. The energy loss per cycle is given by $\oint B dH$ and for linear response the power loss is $\frac{f \times B^2}{2\mu}$, where f is the frequency. In real materials (which are nonlinear) we express the hysteresis power loss as:

$$P_h \sim C_h f B_{\max}^n \quad (3.23)$$

where C_h may vary with the material, and a typical exponent n is ~ 1.6 . Eddy current loss results from the fact that $\frac{d\phi}{dt}$ induces voltages in the core material with consequent $\frac{V^2}{R}$ power loss appearing as heat. This power loss can be reduced by decreasing V and increasing R . Since $V \sim f B_{\max}$ then the power loss due to eddy currents is proportional to $f^2 B_{\max}^2$ i.e:

$$P_e = C_e f^2 B_{\max}^2 \quad (3.24)$$

To reduce the eddy current loss in sheet transformers, they are often laminated so as to reduce the length scale of eddy current loops. In designing transformers the total power loss:

$$P_{\text{tot}} = P_h + P_e = C_h f B_{\max}^n + C_e f^2 B_{\max}^2 \quad (3.25)$$

must be minimized.

The important physical parameters, which can be altered to minimize alternating current (AC) losses are those influencing the hysteresis loss as described above and those, which influence the eddy current losses. By and large the most important physical

parameter, which influences the eddy current losses and therefore the high frequency losses, is the electrical resistivity (ρ). Large electrical resistivities are essential for reducing AC losses. Electrical resistivities in amorphous alloys can be several hundred $\mu\Omega$ -cm and for nanocrystalline alloys $\sim 50 \mu\Omega$ cm, which in both cases offer significant advantage over crystalline metallic magnetic materials ($\sim 1-10 \mu\Omega$ cm).

3.5.5 Temperature dependence of magnetization

The mean-field theories do not account for local magnetic excitations and thus cannot provide an accurate description of the low temperature behavior of the magnetic properties. This problem can be solved by the spin-wave theory. In the quasicrystalline approximation and the long-wavelength limit, the spin-wave energy can be expressed by [3.41].

$$E_k = E_0 + Dk^2 + Fk^4 + \dots, \quad (3.26)$$

where k is the wave vector of the spin wave and D and F are the spin-wave stiffness constants.

It has been well established that amorphous metallic alloys exhibit well-defined spin wave excitation. A number of experiments performed by Mössbauer [3.42], inelastic neutron scattering [3.43] and magnetization measurements [3.44-3.45]. It has been shown that as in crystalline ferromagnets the long wavelength magnetic excitation in amorphous ferromagnets are also spin waves. At low temperature spontaneous magnetization varies with temperature. Usually the magnetization at low temperatures is found to decrease with increasing temperature in accordance with the predictions of an isotropic nearest-neighbor Heisenberg model shown in equation (3.27) below and it vanishes at a temperature, called Curie temperature, T_c . The Curie temperature separates the disordered paramagnetic state at $T > T_c$ from the ordered magnetic state at $T < T_c$. The presence of spin-waves gives rise to a reduction of the average magnetization leading to a temperature dependence of the form [3.46]:

$$M(T) = M(0) \left(1 - BT^{\frac{3}{2}} - CT^{\frac{5}{2}} \right) \quad (3.27)$$

$$\frac{\Delta M}{M(0)} = \frac{M(0) - M(T)}{M(0)} = BT^{\frac{3}{2}} + CT^{\frac{5}{2}} \quad (3.28)$$

In the above equation $M(0)$ is the saturation magnetization at 0 K and can be obtained by extrapolation of the low temperature magnetization data, $M(T)$ to zero Kelvin . Generally, the low temperature behavior of the saturation magnetization of crystalline ferromagnetic materials can be described within reasonable errors by the first term of equation (3.27) and known as Bloch's $T^{3/2}$ law covering a narrow range of temperature i.e. $0.2 T_c$.

The coefficients B and C are related to the spin-wave stiffness constant D by

$$B = \zeta \left(\frac{3}{2} \right) \left(\frac{g\mu_B}{M_s(0)} \right) \left(\frac{k_B}{4\pi D} \right)^{\frac{5}{2}} \quad (3.29)$$

and

$$C = \frac{3}{4} \pi \langle r^2 \rangle \zeta \left(\frac{5}{2} \right) \left(\frac{g\mu_B}{M_s(0)} \right) \left(\frac{k_B}{4\pi D} \right)^{\frac{5}{2}} \quad (3.30)$$

$\zeta \left(\frac{3}{2} \right) = 2.612$ and $\zeta \left(\frac{5}{2} \right) = 1.341$ are the Reiman zeta functions and the mean-square

value of the range of exchange interaction $\langle r^2 \rangle$ was calculated by using the relation

$$\langle r^2 \rangle = \frac{16}{3k_B} \frac{\zeta(3/2)}{\zeta(5/2)} \left(\frac{CD}{B} \right) \quad (3.31)$$

The general variation of the reduced magnetization $\frac{M(T)}{M(0)}$ versus the reduced

temperature $\frac{T}{T_c}$ is shown in fig. 3.6.

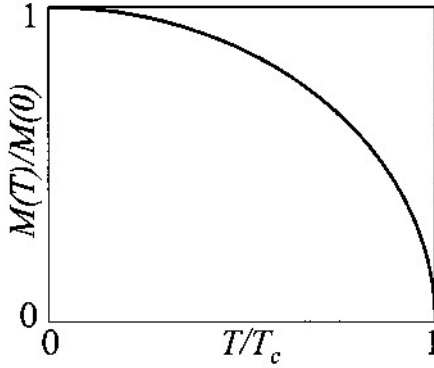


Fig. 3.6 Reduced magnetization $\frac{M(T)}{M(0)}$ versus reduced temperature $\frac{T}{T_c}$ curve

In many cases [3.47] considering the higher temperature term $T^{5/2}$ the equation (3.28) fits the experimental data from very low temperatures up to a temperature close to $0.6 T_c$ to $0.8 T_c$. When the temperature is higher approaching towards T_c , the experimental behavior can be described well by the following equation [3.48, 3.34]

$$M(T) = M(0) \left(1 - \frac{T}{T_c}\right)^\beta \quad (3.32)$$

with the exponent β close to the Heisenberg value $\beta = 0.36$

Bhagat et al. [3.47] from the experimental results of temperature dependence of magnetization in amorphous alloys showed that if $\langle r^2 \rangle$ values are rather high, the constant B from equation (3.27) can no more be treated as a constant since the stiffness constant D is also temperature dependent by the equation

$$D(T) = D(0)(1 - T)^v \quad (3.33)$$

with $2 \leq v \leq 3$ according to Handrich et al [3.46].

3.5.6 Initial permeability of Nanocrystalline alloys

3.5.6.1 Theories of Permeability

The primary requirement for the soft magnetic materials is the highest possible permeability, together with low losses in the frequency range of interest. The initial permeability (μ_i) is defined as the derivative of induction \mathbf{B} with respect to the initial field \mathbf{H} in the demagnetization state.

$$\mu_i = \frac{dB}{dH}, H \rightarrow 0, B \rightarrow 0 \quad (3.34)$$

At microwave frequency, and also in low anisotropic amorphous materials, dB and dH may be in different directions, the permeability thus a tensor character. In the case of amorphous materials containing a large number of randomly oriented magnetic atoms the permeability will be scalar. As we have

$$B = \mu_0(H + M) \quad (3.35)$$

and susceptibility,

$$\chi = \frac{dM}{dH} = \frac{d}{dH} \left(\frac{B}{\mu_0} - H \right) = \frac{1}{\mu_0}(\mu - 1) \quad (3.36)$$

The magnetic energy density

$$E = \frac{1}{\mu_0} \int H \cdot dB \quad (3.37)$$

For time harmonic fields $H = H \sin \omega t$, the dissipation can be described by a phase difference δ between \mathbf{H} and \mathbf{B} . In the case of permeability, defined as the proportional constant between the magnetic field induction \mathbf{B} and applied intensity \mathbf{H} ;

$$\mathbf{B} = \mu \mathbf{H} \quad (3.38)$$

This naive definition needs further sophistication. If a magnetic material is subjected to an ac magnetic field as we get,

$$H = H_0 e^{i\alpha t} \quad (3.39)$$

Then it is observed that the magnetic flux density B experiences a delay with respect to applied AC field, H_{ac} . This is caused due to the presence of various losses and is thus expressed as,

$$B = B_0 e^{i(\alpha t - \delta)} \quad (3.40)$$

where δ is the phase angle and marks the delay of B with respect to H , the permeability is then given by

$$\begin{aligned} \mu &= \frac{B}{H} \\ &= \frac{B_0 e^{i(\alpha t - \delta)}}{H_0 e^{i\alpha t}} \\ &= \frac{B_0 e^{-i\delta}}{H_0} \\ &= \frac{B_0}{H_0} \cos \delta - i \frac{B_0}{H_0} \sin \delta \\ \mu &= \mu' - i\mu'' \quad , \end{aligned} \quad (3.41)$$

$$\text{where } \mu' = \frac{B_0}{H_0} \cos \delta \quad (3.42)$$

$$\text{and } \mu'' = \frac{B_0}{H_0} \sin \delta \quad (3.43)$$

The real part μ' of complex permeability μ as expressed in equation (3.41) represents the component of B , which is in phase with H , so it corresponds to the normal permeability. If there are no losses, we should have $\mu = \mu'$. The imaginary part μ'' corresponds to that part of B , which is delayed by phase δ from H . The presence of such a component requires a supply of energy to maintain the alternation magnetization, regardless of the origin of delay. It is useful to introduce the loss factor or loss tangent ($\tan \delta$). The ratio of μ'' to μ' , as is evident from equation gives.

$$\frac{\mu''}{\mu'} = \frac{\frac{B_0}{H_0} \sin \delta}{\frac{B_0}{H_0} \cos \delta} = \tan \delta \quad (3.44)$$

This $\tan \delta$ is called the loss factor. The Q-factor or quality factor, which is called the merit of the material, is defined as the reciprocal of this loss factor i.e.

$$Q = \frac{1}{\tan \delta} \quad (3.45)$$

and the relative quality factor = $\frac{\mu'}{\tan \delta}$. The behavior of μ' and μ'' versus frequency is called the permeability spectrum. The initial permeability of a ferromagnetic substance is the combined effect of the wall permeability and rotational permeability mechanism.

Experimental

4.1 Sample Preparation

4.1.1 Master alloy preparation

A series of amorphous ribbons with composition of $\text{Fe}_{73.5-x}\text{Cr}_x\text{Cu}_1\text{Nb}_3\text{Si}_{13.5}\text{B}_9$ alloys with $x = 1, 2, 3, 4, 5, 6, 7, 8, 9, 10, 12.5, 15$ & 17.5 were prepared in an arc furnace on a water-cooled copper hearth under an atmosphere of pure Ar. Their purity and origin of the constituent elements were Fe (99.98%), Cu (99+%), B (99.5%), Si (99.9%), Nb (99.8%) and Cr (99.99%) as obtained from Johnson Matthey (Alfa Aesar Inc.). The required amounts of constituent elements were taken from pure metal bars or flakes weighed carefully with a sensitive electronic balance and placed on the copper hearth inside the arc furnace. Before melting the furnace chamber was evacuated (10^{-4} torr) and flashed with Ar gas. The process was repeated several times to get rid of residual air and finally the furnace chamber was kept in an Ar atmosphere.



Fig.4.1 Vacuum arc melting machine

A substantial amount of pure Titanium getter, placed inside of the chamber on the side of the copper hearth was melted first in order to absorb any oxygen present in the

furnace chamber. The constituent elements were then melted in the shape of buttons. The arc melting facilities used to prepare the samples are installed at the Centre for Materials Science, National University of Hanoi, Vietnam. The arc furnace used in the preparation of master alloys is shown in figure 4.1.

4.1.3 Preparation of ribbon by rapid quenching

Melt-spinning is a widely used production method for rapidly solidifying materials as well as preparing amorphous metallic ribbon [4.1-4.2]. In order to prepare amorphous of $Fe_{73.5-x}Cr_xCu_1Nb_3Si_{13.5}B_9$ alloys with $x = 1, 2, 3, 4, 5, 6, 7, 8, 9, 10, 12.5, 15$ and 17.5 , a melt spinning facilities was used at the Centre for Materials Science, National University of Hanoi, Vietnam. The arc melted master alloy was crashed into small pieces and put inside the quartz tube crucible for re-melting by induction furnace using a medium frequency generator with a maximum power of 25 kW at a nominal frequency of 10 kHz.



Fig. 4.2 Melt-spinning Mechine

Fig. 4.2 shows the pictorial view of the melt-spinning machine. The quartz crucible has in its bottom part a rectangular nozzle tip of 8 mm length and 0.7 mm width. The position of the nozzle tip can be adjusted with respect to the copper wheel surface, so that the molten alloy was perpendicularly ejected onto the wheel surface from a distance of about 0.3 mm. The small pieces of the master alloy samples were inductively remelted inside the quartz tube crucible followed by ejecting the molten metal with an over pressure of 250 mbar of 99.9% pure Ar supplied from an external reservoir through a nozzle onto a rotating copper wheel with surface velocity of 30 m/sec. The temperature was monitored by an external pyrometer from the upper surface of the molten alloy through a quartz window. The metal alloys were ejected at a temperature of about 150-250 K above the melting point of the alloy. The resulting ribbon samples had thickness of about 20-25 μm and width of ~ 6 mm. Processing parameters such as the thermal conductivity of the rotating quench wheel, wheel speed, ejection pressure, thermal history of the melt before ejection, distance between nozzle of quartz tube and rotating wheel, as well as processing atmosphere have influenced on the microstructure and properties of melt-spun ribbons [4.3-4.7].

Therefore, all the above mentioned parameters were very precisely controlled. There were numerous studies concerned with the effect of processing parameters on the microstructure and properties of amorphous ribbon [4.8]. While these studies give direction to the control of the microstructure of melt-spun ribbon, the effect of atmosphere on the microstructure during melt spinning was studied [4.9]. It has been established that helium atmosphere enhances the quench-ability of the ribbon over argon and vacuum. But in spite of that considering the cost effectiveness of the production argon atmosphere is very frequently used. The lower pressure of 250 mbar as mentioned above stabilizes the turbulence between melt pull and rotating copper wheel enhancing the heat transfer resulting in a more uniform quenching. As a result a more uniform ribbon microstructure can be obtained at relatively low wheel speed. With increasing wheel speeds for a given ejection rate, the increasing extraction rate results in thinner ribbons.

4.1.3 Thermal Treatment of the Amorphous Ribbons

In order to study nanocrystallization behavior by X-ray diffraction and magnetic properties upon evolution of nanocrystalline phase on amorphous matrix thermal treatment i.e. annealing is required to perform. For X-ray diffraction, as prepared amorphous ribbons were cut into small pieces of about 2 cm length and for magnetic measurement such as permeability toroidal core were wound for annealing treatment. A microprocessor controlled tubular furnace was used for the annealing treatment. A laboratory built vacuum system made by quartz tube capable of evaluating up to 10^{-5} torr was used for this purpose. The samples were put into the quartz tube and evacuated (10^{-5} torr) before it had been put inside the tubular furnace heated to a preset temperature and kept for the time required to complete the annealing. In this way all the isothermal annealing as a function of time were performed.

4.2 Differential Scanning Calorimetry

Differential scanning calorimetry (DSC) is a technique in which the difference in the amount of heat required to increase the temperature of a sample and reference are measured as a function of temperature. In the present study Perkin Elmer, DSC7 was used, which had a temperature scanning range from room temperature to $\sim 900^{\circ}\text{C}$. DSC measurement was used to identify the phase transformation such as glass transition and crystallization. The sample was put in a Pt pan and placed on a Pt holder. An empty pan was placed in the other Pt holder for a reference. The sample pans were designed to have a very high thermal conductivity. In the present investigation the amount of each sample was 10 mg. Fig. 4.3 shows a schematic diagram of a DSC system.

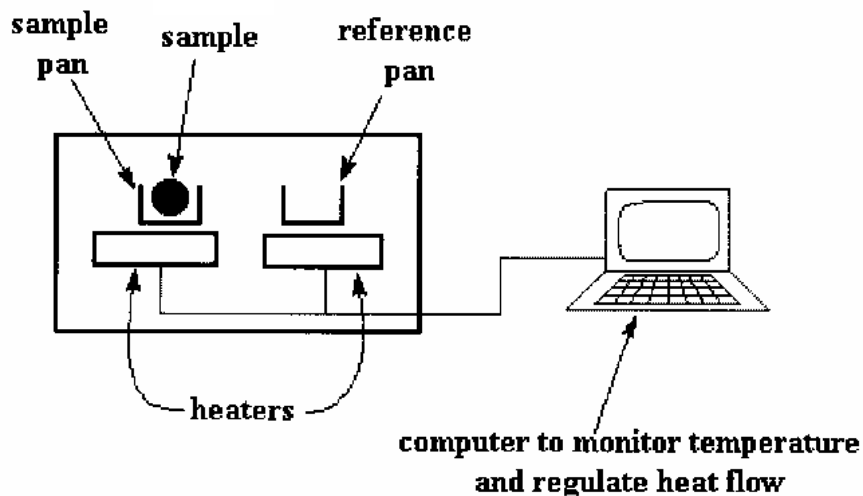


Fig.4.3 Schematic diagram of differential scanning calorimetry (DSC).

The instrument cells are often airtight to shield the sample and reference from external thermal perturbations. This also allows experiments to be performed under variable pressures and atmospheres. The whole system was purged with high purity Ar gas to minimize sample oxidation. The heating rates for non-isothermal scans were 10 to 50K/min with a step of 10K. The temperature and enthalpy were calibrated using pure In and Zn standards. In isothermal mode, the temperature of the reference and the sample was raised to the pre-setting temperature and kept isothermally. In our experiment non-isothermal DSC were used to study the phase transformation kinetics. Whether more or less heat must flow to the sample depends on whether the process is exothermic or endothermic. For example, as a solid sample melts to a liquid it will require more heat flowing to the sample to increase its temperature at the same rate as the reference. This is due to the absorption of heat by the sample as it undergoes the endothermic phase transition from solid to liquid. By observing the difference in heat flow between the sample and reference, differential scanning calorimeters are able to measure the amount of heat absorbed or released during such transitions. DSC may also be used to observe more subtle phase changes, such as glass transitions. DSC is widely used in industrial settings as a quality control instrument due to its applicability in evaluating sample purity and for studying polymer curing.



Fig. 4.4 Differential Scanning Calorimeter (TA Instruments Q100).

A typical differential scanning calorimeter consists of two sealed pans: a sample pan and a reference pan which is generally an empty sample pan. These pans are often covered by or composed of aluminum, which acts as a radiation shield. The two pans are heated, or cooled, uniformly while the heat flow difference between the two is monitored. This can be done at a constant temperature, but is more commonly done by changing the temperature at a constant rate, a mode of operation also called temperature scanning. Fig. 4.4 shows a pictorial view of a DSC setup of Thermal Analysis, U.S.A., model Q100.

During the determination, the instrument detects differences in the heat flow between the sample and reference. This information is sent to an output device, most often a computer, resulting in a plot of the differential heat flow between the reference and sample cell as a function of temperature. When there are no thermodynamic physical or chemical processes occurring, the heat flow difference between the sample and reference varies only slightly with temperature, and shows up as a flat, or very shallow base line on the plot. However, an exothermic or endothermic process within the sample

results in a significant deviation in the difference between the two heat flows. The result is a peak in the DSC curve. Generally, the differential heat flow is calculated by subtracting the sample heat flow from the reference heat flow. When following this convention, exothermic processes will show up as positive peaks above the baseline while peaks resulting from endothermic processes are negative below the baseline.

The result of a DSC experiment is a heating or cooling curve. This curve can be used to calculate enthalpies of transitions. This is done by integrating the peak corresponding to a given transition. It can be shown that the enthalpy of transition can be expressed using the following equation:

$$\Delta H = KA \quad (4.1)$$

where ΔH is the enthalpy of transition, K is the calorimetric constant, and A is the area under the curve. The calorimetric constant will vary instrument to instrument, and can be determined by analyzing a well-characterized sample with known enthalpies of transition[4.10]. An arbitrary DSC thermogram is displayed in fig. 4.5 showing various transformations.

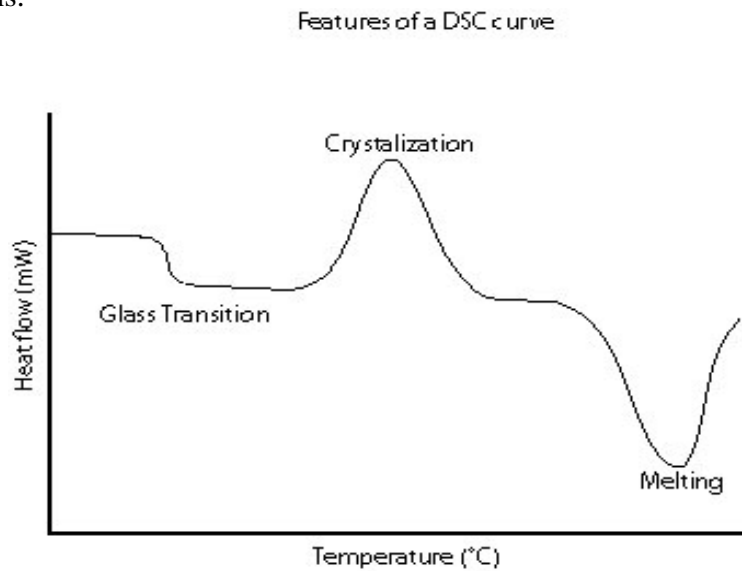


Fig. 4.5 Heat flow as function of temperature of DSC Curve

As the temperature increases, an amorphous solid will become less viscous. At some point the molecules may obtain enough freedom of motion to spontaneously arrange themselves into a crystalline form. This is known as the crystallization temperature (T_c). This transition from amorphous solid to crystalline solid is an exothermic process, and results in a peak in the DSC signal. As the temperature increases the sample eventually reaches its melting temperature (T_m). The melting process results in an endothermic peak in the DSC curve. The ability to determine transition temperatures and enthalpies makes DSC an invaluable tool in producing phase diagrams for various chemical systems [4.11].

4.3 X-ray Diffraction

4.3.1 Introduction

The German Physicist Wilhelm Roentgen discovered X-rays in 1885. X-rays are electromagnetic waves of short wavelengths in the range of 10^{-2} to 10^2 Å. Unlike ordinary light, these rays are invisible, but they travel in straight lines and affect photographic film in the same way as light. On the other hand, they were much more penetrating than light and could easily pass through the human body, wood, quite thick pieces of metal and other “opaque” objects.

4.3.2 Electromagnetic Radiation

X-rays are electromagnetic radiation of exactly the same nature as light but of very much shorter wavelength. The unit of measurement of wavelength in the X-ray region is the Angstrom (Å), equal to 10^{-10} m and X-ray used in diffraction have wavelengths lying approximately in the range 0.5 to 2.5 Å, whereas the wavelength of visible light is of the order of 6000 Å.

X-ray therefore occupies the region between gamma and ultraviolet rays in the complete electromagnetic spectrum as shown in fig: 4.6.

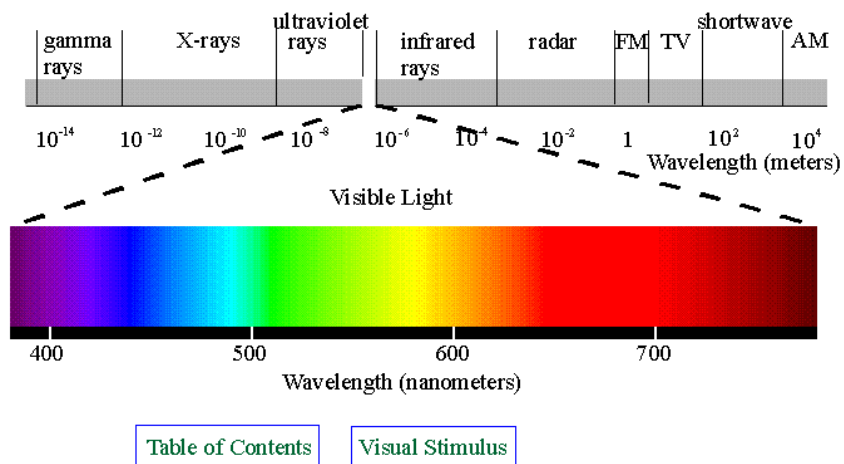


Fig. 4.6 Electromagnetic spectrum.

The approved SI unit for wavelength in the X-ray region is nanometer:
 1 nanometer = 10^{-9} m = 10 Å.

4.3.3 Production of X-ray

We have seen that X-rays are produced whenever high-speed electrons collide with a metal target. Any X-ray tube must therefore contain (i) a source of electrons, (ii) a high accelerating voltage and (iii) a metal target. Furthermore since most of the kinetic energy of the electron is converted into heat, the latter is almost always water-cooled to prevent its melting.

All X-ray tubes contain two electrodes, an anode (the metal target) maintained, few exceptions, at ground potential, on a cathode maintained at a high negative potential, normally of the order of 30000 to 50000 volt for diffraction work. X-ray tubes may be divided into two basic types, according to the way in which sections are produced by

the ionization of small quantity of gas (residual) air in a partly evacuated tube and filament tubes, in which the source of the electrons is a hot filament.

4.3.4 X-ray Diffractometer

Thin sheets of the samples were prepared from the alloy ingot by rolling the ingot. Sharp strip like samples were cut from the thin sheet for Debye-Scherrer experiment.

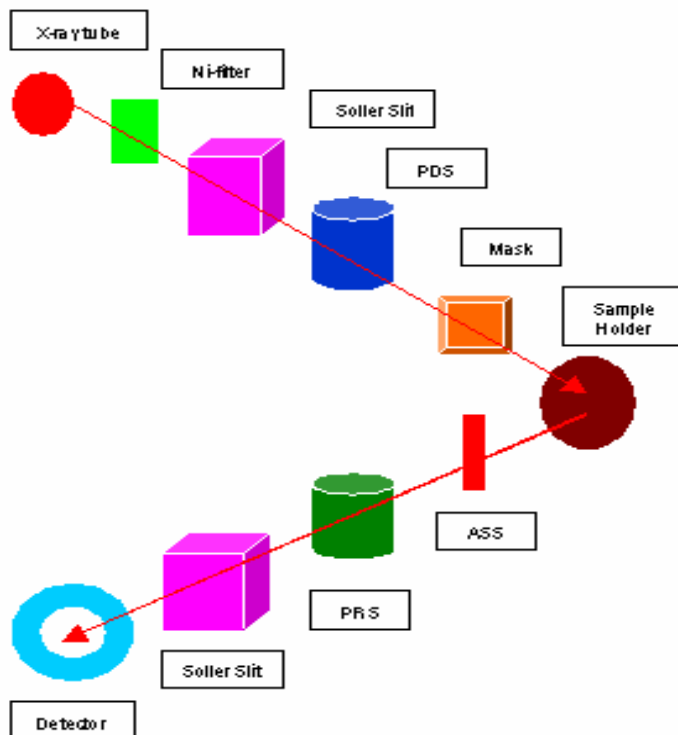


Fig. 4.7 Block diagram of the PHILIPS PW 3040 X'Pert PRO XRD system.

After heat treatment of the samples separately to remove strain the lattice parameter of the quenched specimen in the disordered state were measured by Debye-Scherrer method using Cu radiation. In the present case a special technique was used to

determine the lattice parameter using Debye-Scherrer method. The shape of the sample was used as the same of Debye-Scherrer method sample. But in the conventional Debye-Scherrer experiment, sharp strip sample rotates and X-ray tube and camera remain fixed. In the present case, sample was kept fixed and X-ray tube and detector were moved to the θ and 2θ ranges respectively. Instead of the film, digital data was recovered for the whole 2θ range.

After the pattern is obtained the value of 2θ is calculated for each diffraction line; set of 2θ values is the raw data for the determination of the lattice parameters of the unit cell. Fig. 4.7 shows the block diagram of Phillips PW3040 X'Pert PRO X-ray diffractometer.

A PHILIPS PW 3040 X'Pert PRO X-ray diffractometer was used for the lattice parameter determination in the Materials Science Division, Atomic Energy Center, Dhaka. Fig. 4.8 shows the inside view of the X'Pert PRO XRD system.



Fig.4.8 A PHILIPS PW3040 X'Pert PRO X-ray diffractometer.

The X'Pert PRO XRD system contains the following parts:

- (i). "Cu-Tube" with maximum, input power of 60 kV and 55 mA
- (ii). "Ni-Filter" to remove the CuK_α component.
- (iii). "Programmable Divergent Slit" (PDS) to reduce divergence of beam and control irradiated beam area.
- (iv). "Mask" to get desired beam area.
- (v). "Sample holder" for powder sample.
- (vi). "Anti Scatter Slit" (ASS) to reduce air scattering background.
- (vii). "Programmable Receiving slit" (PRS) to control the diffracted beam intensity.
- (viii). "Soller Slit" to stop scattered beam and pass parallel diffracted beam.

A PHILIPS PW3040 X'pert PRO X-ray diffractometer was used to study the crystalline phases of the prepared samples in the Materials Science division, Atomic Energy Centre, Dhaka. The powder diffraction technique was used with a primary beam power

of 40 kV and 30 mA for Cu radiation. A nickel filter was used to reduce CuK_β radiation and finally Cu-K_α radiation was only used as the primary beam. A 2θ scan was taken from 30° to 90° to get possible fundamental peaks with the sampling pitch of 0.02° and time for each step data collection was 1.0 sec. After that data of the samples were analyzed by computer software.

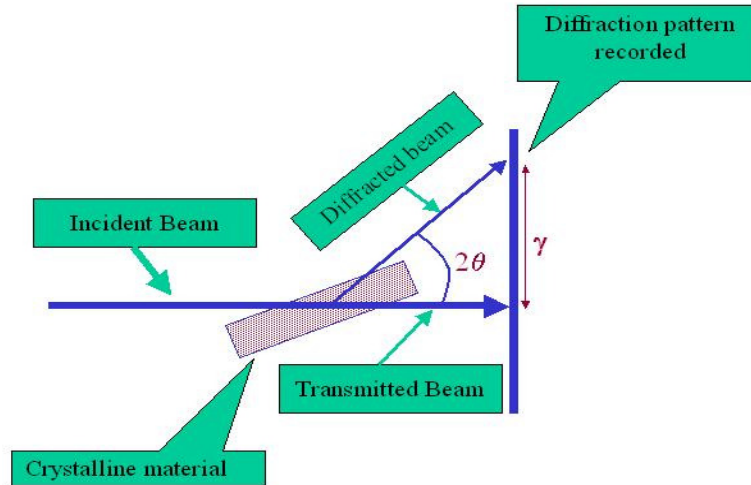


Fig.4.9 Schematic diagram of X-ray.

The aim of the present study was to determine the grain size of $\text{Fe}_{73.5-x}\text{Cr}_x\text{Cu}_1\text{Nb}_3\text{Si}_{13.5}\text{B}_9$ ($x = 0,1,2,3,4,5,6,7,8,9,10,12.5,15\&17.5$) alloys. The grain size of the prepared samples were determined from the strongest peak of each XRD patterns using Scherrer's formula,

$$D_g = \frac{0.9\lambda}{\beta \cos \theta} \quad (4.2)$$

where, D_g is the average grain size, λ is the wavelength of the radiation used as the primary beam of Cu-K_α ($\lambda = 1.54178 \text{ \AA}$), θ is the angle of incidence in degree and β is the full width at half maximum (FWHM) of the strongest reflection (110) in radian, which was determined experimentally after correction of instrumental broadening (in the present case it is 0.07°).

The peaks in an X-ray diffraction pattern are directly related to the atomic distance. Let us consider an incident X-ray beam interacting with the atoms arranged in a periodic

manner as shown in fig. 4.10. The atoms represented as block spheres in the figure, can be viewed as forming different sets of planes in the crystal.

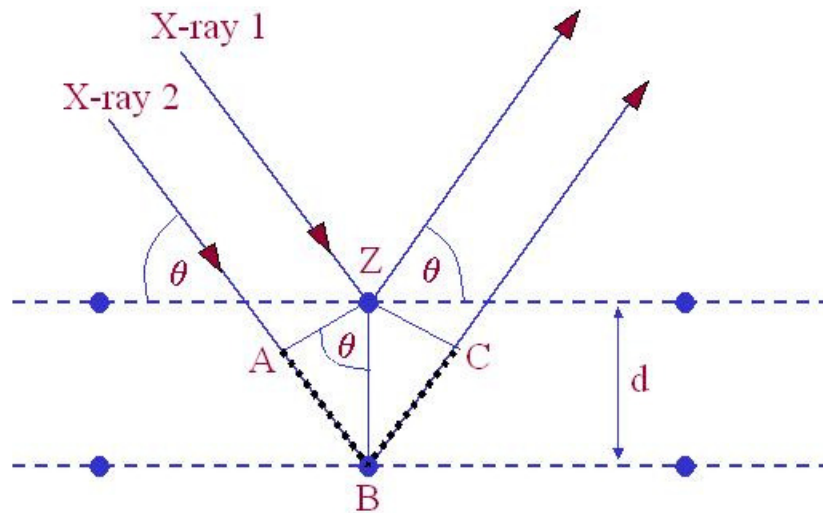


Fig. 4.10 Bragg's diffraction pattern.

For a given set of lattice plane with an inter planer distance of d , the condition for a diffraction to occur can simply written as

$$2d_{hkl} \sin\theta = n\lambda \quad (4.3)$$

which is known as Bragg's law. Where, λ is the wavelength of the X-ray, θ is the scattering angle and n is an integer representing the order of the diffraction.

4.3.5 Determination of Nanometric Grain Size by X-ray Diffraction

Nanocrystalline alloys are above all crystalline and because of their crystallinity exhibit Bragg scattering peaks in X-ray diffraction experiments. However, due to their small size, significant fine particle broadening is observed in the Bragg peaks. The condition for constructive interference, reinforcement of X-ray scattering from a crystalline solid is given by Bragg's law:

$$n\lambda = 2d \sin\theta \quad (4.4)$$

This equates the path difference of X-rays scattered from parallel crystalline planes spaced $d = d_{hkl}$ apart to an integral (n) number of X-ray wavelengths λ . Here θ is the X-ray angle of incidence (and of diffraction) measured with respect to the crystalline planes. For an infinite crystal Bragg scattering occurs at discrete values of 2θ satisfying the Bragg condition, i.e. Bragg peaks are δ -functions. For finite sized crystals the peaks are broadened over a range of angles as shown in fig. 4.11

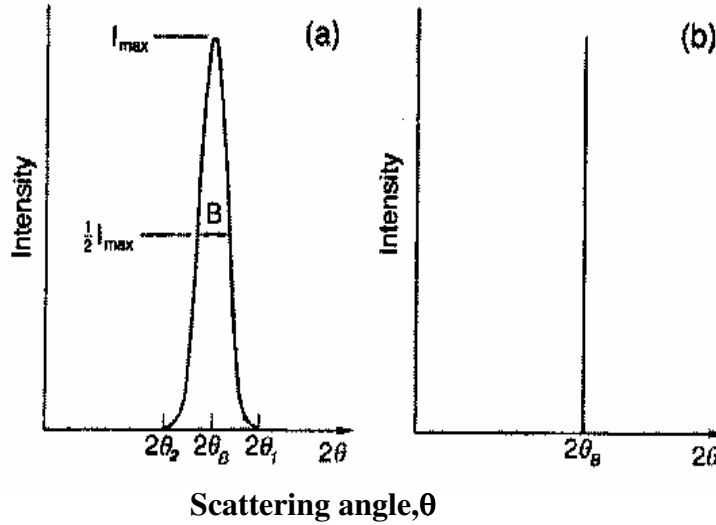


Fig. 4.11 Effect of fine particle size on diffraction curves (schematic)

To better understand the phenomenon of fine particle broadening following argument of Cullity, [13] we consider a finite crystal of thickness, $D = md$, where m is an integer, and d is the distance between crystalline planes, i.e., there are m planes in D . Considering Fig.-3.3, if the broadened Bragg peak begins at an angle $2\theta_2$ and ends at $2\theta_1$, the breadth of the peak or full width at half maximum is given as:

$$\beta = \frac{1}{2}(2\theta_1 - 2\theta_2) = \theta_1 - \theta_2 \quad (4.5)$$

Now consider the path differences for each of the two angles θ_1 and θ_2 , for X-rays traveling the full thickness of the crystal. The width β is usually measured in radians.

We now write path difference equations for these two angles, related to the entire thickness of the crystal rather to the distance between adjacent planes.

$$2D \sin \theta_1 = (m+1)\lambda \quad (4.6)$$

$$2D \sin \theta_2 = (m-1)\lambda \quad (4.7)$$

By subtraction we find:

$$D (\sin \theta_1 - \sin \theta_2) = \lambda \quad (4.8)$$

$$D 2 \cos\left(\frac{\theta_1 + \theta_2}{2}\right) \sin\left(\frac{\theta_1 - \theta_2}{2}\right) = \lambda \quad (4.9)$$

But θ_1 and θ_2 are both very nearly equal to θ , so that $\theta_1 + \theta_2 \approx 2\theta$ and $\sin\left(\frac{\theta_1 - \theta_2}{2}\right) \approx \left(\frac{\theta_1 - \theta_2}{2}\right)$ so that equation (4.9) can be written as:

$$2D \cos \theta \left(\frac{\theta_1 - \theta_2}{2}\right) = \lambda \quad (4.10)$$

From equation (4.5) and equation (4.10) we get:

$$\beta D \cos \theta = \lambda \quad (4.11)$$

$$D = \frac{\lambda}{\beta \cos \theta} \quad (4.12)$$

A more exact empirical treatment yields:

$$D = \frac{0.9\lambda}{\beta \cos \theta} \quad (4.13)$$

which is known as the Scherrer's formula. It is used to estimate the particle size of very small crystals from the measured width of their diffraction curves.

4.4 Magnetization Measurement Techniques

There are various means of measuring magnetization of a substance. The magnetization of a substance is usually determined by measuring its magnetic moment divided by the volume or mass of the substance. In the present study magnetization has been performed using a Vibrating Sample Magnetometer (VSM) and a Superconducting Quantum Interface Device (SQUID) magnetometer

4.4.1 Vibrating Sample Magnetometer (VSM)

Vibrating Sample Magnetometer developed by S. Foner [4.14, 4.15] is a versatile and sensitive method of measuring magnetic properties and is based on the flux change in a coil when the sample is vibrated near it. The Vibrating Sample Magnetometer (VSM) is an instrument designed to continuously measure the magnetic properties of materials as a function of temperature and field. In this type of magnetometer, the sample is vibrated up and down in a region surrounded by several pickup coils. The magnetic sample is thus acting as a time-changing magnetic flux, varying inside a particular region of fixed area. From Maxwell's law it is known that a time varying magnetic flux is accompanied by an electric field and the field induces a voltage in pickup coils. This alternating voltage signal is processed by a control unit system, in order to increase the signal to noise ratio. The result is a measure of the magnetization of the sample. Schematic diagram of the vibrating sample magnetometer is shown in fig. 4.12.

In the present thesis work we used two different VSMS' at two different institutes for the measurements. One of them is digital measurement system (DMS 880 VSM, USA) situated at the center for materials science (CMS), National University of Hanoi, Vietnam. It is a computer controlled commercial type VSM and capable to take program measurement. The field can be varied 0 and 13 KOe with a field resolution of 10^{-2} Oe. Field can be controlled in stepped mode, which gives better accuracy of field measurement. For a high temperature measurement the sample is put inside an oven made of quartz glass and the temperature is controlled with the precision controller, in

which the temperature can be increased with different heating rates according to the desired rate. Isothermal magnetization measurement as a function of field can also be performed by this VSM. Another laboratory built sensitive VSM installed at the Institute of Materials Science, Vietnamese Academy of Science and Technology; Hanoi has also been used to measure the magnetization of the samples as a function of field and temperature. In these VSM the maximum field used in our experiment is 10KOe. Where the temperature was varied from room temperature to 1000 K. In this VSM temperature scan was continuous in which the magnetization data were recorded after a regular interval of time. Therefore an enormous number of data were recorded which gives more precision measurement for an accurate determination of phase transition temperature as well as the onset of crystallization temperature. Above room temperature and high temperature oven with a PID temperature controller was used. Thermocouple placed adjacent to the sample and continuous flow of helium exchange gas was maintained. The sensitivity of the both VSM used in the present investigation is $\approx 10^{-5}$ emu and all of them have the same working principle with slight deviation in their constructions. The applied magnetic field can be varied between 0 and 13 KOe.

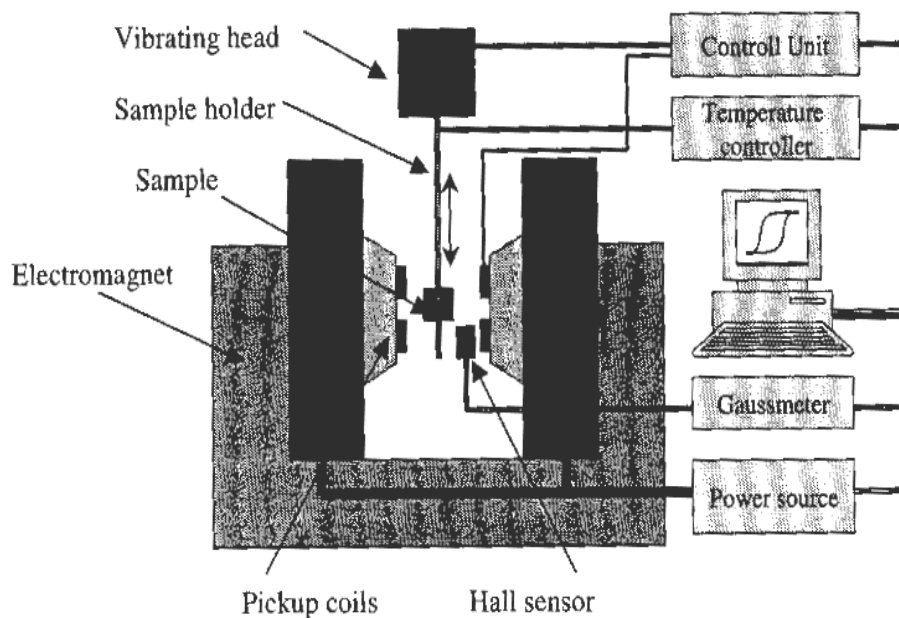


Fig.4.12 Vibrating Sample Magnetometer (VSM)

4.4.2 SQUID magnetometer

In the present work a Superconducting Quantum Interface Device (SQUID) magnetometer MPMS XL, USA was used for a detail study of the magnetic properties at the Department of Engineering Sciences, Angstrom Laboratory, Uppsala University, Sweden. The magnetic properties measurement system MPMS XL is a sophisticated analytical instrument configured specially for the study of the magnetic properties of small samples over a broad range of temperature from 4.2 K to 400 K and magnetic fields from -50 KOe to $+50$ KOe. This standard system made by Quantum Design Inc. USA can measure the magnetic moment of solid powder and liquid samples with a differential sensitivity of 10^{-9} emu and can handle a maximum signal size of 0.5 emu. A general view of the MPMS XL with its system components is shown in fig. 5.13. The most sensitive available device for measuring magnetic fields, based on this sensitive device the so-called ‘SQUID magnetometers’ have been developed. SQUID magnetometers are used to characterize materials when the highest detection sensitivity over a broad temperature range and using applied magnetic fields up to several Tesla is needed. Nowadays, this instrument is widely used worldwide in research laboratories. The system is designed to measure the magnetic moment of a sample, from which the magnetization and magnetic susceptibility can be obtained. Therefore, SQUID magnetometers are versatile instruments that perform both, DC and AC magnetic moment measurement.



Fig. 4.13 SQUID Magnetometer.

The major components of a SQUID magnetometer are: superconducting magnet, superconducting detection coil, a SQUID connected to the detection coil, superconducting magnetic shield. Superconducting magnets are solenoid made of superconducting wire which must be kept at liquid helium dewar. The uniform magnetic field is produced along the axial cylindrical bore of the coil. The superconducting pick-up coil system, which is configured as a second order gradiometer is placed in the uniform magnetic field region of the solenoidal superconducting magnet. The SQUID device is usually a thin film that functions as an extremely sensitive current to voltage converter. Measurements are done in this equipment by moving the samples through the second order gradiometer. Hence, the magnetic moment of the sample induces an electric current in the pick-up coil system. Superconducting magnetic shield is used to shield the SQUID sensor from the fluctuations of the ambient magnetic field of the place where the magnetometer is located and from the large magnetic field produced by the superconducting magnet.

Using this kind of equipment we can measure the real and imaginary components of AC magnetic susceptibility as a function of frequency, temperature, AC magnetic field amplitude and DC magnetic field, and time. Using a specially designed sample holder the magnetic moment as a function of angle can also be measured.

It is an important feature of the instrument that one can change the magnetic field either by “oscillate mode” or “no overshoot mode”. The oscillate mode is used to minimize the remanent field of the magnet, whenever an accurate value of magnetic field is needed, e.g. in case of zero field cooling. In the hysteresis measurement the no overshoot mode has been selected, in which the field is changed directly from one value to another, and the magnet is returned to its persistent mode.

The MPMS XL features the new reciprocating sample measurement system. Unlike DC measurements where the sample is moved through the coils in discrete steps the RSO measurements are performed using a servomotor, which rapidly oscillates the sample is shown in fig. 4.14.

A shaft encoder on the servomotor records the position of the sample synchronous with the SQUID signal. The data received is fitted to an ideal dipole moment response. To ensure this assumption is applicable samples need to be small: the calibration sample is a cylinder of 3 mm diameter and 3mm height. Sample of this size or smaller than an ideal point dipole to an accuracy of approximately 0.1%.

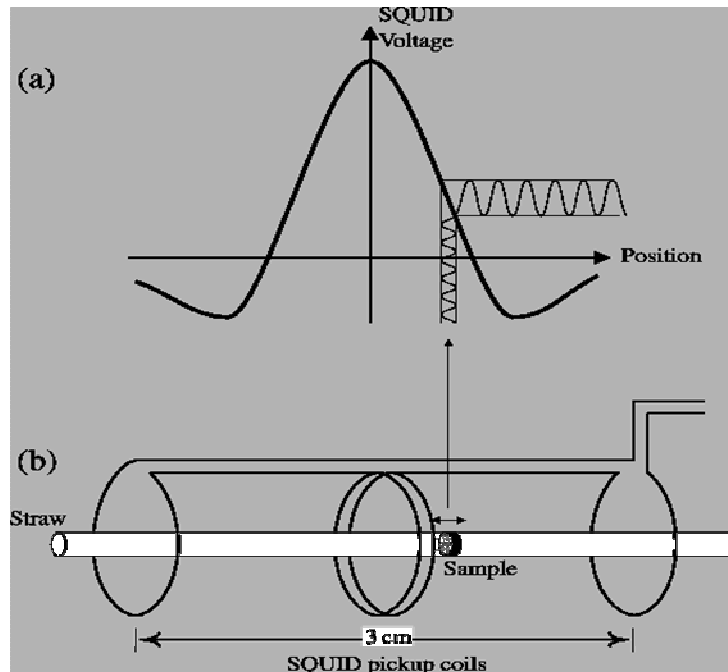


Figure 4.14: Illustration of an RSO measurement with small amplitude. (a) the ideal SQUID response for a dipole and (b) the movement of the sample within the SQUID pickup coils.

RSO measurements can be made in one of two configurations: Centre or maximum slope. Centre scans use large oscillations (2 or 3 cm) around the centre point of the pickup coils. These scans take a long time but the sample always remains properly located and a large number of measurements are recorded. These give the most accurate readings.

The maximum slope method oscillates the sample over a small region (0.2cm) at the most linear part of the SQUID response. The smaller amplitude makes measurements quicker and prevents the sample being subjected to significant magnetic field variation; however it also makes the measurement less accurate and susceptible to drift in the sample position.

The MPMS XL features significant improvements in the temperature control system. Utilizing a new design for the helium flow impedance, the MPMS XL has capability to

operate continuously at temperatures below 4.2 K for indefinite periods of time-completely removing time limitations for making measurements in this temperature regime.

The new MPMS XL eliminates the operations associated with filling and recycling the He reservoir. Thus, the system solves the traditional problems of temperature instability and hysteresis associated with rapid boil off of liquid helium when warming through 4.2K. The results are smooth monotonic transitions across 4.2 K during both warming and cooling temperature sweeps. All these capabilities are fully automated for precise systems control and user-friendly operation.

The addition to a redesigned impedance system, the MPMS XL uses a new thermometer design for improved temperature accuracy and precise thermal control. The new thermometry, designed and developed at Quantum Design, is installed in close proximity to the sample within the sensitive coil detection region. The improved design is combined with new temperature control capabilities to provide more accurate measurements of the sample chamber, even under extreme temperature changes.

The new temperature sweep mode of operation provides MPMS XL users with the ability to take magnetic measurements while sweeping the system temperature at a controlled rate, automatically with no manual intervention. This mode provides a controlled, monotonic change in temperature during a measurement sequence at rates up to 10 K/min. Measurements of temperature dependence over large temperature ranges, which previously required time consuming temperature stabilization, can now be made quickly and precisely using temperature sweep mode.

4.5 Components of Complex Permeability Measurements

Determinations of permeability normally involve the measurements of the change in self-inductance of a coil in the presence of magnetic core. Methods of measurement those are commonly used are:

- (i) The LCR bridge method
- (ii) Resonance circuits and
- (iii) The standing wave method

In this thesis work complex permeability was measured by the LCR bridge method. The behavior of a self-inductance can now be described as follows. If we have an ideal lossless air coil of inductance L_0 , on insertion of magnetic core with permeability μ , the inductance became μL_0 . The complex impedance Z of this coil can then be expressed as

$$\begin{aligned}
 Z &= R + iX = i\omega L_0 \mu \\
 &= i\omega L_0 (\mu' - i\mu''), \\
 &= \omega L_0 \mu'' + i\omega L_0 \mu'
 \end{aligned} \tag{4.14}$$

where the resistive part

$$R = \omega L_0 \mu'' \tag{4.15}$$

and the reactive part is

$$X = \omega L_0 \mu' \tag{4.16}$$

The r.f permeability can be calculated from the complex impedance of a coil using eqⁿ (4.14). The core is made in the form of toroid to avoid demagnetizing effects.

The real (μ') and imaginary (μ'') part of the complex permeability of the as-cast and annealed ribbons were measured as a function of frequency and temperature using Wayne Kerr 3255 B inductance meter and HP 4192 A impedance analyzer in conjunction with a laboratory built tubular furnace with continuous heating rate of $\approx 5^\circ\text{C}/\text{min}$ with a very low ac driving field of $\approx 10^{-3}$ Oe. From the temperature dependence of permeability measurement, Curie temperature, T_c of the amorphous ribbons was determined. From the frequency dependence of complex permeability, evolution of permeability and magnetic loss component at different stages of nanocrystallization as affected by thermal treatment at different temperatures was

determined using toroids prepared from the ribbons wound with insulating Cu wire. The Wayne Kerr 3255 B inductance and HP 4192 A impedance analyzer directly measure the value of inductance, L and loss factor,

$$D = \tan \delta \quad (4.17)$$

From inductance the value of real part of complex permeability, μ' can be obtained by using the relation,

$$\mu' = \frac{L}{L_0} \quad (4.18)$$

Here, L is the inductance of the toroid and L_0 is the inductance of the coil in the free space. L_0 is determined by using the relation

$$L_0 = \frac{\mu_0 N^2 S}{\pi d} \quad (4.19)$$

where $S = \frac{m}{\pi \rho d}$, μ_0 is the permeability of the vacuum, m is mass of the sample, N is the number of turns, S is the cross-sectional area of the toroid, d is the average diameter and ρ is the density of the material. The imaginary part of complex initial permeability can be determined by using the relation,

$$\tan \delta = \frac{\mu''}{\mu'} \quad (4.20)$$

and the relative loss factor is calculated with the relation $\frac{\tan \delta}{\mu'}$.

The frequency characteristics of the amorphous ribbon samples i.e the permeability spectra, were investigated using an impedance analyzer (LCR bridge), Wayne Kerr 3255B model, at Materials Science Division, Atomic energy Centre, Dhaka. The measurements of inductances were taken in the frequency range 1 kHz to 500 kHz. The values of measured parameters are obtained as a function of frequency and the real and imaginary parts of permeability and the loss factor μ' was calculated by using above formulas.

4.6 Preparation of the samples for complex permeability measurement

The amorphous ribbons were wound into toroidal shape having outer and inner diameters 13 to 15 mm and with the ratio of outer and inner diameters always kept less than 1.2 in order to improve the homogeneity of the applied field, as also to reduce the possibility of an inhomogeneous inductance response. Toroids were wound with 10 turns around to apply AC magnetic fields over a wide range of amplitude. While measuring the permeability of the amorphous ribbon cores at high frequency, the high electric resistance of these materials generally precludes the trouble some skin effect found in ribbons. However, the cross section of the amorphous ribbon core to be measured may have to be kept small in order to avoid dimensional resonance phenomena. To avoid an increase in resistance owing to skin effect, braided copper wire is used at frequencies higher than 100 KHz. At higher frequencies the capacitance arising from winding gives inaccurate values of R and L. It is therefore necessary, to keep the capacitance of the winding as low as possible. Frequency response characteristics were then investigated on these ring shaped specimens as a function of frequency.

Results and Discussion

5.1 Crystallization behavior of $\text{Fe}_{73.5-x}\text{Cr}_x\text{Cu}_1\text{Nb}_3\text{Si}_{13.5}\text{B}_9$ alloys

5.1.1 Study of Crystallization Behavior of Amorphous $\text{Fe}_{73.5-x}\text{Cr}_x\text{Cu}_1\text{Nb}_3\text{Si}_{13.5}\text{B}_9$ Alloys

The understanding of the crystallization kinetics of magnetic amorphous/nanocrystalline alloys has enormous scientific and technological interest because of the enhancement as well as deterioration of magnetic properties extremely depends on the degree of crystallization. Crystallization kinetics is often determined from Differential Scanning Calorimetry (DSC), Differential Thermal Analysis (DTA) and in magnetic materials from thermomagnetic analysis (TMA) [5.1-5.3]. Crystallization kinetics have also been studied by a variety of techniques including high resolution transmission electron microscope (HRTEM), in-situ XRD, extended X-ray absorption fine structure (EXAFS) measurements and resistance measurements.

Differential Scanning Calorimetry (DSC) is an important experimental tool to study the crystallization kinetics of amorphous materials through which the onset of crystallization, the temperature of primary and secondary crystallization phenomena can be revealed. Fig.5.1 (a) and fig.5.1 (b) displays the DSC thermogram measured with a heating rate of $20^{\circ}\text{C}/\text{min}$, where the primary crystallization and secondary crystallization peak temperatures are well demonstrated for the entire series of $\text{Fe}_{73.5-x}\text{Cr}_x\text{Cu}_1\text{Nb}_3\text{Si}_{13.5}\text{B}_9$ ($x = 0, 1, 2, 3, 4, 5, 6, 7, 8, 9, 10, 12.5, 15$ & 17.5) amorphous alloys in the form of ribbons, prepared by melt spinning technique. Two well-defined exothermic peaks corresponding to two different crystallization products are manifested. Unfortunately the identification and composition of the phases cannot be ascertained through the DSC measurement.

X-ray diffraction technique confirmed these two phases as bcc-Fe(Si) corresponding to the first peak while Fe-B to the second peak on the amorphous matrix. This has been proved by several earlier studies by XRD [5.4-5.8]. It is observed from fig.5.1 (a) and

fig.5.1 (b) that the crystallization of each phase has occurred over a wide range of temperatures and the primary crystallization temperature shifts to higher temperature as the Cr concentration is increased. There is a difference of $\approx 150\pm 10^0\text{C}$ for the two crystallization temperatures. But this difference decreases as the Cr content is increased. For $x=17.5$, it is observed from fig.1 (b) that the two crystallization peaks are very close to each other. The secondary crystallization peak temperature for the boride phase is found to increase slightly with lower Cr content, while for higher Cr content alloys it slightly shifts to lower temperature. The results indicate that the Cr has enhanced the thermal stability of the amorphous alloys against crystallization. This is to note that for obtaining good soft magnetic properties, T_{x1} and T_{x2} corresponding to primary and secondary crystallized phases should be well separated from each other at a annealing temperature $T_{x1} < T_a < T_{x2}$ so that only primary crystallization product $\alpha\text{-Fe}(\text{Si})$ is crystallized. The reason is that the secondary crystallization product Fe-B is extremely detrimental for the soft magnetic properties. From our results on the onset of crystallization temperatures T_{x1} and T_{x2} , it is immediately clear that the alloys with higher Cr content are not expected to show good soft magnetic properties.

Fig. 5.2 (a,b,c) demonstrates the heating rate dependence of DSC thermogram (heating rate 10, 20, 30, 40 & $50^0\text{C}/\text{min}$) for some of the representative amorphous alloys with $x = 1, 3 \text{ \& } 5$ respectively. It is observed that the crystallization peak temperature shifts to higher values as the heating rate is increased due to a thermal activation necessary for crystallization, which suggests the dependence of crystallization temperature upon the heating rate. Therefore, from the heating rate dependence of DSC thermogram, activation energy of crystallization has been calculated using the Kissinger relation [5.9] which is expressed as:

$$\ln\left(\frac{B}{T_p^2}\right) = -\frac{E}{k_B T_p} + \text{constant} \quad (5.1)$$

where B is the heating rate, T_p is the crystallization peak temperature, E is the crystallization activation energy and k is the Boltzman constant. By plotting $\ln\left(\frac{B}{T_p^2}\right)$

against $\frac{1}{T_p}$, one can derive the value of E from the slope of the straight line which is depicted in fig. 5.2 (d) for the sample $x = 3$. The determined values of activation energy for the crystallization of primary crystallization product bcc-Fe(Si) and secondary crystallization product Fe-B are $E_1 = 3.18$ and $E_2 = 4.62$ eV respectively. Our results are comparable with the published literature values [5.10, 5.11].

Table-5.1 shows the crystallization onset temperature, peak temperature for the primary and secondary crystallization measured with a heating rate $20^{\circ}\text{C}/\text{min}$ together with their corresponding activation energies of crystallization. It is observed from the table-5.1 that the crystallization onset temperature (T_{x1}) and the peak temperature (T_{p1}) for the primary crystallization increase continuously with the increase of Cr substitution for Fe in the $\text{Fe}_{73.5-x}\text{Cr}_x\text{Cu}_1\text{Nb}_3\text{Si}_{13.5}\text{B}_9$ alloys. Similar is the situation with the secondary crystallization temperature T_{x2} and T_{p2} with the exception that for very high Cr content in which T_{x2} and T_{p2} slightly decreases toward the value corresponding to zero Cr content alloy. The activation energies of crystallization for the α -Fe(Si) and Fe-B phases are found to increase gradually with increase of Cr content in the alloy system with slight deviation of few alloys probably due to experimental uncertainty. Rosales-Rivera *et al.* [5.12] found similar enhancement of T_{x1} and the activation energy with the increase of Cr concentration in their studied $\text{Fe}_{73.5-x}\text{Cr}_x\text{Cu}_1\text{Nb}_3\text{Si}_{13.5}\text{B}_9$ system. Primary crystallization onset temperature (T_{x1}) in our experiment varies from 522°C for Cr = 1 at.% to 580°C for Cr = 15 at.%. This implies that higher Cr content alloys weaken the diffusion process to form the crystallization phases since Cr has a melting temperature (1857°C) higher than that of Fe (1536°C). From our experimental findings it is clearly understood that the partial substitution of Fe by Cr enhances thermal stability of amorphous alloys against crystallization.

The opposite scenario has been observed when the substitution of Co for Fe in the FINEMET $\text{Fe}_{73.5-x}\text{Co}_x\text{Cu}_1\text{Nb}_3\text{Si}_{13.5}\text{B}_9$ alloys is made [5.10]. The crystallization peak temperature (T_{p1}) and the activation energy for the primary crystallization E_1 decreases gradually with Co content. This result indicates that the role of Co is to facilitate the

formation of crystalline α -Fe(Si) phase. This is to note that the onset of crystallization temperature has been taken as the temperature at which the exothermic peak starts rising. The understanding of the crystallization onset, crystallization peak temperature and the end of crystallization temperature is essential for the determination of appropriate annealing temperature for nanocrystallization. Temperature and time of annealing is crucial for controlling the size and volume fraction of nanocrystals, which ultimately controls the magnetic properties of the FINEMET type of amorphous soft magnetic alloys.

Table-5.1 Crystallization states and activation energy of different phases of nanocrystalline amorphous ribbons with composition $\text{Fe}_{73.5-x}\text{Cr}_x\text{Cu}_1\text{Nb}_3\text{Si}_{13.5}\text{B}_9$ alloys

Cr content x at. %	Primary crystallization temperature, T_{x1} in $^{\circ}\text{C}$	Primary peak temperature, T_{p1} in $^{\circ}\text{C}$	Secondary crystallization temperature, T_{x2} in $^{\circ}\text{C}$	Secondary peak temperature, T_{p2} in $^{\circ}\text{C}$	Activation energy of Fe(Si) phase E_{a1} in eV	Activation energy of Fe-B phase E_{a2} in eV
1	522	542	675	690	3.2	3.6
2	526	557	680	702	3.6	4.2
3	552	569	723	732	3.2	4.6
4	541	561	691	710	3.6	3.5
5	555	573	737	744	2.3	4.5
6	574	579	718	712		
8	564	581	696	703		
9	543	566	688	704		
10	535	559	691	710		
12.5	566	575	691	703		
15	614	632	677	693		
17.5	630	656	671	685		

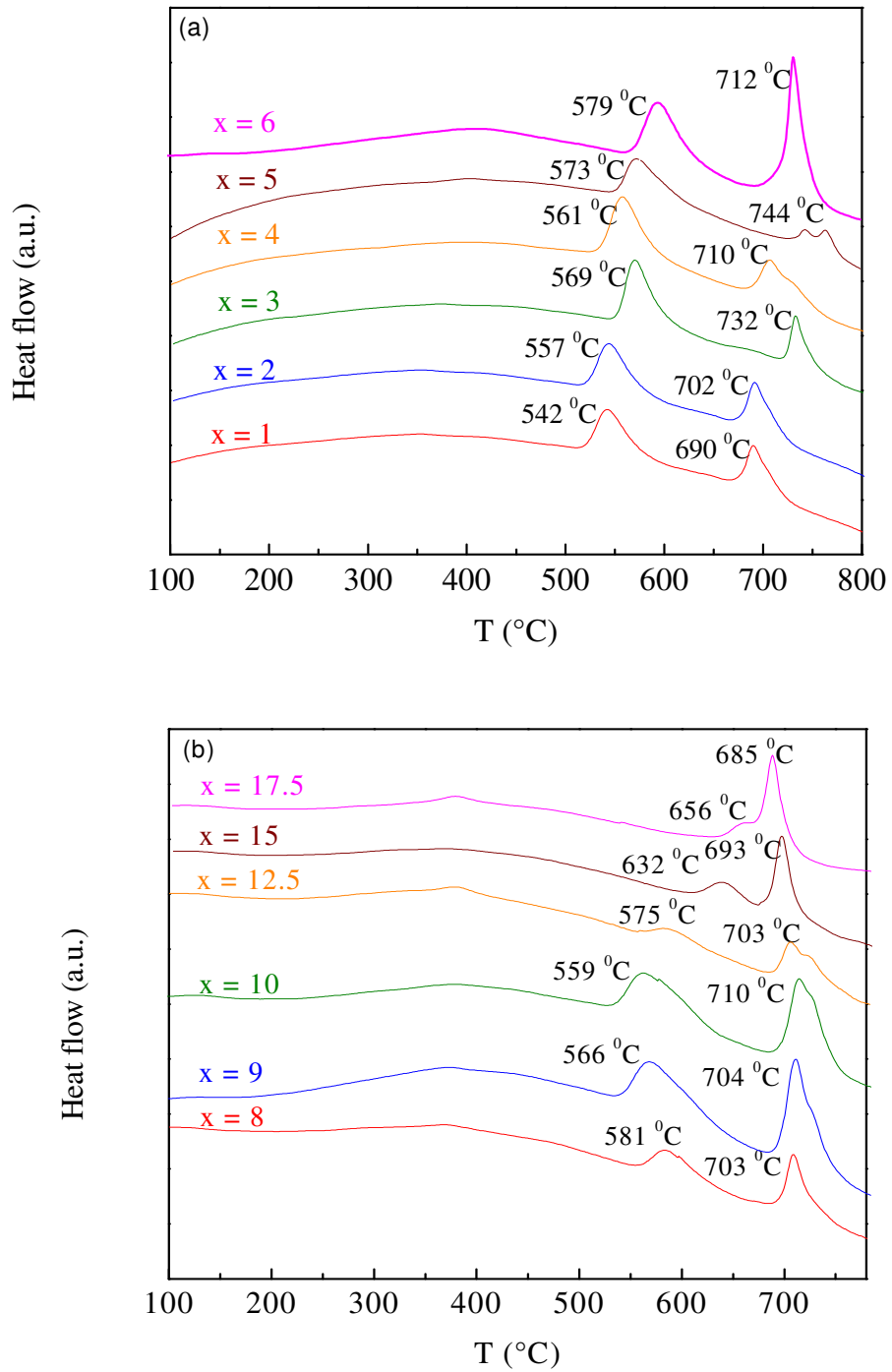


Fig. 5. 1(a). DSC thermograms of amorphous ribbons of $\text{Fe}_{73.5-x}\text{Cr}_x\text{Cu}_1\text{Nb}_3\text{Si}_{13.5}\text{B}_9$ [$x =$ Fig. 1, 2, 3, 4, 5 & 6] (b) $\text{Fe}_{73.5-x}\text{Cr}_x\text{Cu}_1\text{Nb}_3\text{Si}_{13.5}\text{B}_9$ [$x = 8, 9, 10, 12.5, 15$ & 17.5] alloys.

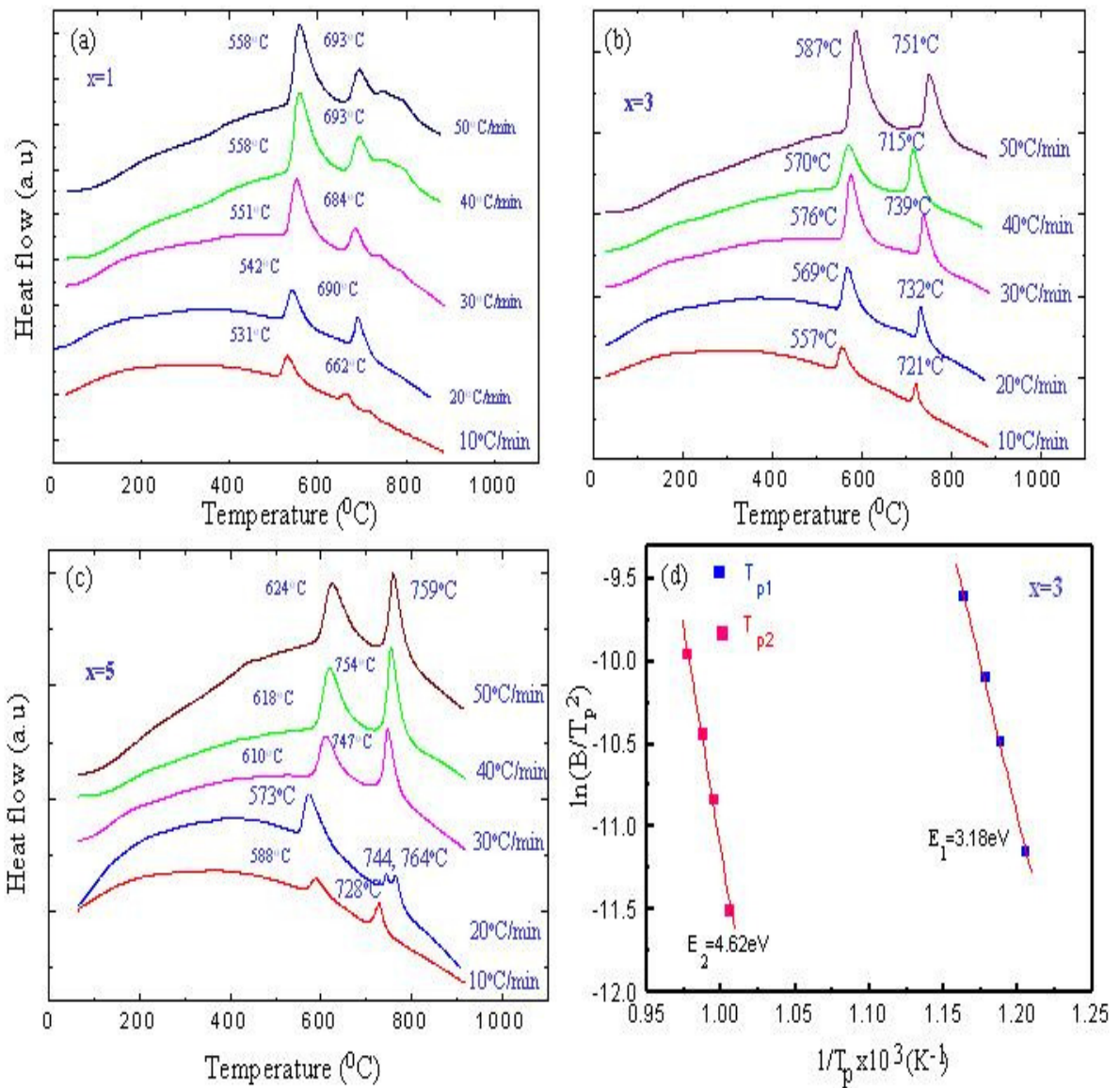


Fig. 5.2 DSC thermograms of amorphous ribbons of Fe_{73.5-x}Cr_xCu₁Nb₃Si_{13.5}B₉ alloys at different heating rates of 10-50°C/min (a) x = 1 (b) x = 3, (c) x = 5 and (d) Kissinger plot for determination of crystallization activation energies of E₁ for Fe(Si.) and E₂ for Fe-B phases

5.1.2 Determination of Crystallization Products and Grain Size

X-ray diffraction is generally used for the identification of various phases while the grain size is estimated by high-resolution transmission electron microscope (HRTEM) and/or by X-ray diffraction. Nanocrystalline alloys are above all crystalline and because of their crystallinity they exhibit Bragg Scattering peaks in X-ray diffraction experiments. However, due to their small size, significant fine particle broadening is observed in the Bragg peaks. For 50 nm particles, a broadening of 0.2° at half width of the peak is expected which can easily be measured. Using Scherrer's formula of line broadening, particle size between 5 and 60 nm can be measured using XRD.

In the present study X-ray diffraction technique has been used to identify the crystallized phases as well as the grain size of the nanocrystallites that develops due to annealing of the amorphous precursor. Fig.5.3 (a, b) show the XRD patterns for all the samples in the amorphous state. It clearly shows the amorphous nature of all the samples since no sharp peak corresponding to any crystalline peaks is observed, rather a broad defused halo peaks covering $2\theta = 10^\circ$ is observed. This hump type broad peak is generally observed for amorphous alloys of FINEMET type composition centering at 45° , which corresponds to fundamental peak at (110) plane with 100% intensity of their crystalline bcc-Fe (Si) phase. The origin of this hump is short range atomic ordering.

Fig. 5.4 (a-f) demonstrates the X-ray diffraction patterns of five samples with $x = 1, 3, 10, 12, 15$ & 17.5 annealed at various temperatures. It is observed from fig. 5.4 (a, b) that the broad defuse hump at $2\theta = 45^\circ$ become sharper and the peak intensity increases as the annealing temperature T_a , increases to $T_a = 540^\circ\text{C}$. In addition another peak centering around 65° develops corresponding to (200) plane of bcc-Fe (Si). After analysis of these peaks using computer software (high score) and comparing with the standard value of bcc-Fe(Si) phase, it has been confirmed that the newly evolved phase in the amorphous matrix is bcc-Fe(Si). The XRD pattern of $x = 10, 12.5, 15$ & 17.5 annealed $520, 540, 560$ & 600°C are shown in fig. 5.4 (c-f). For the sample with $x =$

12.5 crystallization seems to start at $T_a = 540^{\circ}\text{C}$ while for $x = 15$ & 17.5 no evidence of crystallization is observed even at $T_a = 560^{\circ}\text{C}$ & 580°C respectively. Only at $T_a = 600^{\circ}\text{C}$ crystallization seems to start for the sample $x = 17.5$. Since the onset of crystallization temperature for the sample with $x = 15$ is 580°C (see table-5.1), it is quite obvious that crystallization cannot take place at $T_a = 560^{\circ}\text{C}$. The grain size D_g , of the crystallites have been calculated from the line broadening of the fundamental peak (110) using Scherrer's formula

$$D_g = \frac{0.9\lambda}{\beta \cos \theta}, \quad (5.2)$$

where D_g is the grain size, β is the full width at half maximum (FWHM) and λ is the wave length of Cu- K_{α} radiation.

It has been observed that the grain size decreases with the increase of Cr content. Grain size is found to be 9.0, 8.6, 8.0, 7.0, 6.5 nm for Cr content $x = 1, 2, 3, 4, 5$ annealed at 540°C for 30 min. respectively. It again confirms that the Cr enhances the thermal stability against crystallization as well as controls the grain growth. Marvin *et al.* [5.13] found a grain size of 4 nm for the FINEMET alloy with Fe substituted by 10 at.% Cr annealed at 818 K which increases to 15 nm at $T_a = 873$ K. The authors found a satisfactory agreement of this XRD grain size with the TEM result. The evolution of grain size with annealing temperature has been determined on FINEMET composition with T_a substituted for Nb and Au for Cu [5.14, 5.15]. It was observed that grain size increased from 5 nm for the sample annealed at 500°C for 30 min. to a limiting value of 12-14 nm between annealing temperature of 525° and 650°C .

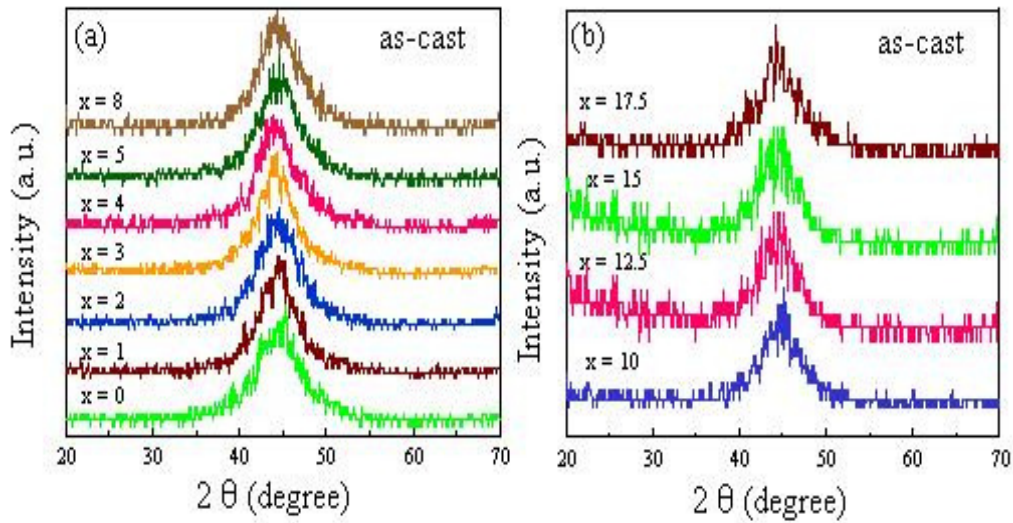


Fig. 5.3 XRD patterns of amorphous ribbons of $\text{Fe}_{73.5x}\text{Cr}_x\text{Cu}_1\text{Nb}_3\text{Si}_{13.5}\text{B}_9$ alloys in the as cast condition: (a) $x = 0, 1, 2, 3, 4, 5$ & 8 (b) $x = 10, 12.5, 15$ & 17.5

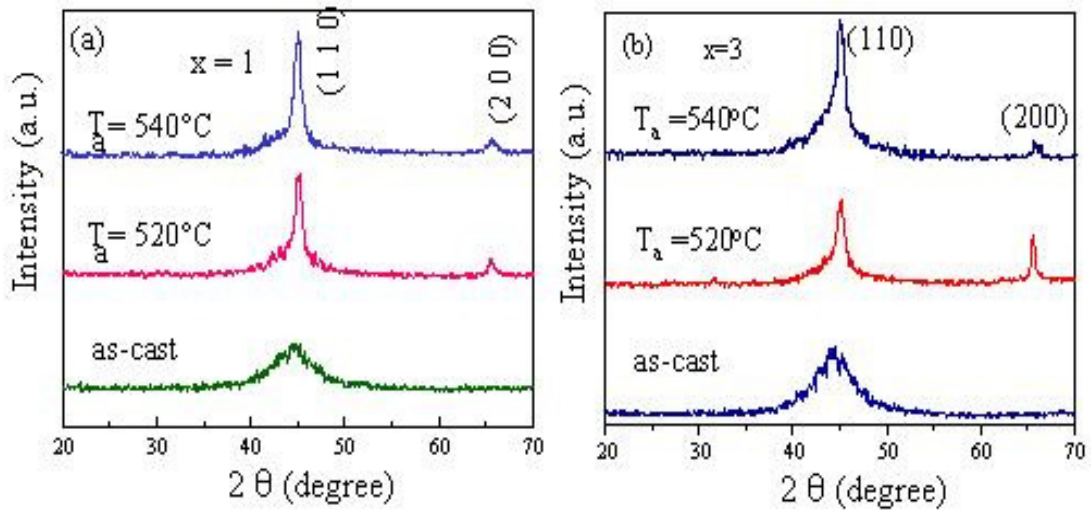


Fig. 5.4 XRD patterns of $\text{Fe}_{73.5x}\text{Cr}_x\text{Cu}_1\text{Nb}_3\text{Si}_{13.5}\text{B}_9$ alloys in the as cast condition and annealed at different temperatures: (a) $x = 1$ (b) $x = 3$

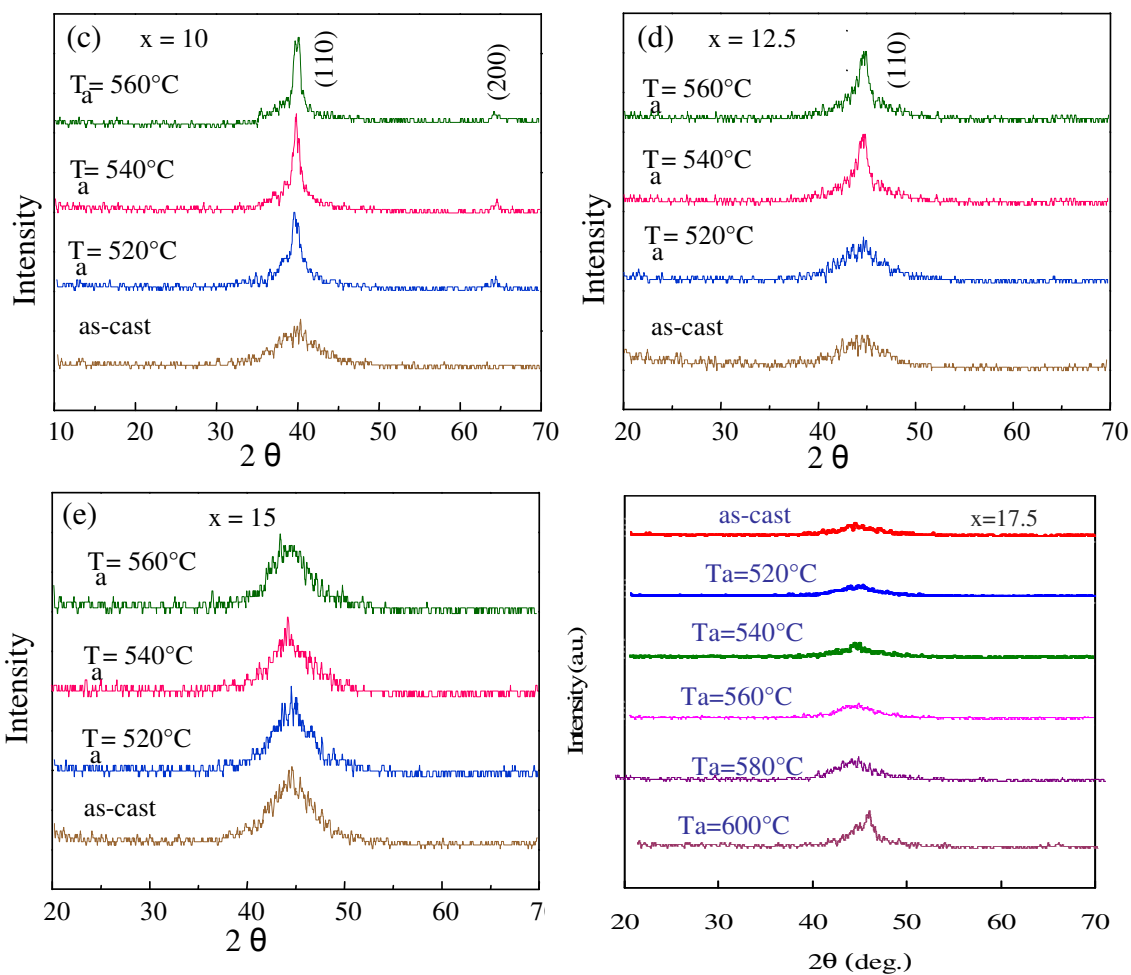


Fig. 5.4 XRD patterns of $\text{Fe}_{73.5x}\text{Cr}_x\text{Cu}_1\text{Nb}_3\text{Si}_{13.5}\text{B}_9$ alloys in the as cast condition and annealed at different temperatures: (c) $x = 10$ (d) $x = 12.5$ (e) $x = 15$ (f) $x = 17.5$

5.2 Magnetization Measurements

5.2.1 Saturation Magnetization

Saturation magnetization (M_s) a basic quantity of magnetic materials has been measured using a SQUID magnetometer. Fig. 5.5 (a) and 5.5 (b) shows magnetization curves at 5K and 300K respectively. It is evident from the curves that the magnetization is saturated for all the studied samples with $x = 0$ to 17.5 measured at 5K. This implies that all the studied samples are ferromagnetic at 5 K. In contrast, magnetization measured at 300K, the samples with $x = 0$ to 10 are saturated with an applied field of 8 kOe. The samples with Cr content $x \geq 12.5$ do not show any sign of ferromagnetic nature, rather a very small value of magnetization is observed which increases almost linearly up to the field of $H = 8$ kOe. The $M \sim H$ curves of these samples show typical characteristics of paramagnets at room temperature. But they are ferromagnetic at $T = 5$ K as shown in fig.5.5 (a).

The saturation magnetization values of all the studied samples at 5K and 300K are shown in table-5.2. It is evident from the results that the M_s decreases as the Cr contents increase. This may be attributed to the dilution of Fe magnetic moment by the substitution of non magnetic Cr. Saturation magnetization value of $M_s = 160$ emu/gm and 137 emu/gm measured at 5 K and 300 K respectively for the $x = 0$ which decreases monotonically with the successive substitution of Fe by Cr and attains a value of $M_s = 52.2$ emu/gm at 5K for $x = 17.5$. The saturation magnetization value M_s for the original FINEMET alloy i.e. $x = 0$ was found to be comparable within an experimental error of $\pm 5\%$ by several investigators [5.16-5.18].

Table-5.2 Curie temperature and magnetic parameters (5K & 300K) of nanocrystalline $\text{Fe}_{73.5-x}\text{Cr}_x\text{Cu}_1\text{Nb}_3\text{Si}_{13.5}\text{B}_9$ alloys

Cr content x (at.%)	Curie temperature, T_c in K	Saturation magnetization, M_0 in emu/g at 0K	Saturation magnetization, M_s in emu/g at 5K	Saturation magnetization, M_s in emu/g at 300K	Magnetic moment, n_B in Bohr magneton at 5K	Magnetic moment, n_B in Bohr magneton at 300K
0	596	160.3	160	137	1.41	1.21
1	566	155.3	155	130	1.37	1.15
2	540	147.6	147	115	1.29	1.01
3	517	133.4	133	111	1.17	0.98
4	490	127.8	127	99	1.12	0.87
5	466	122.9	122	89	1.07	0.78
6	435	119.7	119	87	1.04	0.76
7	412	111.2	111	72	0.97	0.63
8	390	107.8	107.6	65.2	0.94	0.58
9	371	103.1	101	56.2	0.88	0.5
10	364	92.8	92.5	48.18	0.81	0.42
12.5	247	72.6	72.5	3.33*	0.63	0.03
15	196	67.2	67	2.42*	0.58	0.02
17.5	143.5	52.8	52.2	2.14*	0.45	0.02

* Not saturation magnetization, M_s ; it defines magnetization value at H=1 Tesla.

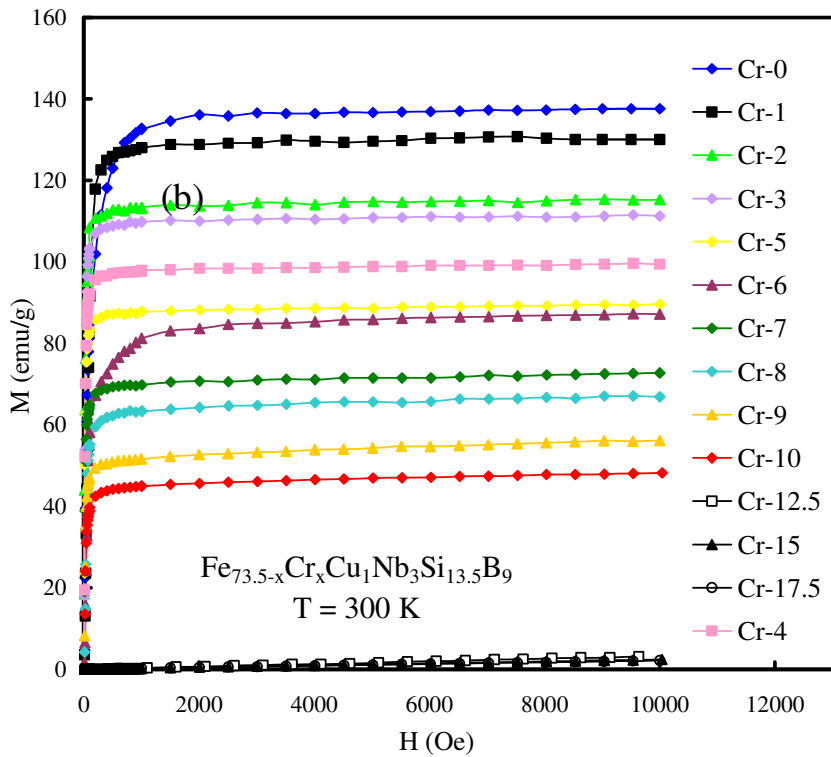
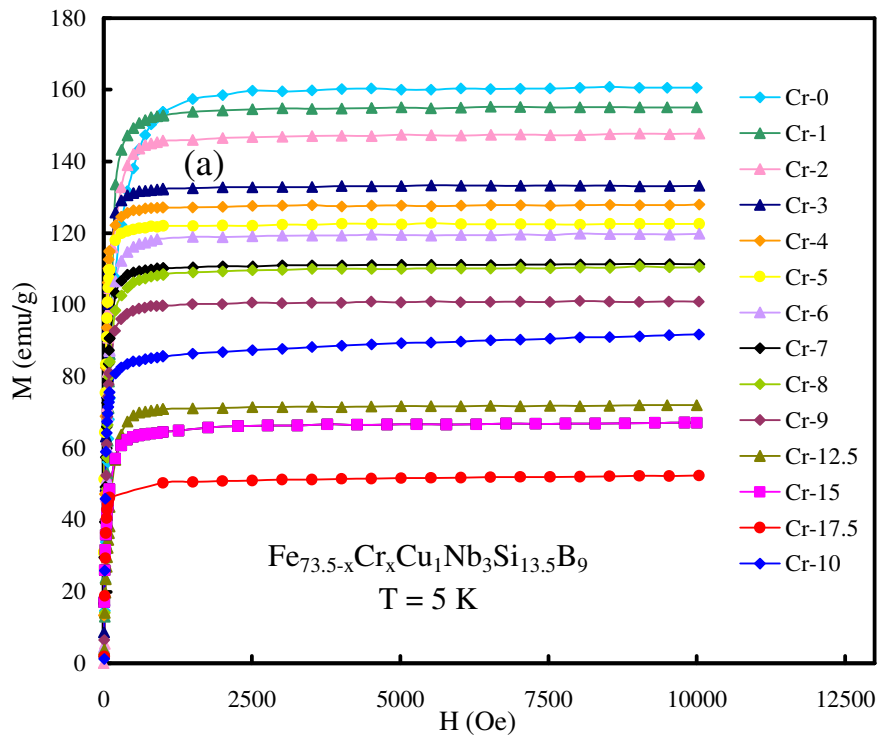


Fig.5.5 Field dependence of magnetization of amorphous $\text{Fe}_{73.5-x}\text{Cr}_x\text{Cu}_1\text{Nb}_3\text{Si}_{13.5}\text{B}_9$ ribbons with $x = 0, 1, 2, 3, 4, 5, 6, 7, 8, 9, 10, 12.5, 15$ & 17.5 alloys at (a) 5K and (b) 300K

5.2.2 Curie Temperature

Curie temperature is a primary intrinsic property of magnetic materials. A material is ferromagnetic if it possesses regions of finite magnetization where the external magnetic field intensity $H = 0$. The temperature at which ferromagnetism occurs is called the Curie temperature (T_c) and depends on the strength of exchange interaction which arises from the overlapping of the electronic wave functions of the interacting magnetic atoms. It is more appropriate from the fundamental point of view to find out the T_c from the appearance of spontaneous magnetization on decreasing the temperature (cooling) than the vanishing of spontaneous magnetization as the temperature is increased (warming) because of many complexities of the co-operative phenomena, in particular domain wall motion. In general determination of T_c is not that straight forward as it seems to be from the first principle and the unique value of T_c can be determined without ambiguity only when the material under study is perfectly homogeneous, single phase, defect free and of high purity.

The Curie temperature of the studied samples has been determined by various methods such as temperature dependence of high and low field dc magnetization, low field ac susceptibility and initial permeability ($H = 10^{-3}$ Oe), Arrott plots etc. Fig. 5.6 shows the temperature dependence of permeability (μ) of some representative curves of the samples with $x = 1, 3, 5$ & 8 measured by an inductance meter in conjunction with a tubular furnace. Curie temperature has been taken as that temperature where the $\frac{\delta\mu}{\delta T}$ attains its maximum value.

It is observed that the Curie temperature decreases with increase of Cr content and may be attributed to the reduction of exchange interaction between Fe magnetic moment. A gradual decrease of permeability below T_c is a manifestation of the Hopkinson effect, according to which the initial permeability as a function of temperature increases to a maximum value just below T_c and then drops off to a small value [5.19]. This is attributed to the temperature dependence of intrinsic magnetic anisotropy and domain

wall mobility. This is to note that the samples with $x \geq 5$ at.% Cr, the decrease of permeability below the Hopkinson peak is faster than those of low Cr content samples. This implies that the magnetic hardening occurs in those higher Cr content alloys, which increases with the Cr content as well as with the decreasing temperature originating from the increase of the magnetic anisotropy and thermal activation. Similar magnetic hardening of higher content amorphous alloys has been observed in the temperature dependence of ac susceptibility and field-cooled dc magnetization measurements, which would be discussed later on in the relevant section.

Fig. 5.7 shows the temperature dependence of saturation magnetization measured with an applied field of 10 kOe in the temperature range 5-700K for the sample with $x = 1, 2, 3, 6$ & 8 in the as cast condition. All the samples of this studied system have been measured, but the representative curves of the above-mentioned samples are shown for clarity. From these curves Curie temperature (T_c) has been determined as the temperature corresponding to the inflexion point where the rate of change of magnetization with respect to temperature is maximum. The Curie temperature determined in this method varies from 596 K for $x = 0$ to 142 K for $x = 17$ at.% Cr within an experimental uncertainty of ± 2 K since magnetization was recorded at an interval of 2K.

It is clearly observed from the curves of Fig. 5.7 that the saturation magnetization of the samples at low temperature decreases gradually with the increase of Cr content. Similarly, Curie temperature decreases gradually as the Cr content is increased. It is also noticed that the magnetization at low temperature decreases slowly with the increase of temperature and falls faster near the Curie temperature. Fig.8 shows the low field ($H = 20$ Oe) $M \sim T$ curves for the samples with Cr content $x = 10, 12.5, 15$ & 17.5 from which T_c values has been determined as the inflexion point. This is note that low field dc magnetization is a unique method of determining the magnetic phase transition temperature known as the “kinkpoint” method originally pioneered by L. Neel at strassbourg (France) in the school of magnetism in the early thirties of the last century [5.20]. It was later named as “kink point Locus” by Wojtowicz *et al.* [5.21]. According to this method

magnetization is observed fairly constant until the appearance of a “kink point” beyond which magnetization sharply falls to zero. The temperature corresponding to the “kink point” is considered as the ferromagnetic Curie temperature (T_c). The reason for the temperature independent part of magnetization below T_c is due to demagnetizing field

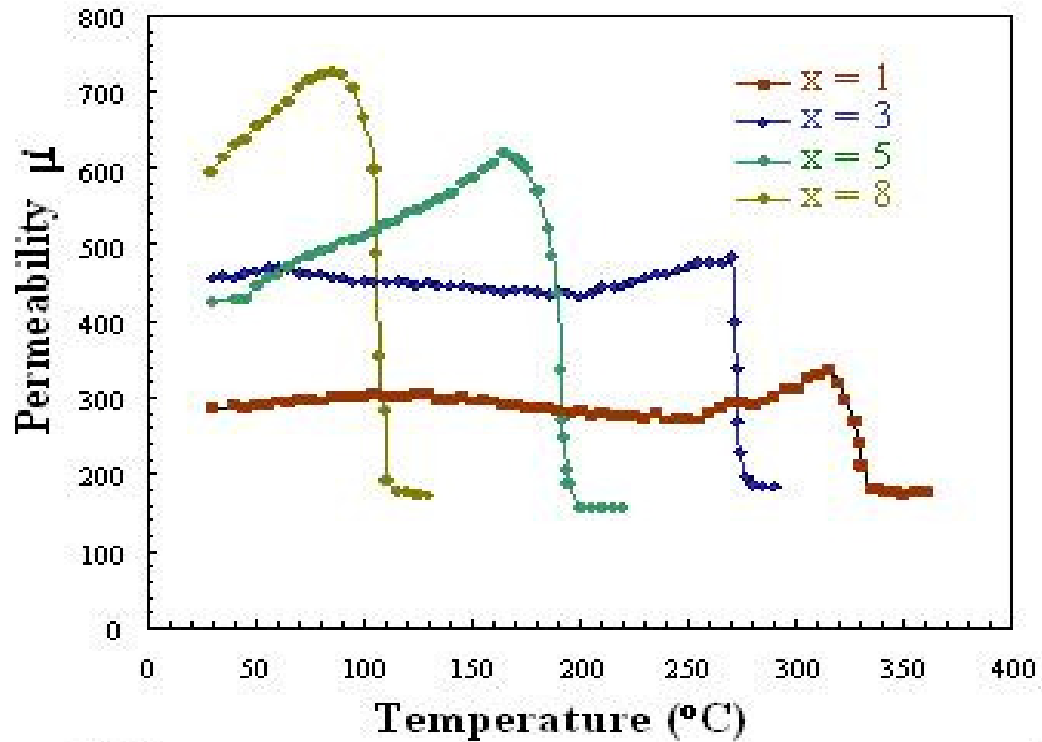


Fig. 5.6 Temperature dependence of permeability of amorphous ribbons with composition $Fe_{73.5-x}Cr_xCu_1Nb_3Si_{13.5}B_9$ [$x = 1, 3, 5$ & 8] alloys

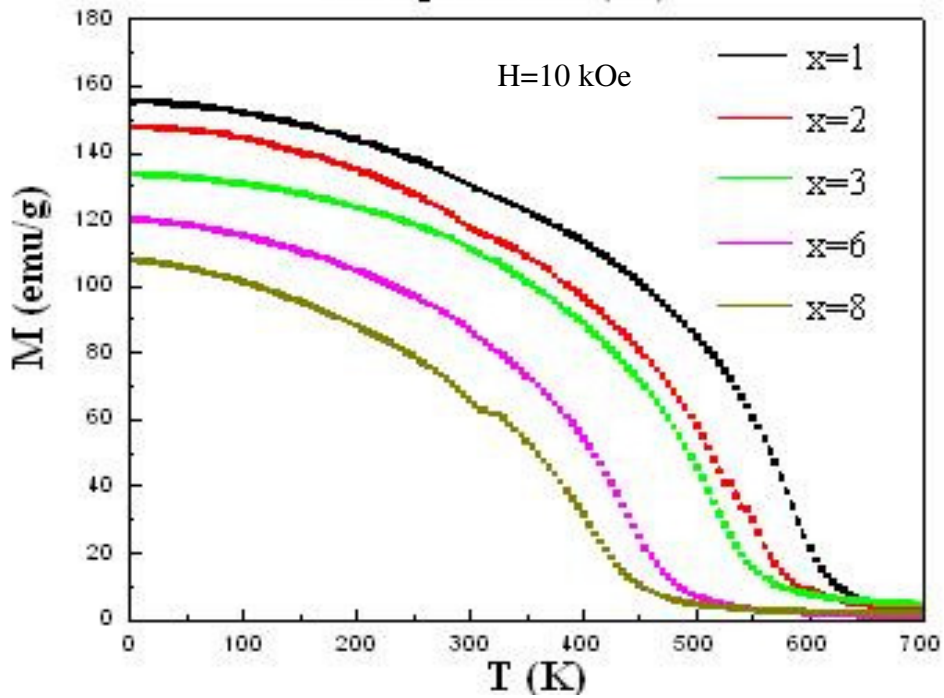


Fig. 5.7 Temperature dependence of magnetization of amorphous ribbons with composition $\text{Fe}_{73.5-x}\text{Cr}_x\text{Cu}_1\text{Nb}_3\text{Si}_{13.5}\text{B}_9$ [$x = 1, 2, 3, 6 \& 8$]

that limits the magnetization to a value $M = \frac{H_a}{D_s}$ (where H_a is the applied magnetic field and D_s is the shape- dependent demagnetization factor), producing a magnetization that is temperature independent below the “kink point”. But, in fig. 5.8 the “kink” has not been observed so distinctly and the magnetization is not observed independent of temperature with an applied field of $H = 20$ Oe, rather a smearing effect is observed. It is possibly due to high value of applied field ($H = 20$ Oe), which is higher than the demagnetizing field (H_k). Therefore temperature corresponding to maxima of $\frac{dM}{dT}$ has been taken as the Cuire temperature. The Curie temperatures determined by low field (20 Oe) dc magnetization measurements are found to be $T_c = 364, 245, 195 \& 149$ K for $x = 10, 12.5, 15 \& 17.5$ at.% Cr respectively. These values are within $\pm 2\text{K}$ with high field $M(T)$ and $\mu(T)$ measurements. M vs. T measurements have been performed with $H = 1$ Oe to see the effect of still lower field which will be discussed later on.

Ac susceptibility is a powerful tool to discern the Curie temperature. Temperature dependence of real part of ac susceptibility χ'_{ac} at frequencies 1.7, 17 & 170 Hz with an applied ac driving field $H_{ac} = 2$ Oe is depicted in Fig. 5.9 for the $x = 12.5$ sample. It is found that the χ'_{ac} measured at all three frequencies are superimposed. The susceptibility χ'_{ac} fall rapidly toward zero just above the Curie temperature. The T_c has been taken as the temperature corresponding to the maxima of $\frac{d\chi'}{dT}$ as proposed by Maartense *et al.* [5.22] and found to be $T_c = 245 \pm 1$ K. This value has good coincidence with the $T_c = 245$ K determined by low field dc magnetization as shown in Fig. 5.8. Fig. 5.10(a) 5.10(b) show the χ'_{ac} vs T curves for the samples $x = 15$ & 17.5, where susceptibility values measured at different frequencies are superimposed, i.e χ'_{ac} is independent of frequency. A sharp fall of susceptibility at the Curie temperature $T_c = 194$ K and 142K for the sample $x = 15$ & 17.5 respectively, signifies the homogeneity of the sample. From the χ'_{ac} vs. T curves, it is clearly observed that χ'_{ac} decreases gradually with the decrease of temperature for all the samples with sudden drop of χ'_{ac} for the sample $x = 17.5$. This is due to the magnetic hardening effect of higher Cr content alloys resulting from the increase of anisotropy energy as the temperature is lowered.

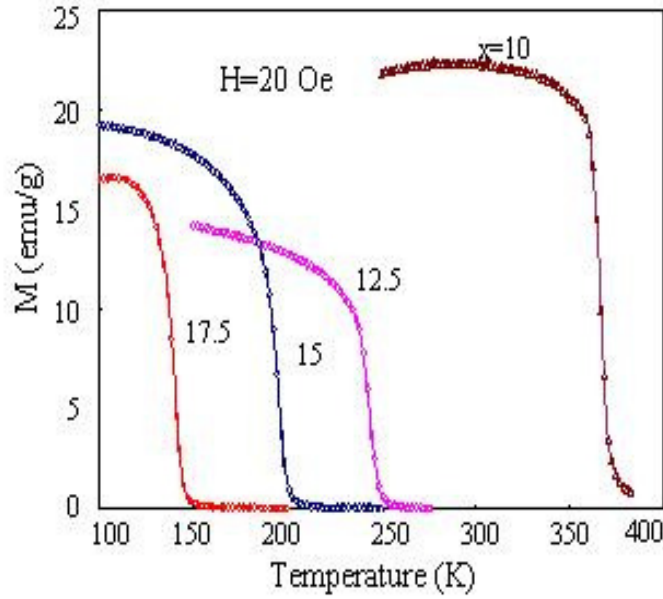


Fig.5.8. Temperature dependence low field dc magnetization ($H = 20$ Oe) of amorphous ribbons with composition $\text{Fe}_{73.5-x}\text{Cr}_x\text{Cu}_1\text{Nb}_3\text{Si}_{13.5}\text{B}_9$ [$x = 10, 12.5, 15$ & 17.5] alloys

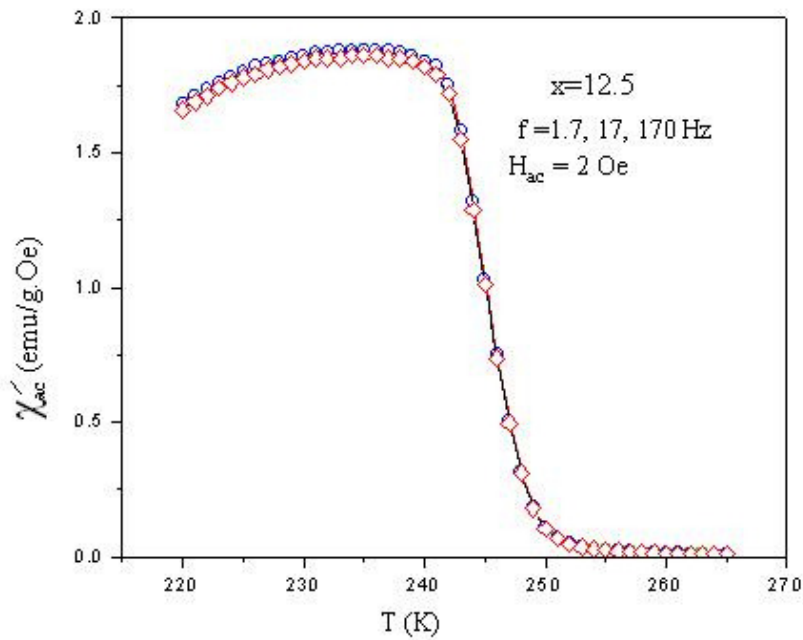


Fig. 5.9 Temperature dependence of ac susceptibility (real χ') with ac driving field of $H_{ac} = 2$ Oe for the amorphous ribbon with composition $\text{Fe}_{61}\text{Cr}_{12.5}\text{Cu}_1\text{Nb}_3\text{Si}_{13.5}\text{B}_9$ at different frequencies

The Curie temperatures determined by both dc and ac techniques are well correlated. More over Curie temperature (T_c) of the samples with $x = 10, 12.5, 15$ & 17.5 have also been determined from the magnetic isotherm taken around the T_c with an interval of 1-2K using the ABK (Arrot-Belov-Kouvel) plot [5.23-5.25]. A standard procedure for determining T_c in ferromagnetic materials is based on symmetry principle. Arrott [5.10] have pioneered the use of a classical form of expression for magnetization and field near a ferromagnetic phase transition and showed that internal field, H_i , should be an odd power of magnetization M , and is given by

$$H_i = A(T - T_c)M + BTM^3 + CTM^5 \quad (5.3)$$

where A, B, C are constants.

Since $M \ll M_s$, the saturation magnetization around T_c , the terms involving M^5 and higher can be neglected, so that the equation can be written as

$$H_i = A(T - T_c)M + BTM^3 \quad (5.4)$$

$$\frac{H_i}{M} = A(T - T_c) + BTM^2 \quad (5.5)$$

$$\text{At } T = T_c; \quad \frac{H_i}{M} = BT_c M^2 \quad (5.6)$$

An approach to T_c is characterized by vanishing of the parameter A . B is the temperature dependent parameter. Therefore, a value of T_c may be determined from the magnetic isotherms by plotting at fixed temperatures $\frac{H_i}{M}$ vs. M^2 . According to equation

(5.4) these plots should yield straight lines for each value of T and T_c corresponds to that straight line which passes through the origin for a low enough fields, H_i . These plots are called Arrott-Belov-Kouvel (ABK) plots and sometime shortly called Arrott plots. Arrot plots not only determine T_c , but also give spontaneous magnetization M_0^2 ($\frac{H}{M} = 0$) from the intercepts on M^2 axis for $T < T_c$ and reciprocal of initial

susceptibility $\frac{1}{\chi_0}$ ($H \rightarrow 0$) from the intercepts on the $\frac{H_i}{M}$ axis for $T > T_c$.

Fig. 5.11(a) and 5.11(b) shows the representative curves of the magnetic isotherms measured around the T_c of the samples with $x = 12.5$ & 17.5 . From these magnetic isotherms calculations are made for M^2 and H/M to draw the ABK plots considering low field data which are demonstrated in fig. 5.12 (a, b, c, d). The estimated T_c values for $x = 10, 12.5, 15$ & 17.5 are 362, 247, 197 and 143.5 K respectively, which is quite compatible with other methods of measurements. The T_c values of all the studied samples are depicted in table-5.2. It is observed that the T_c decreases monotonically as in the case of M_s with the increase of Cr content. The reduction of T_c with the substitution of nonmagnetic Cr may be attributed to the simultaneous weakening of the strength of exchange interaction between the Fe magnetic moments. For $x = 0$, the Curie temperature, $T_c = 596\text{K}$ which decreases to $T_c = 143.5\text{K}$ for $x = 17.5$. However the T_c values depicted in table-5.2 are average over all types of measurements. The absolute values of all these T_c are within $\pm 2\text{K}$. In spite of careful determination of T_c of the amorphous alloys by various methods ambiguity of T_c values still remains a open question specially for the amorphous alloys because amorphous glassy metal alloys are basically metastable materials. It has been demonstrated by numerous experimental evidences that when the materials with the same compositions are produced with different quenching rate, magnetic properties, in particular the Curie temperature can vary substantially. This fact prevents a reliable comparison between results obtained by different laboratories [5.26]. The T_c of original FINEMET has been found to vary from 590K to 630K. Therefore the initial amorphous state should be taken into account.

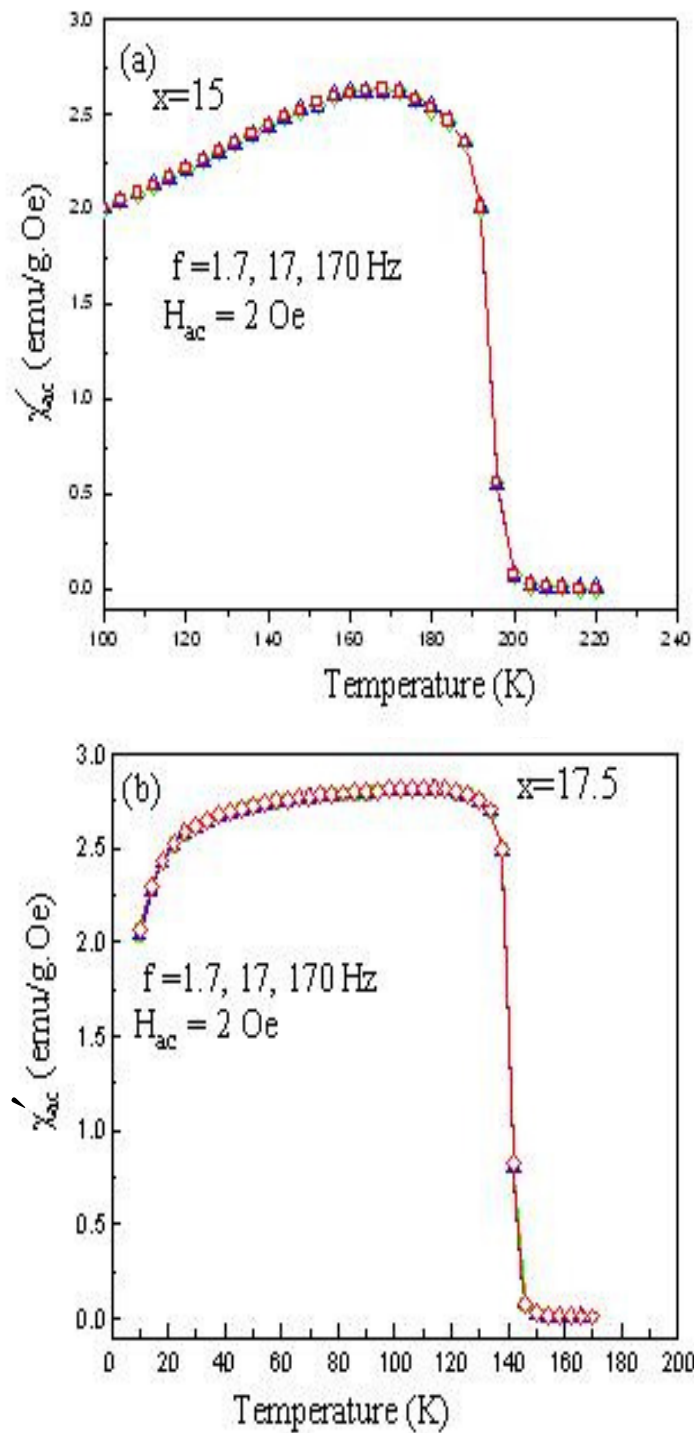


Fig. 5.10. Temperature dependence of the real part of ac susceptibility (χ') with driving field of $H_{ac}= 2 \text{ Oe}$ for the composition (a) $\text{Fe}_{58.5}\text{Cr}_{15}\text{Cu}_1\text{Nb}_3\text{Si}_{13.5}\text{B}_9$ and (b) $\text{Fe}_{56}\text{Cr}_{17.5}\text{Cu}_1\text{Nb}_3\text{Si}_{13.5}\text{B}_9$ at different frequencies

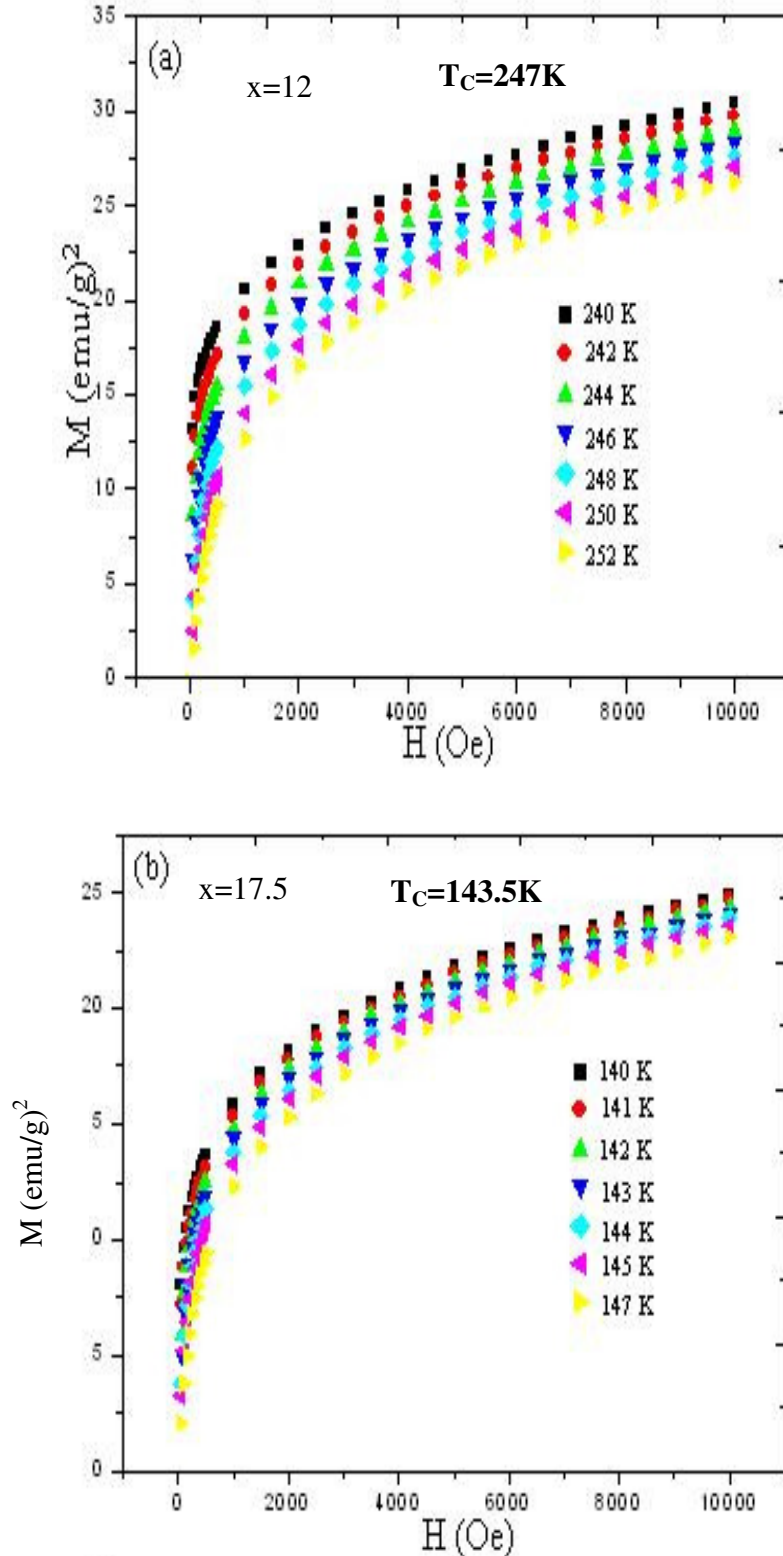


Fig. 5.11. Field dependence of magnetic isotherms (M vs. H) at different temperatures of the amorphous ribbons with composition (a) $Fe_{61}Cr_{12.5}Cu_1Nb_3Si_{13.5}B_9$ and (b) $Fe_{56}Cr_{17.5}Cu_1Nb_3Si_{13.5}B_9$ alloy.

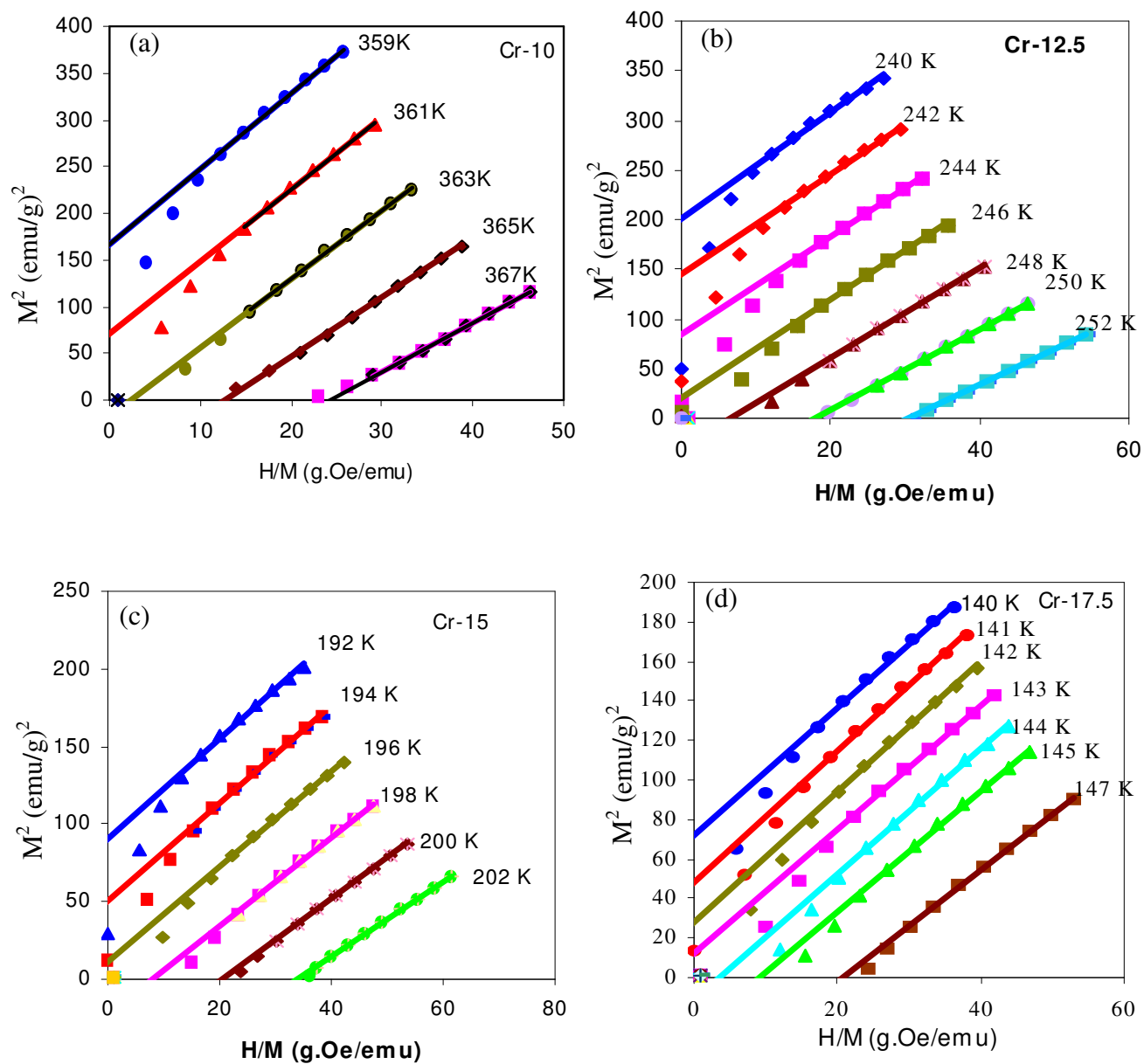


Fig. 5.12 (a,b,c,d). Arrot plots (M^2 vs. H/M) from the magnetic isotherms with composition $\text{Fe}_{73.5-x}\text{Cr}_x\text{Cu}_1\text{Nb}_3\text{Si}_{13.5}\text{B}_9$ ($x = 10, 12.5, 15$ & 17.5) alloys

5.2.3 Temperature Dependence of Magnetization

The variation of saturation magnetization (M_s) as a function of temperature in the range $T = 5\text{K}-1000\text{K}$ measured with an applied field of 10 kOe in the amorphous state for the samples with $x = 1, 2, 5, 6, 8$ and $x = 12.5, 15, 17.5$ are shown in fig. 5.13 (a) & 5.13 (b) respectively. During the magnetization measurements, the heating rate was always kept constant ($20^\circ\text{C}/\text{min}$). The magnetization of all the samples decreases gradually with increasing temperature since the thermal energy is acting on opposition to the magnetic coupling or exchange energy between neighboring atoms. As the temperature approaches to the Curie temperature, magnetization falls more rapidly toward zero as the thermal energy exceeds the magnetic ordering or the exchange energy. As a result the sample undergoes a ferro-paramagnetic phase transition at $T = T_c$ in the amorphous state. It is observed that the magnetization and the T_c of all the amorphous samples both decreases as the Cr content increase implying the effect of Cr on the dilution of magnetic moment as well as the weakening of exchange interaction between Fe magnetic moments respectively. In fig.5.13 (a) it is evidenced that from the temperature above T_c^{am} until 800K, magnetization value of the studied samples ($x = 1, 2, 5, 6, 8$) is nearly zero since they are paramagnetic in this temperature range. At $T=800\text{K}$ and above the crystallization behavior of the amorphous samples has been well demonstrated as the temperature continues to rise further.

The sharp rise of magnetization of all the amorphous samples in their paramagnetic state is connected to the onset of crystallization of $\alpha\text{-Fe}(\text{Si})$ ferromagnetic phase in the remaining amorphous matrix. The onset of primary crystallization temperature corresponds well with that of DSC thermogram measured with the same heating rate. The magnetization of this newly evolved ferromagnetic phase rises fast with the increase of temperature due to enhanced volume fraction of crystallized $\alpha\text{-Fe}(\text{Si})$ phase and passes through a maximum, beyond which it decreases to a very low value. It is clearly observed from the thermomagnetic curves shown in fig.5.13 (a) that the height of the peak related to the crystallization process of $\alpha\text{-Fe}(\text{Si})$ phase decreases remarkably with increasing Cr content indicating the stabilization effect of Cr against primary crystallization together with the reduction of magnetization of the nanograins. Similar

effect of substitution of Fe by Al in FINEMET has been observed by Zorkovska *et al.* [5.27]. The decrease of magnetization M after passing through the maximum is connected to the temperature dependence of magnetization of Fe(Si) crystalline phase which undergoes a FM-PM phase transition at $T \approx 600^\circ\text{C}$. This is to note that the onset of crystallization temperature T_{x1} and the peak temperature T_{p1} of Fe(Si) phase shifts to higher temperature as the Cr content of the alloys increases. These features suggest that the Cr addition enhances the thermal stability of the studied alloys against crystallization of α -Fe(Si) phase. The values of T_{x1} and T_{p1} are comparable with values obtained by DSC measurements in the present work. It is also noticed in the M_s vs. T curves as shown in fig. 5.13 (b) that the alloys with $X \geq 15$, no crystallization events are observed until $T = 1000\text{K}$. It indicates that the crystallization of Fe(Si) phase is completely suppressed for higher Cr content alloys which has also been confirmed in the DSC thermogram and explained earlier.

Fig. 5.13 (b) also shows the $M(T)$ cooling curve of $x = 12.5, 15$ & 17 which correspond to the fully crystallized samples. During cooling the magnetization rises sharply indicating a magnetic phase transition from paramagnetic-ferromagnetic. This phase transition corresponds to crystalline Fe(Si) that vary in their composition due to the thermal stability against crystallization as affected by Cr content. This shows a distribution of Curie temperatures of this phase between 825K and 900K . Fig. 5.14 shows the $M(T)$ curve for $x = 5$ during heating and cooling. The cooling curve $M(T)$ clearly demonstrates two-phase character. The high temperature phase transition of Fe(Si) crystalline phase takes place at around $T \approx 875\text{K}$ in both the heating and cooling cycle. But at lower temperature around 500K another magnetic phase transition (smeared and diffused) takes place during cooling which corresponds to the remaining amorphous phase after high temperature crystallization of Fe(Si), while during heating a well-defined Curie temperature $T_c = 466\text{K}$ has been determined for the amorphous state. From the above measurements it has been elucidated that the thermomagnetic measurement is a powerful technique to analyze the crystallization behavior of amorphous ferromagnetic materials provided the crystallization products are ferromagnetic and the T_c of the amorphous alloys lie below the crystallization

temperature. From the temperature dependence of magnetization, the saturation magnetization, $M_s(0)$ value at 0 K has been determined by extrapolating the low-temperature magnetization data and are shown in table 5.2.

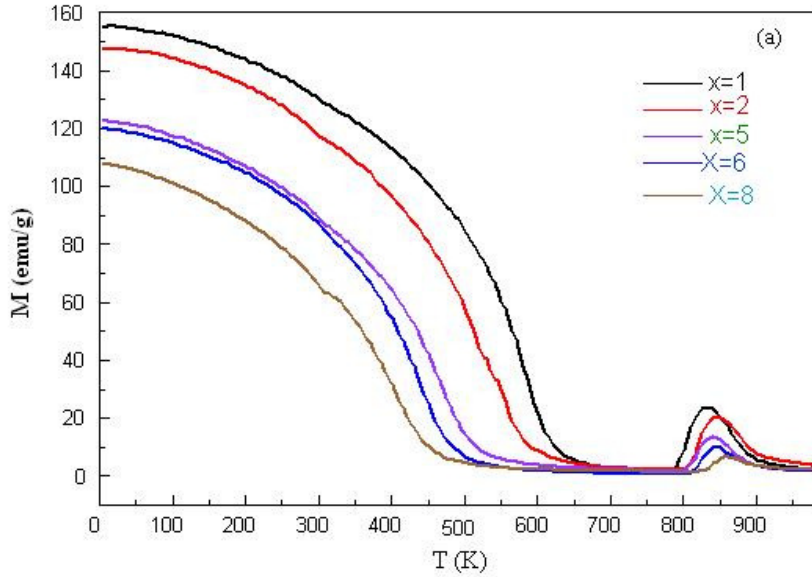


Fig. 5.13 (a) Thermomagnetic curves with an applied field of $H=1$ Tesla of amorphous $Fe_{73.5-x}Cr_xCu_1Nb_3Si_{13.5}B_9$ ribbons measured at the heating rate of $20^\circ C/min$ [$x = 1, 2, 5, 6$ & 8].

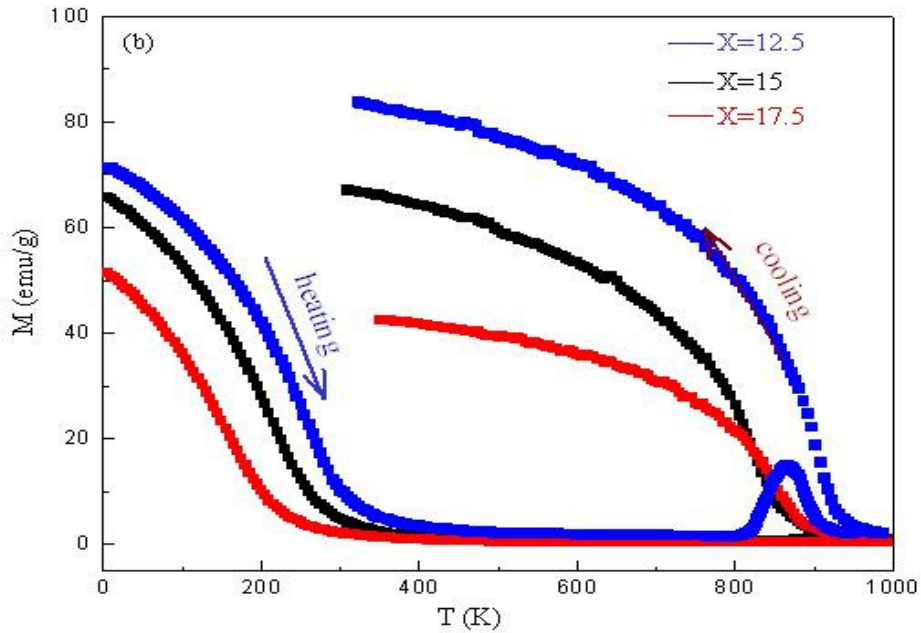


Fig. 5.13 (b) Thermomagnetic curves with an applied field of $H=1$ Tesla of amorphous ribbon with composition $Fe_{73.5-x}Cr_xCu_1Nb_3Si_{13.5}B_9$ measured at the heating rate of $20^\circ C/min$ [$x = 12.5, 15$ & 17.5] including the cooling curves

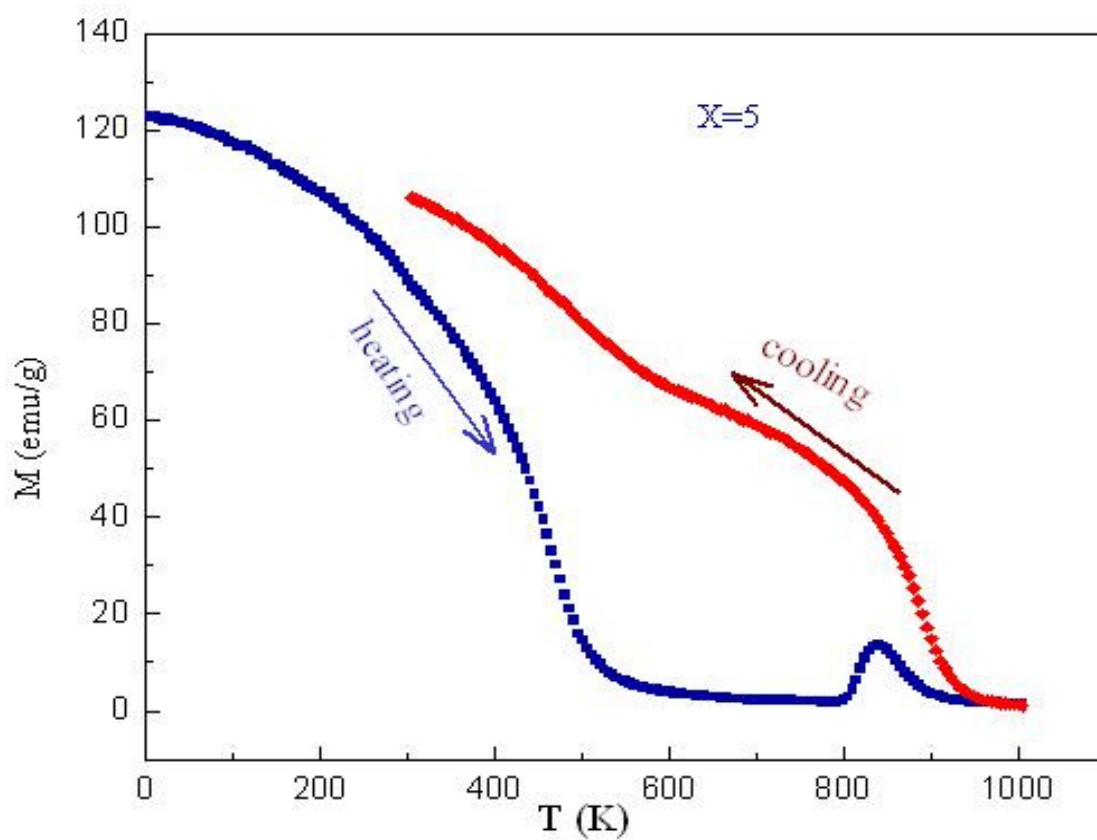


Fig. 5.14. Temperature dependence of saturation magnetization amorphous ribbon with composition $\text{Fe}_{73.5-x}\text{Cr}_x\text{Cu}_1\text{Nb}_3\text{Si}_{13.5}\text{B}_9$ with an applied field of $H = 1\text{ Tesla}$ during heating and cooling with $x = 5$

5.2.4 Variation of Magnetization M(0) and T_c with Cr Concentration for the Fe_{73.5-x}Cr_xCu₁Nb₃Si_{13.5}B₉ Alloys

The saturation magnetization M(0), M(5K), M(300K) and T_c with Cr content are shown in Table-5.2. The magnetic moment in Bohr magneton n_B has been calculated using the formula

$$n_B = \frac{AM(0)}{N\mu_B} \quad (5.7)$$

where A = molecular weight of alloy composition and M = Magnetization (emu/g) at 0 K.

The results are shown in table-5. 2. The dependence of magnetic moment n_B and T_c on Cr content in the studied alloy system Fe_{73.5-x}Cr_xCu₁Nb₃Si_{13.5}B₉ are demonstrated in fig. 5.15 (a, b) respectively. The variation of the magnetic moment of the amorphous alloys can be approximated by a straight line of the form n_B=1.3748-0.0552x.

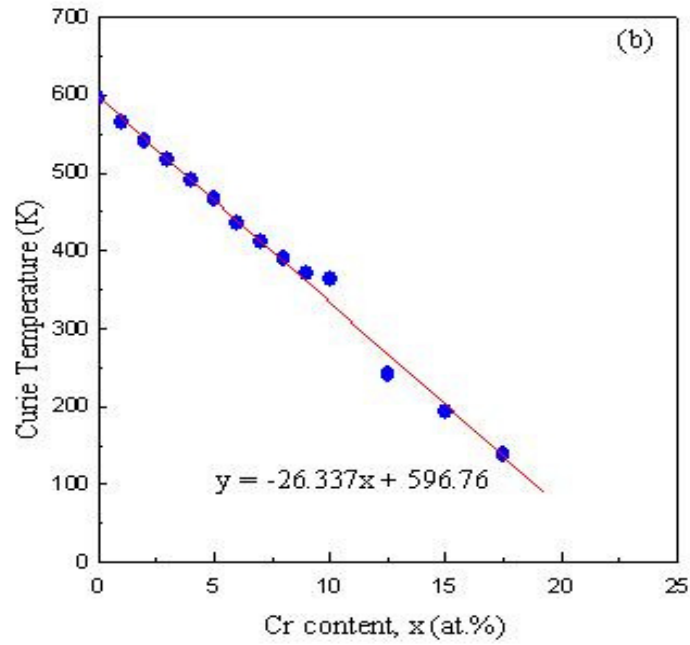
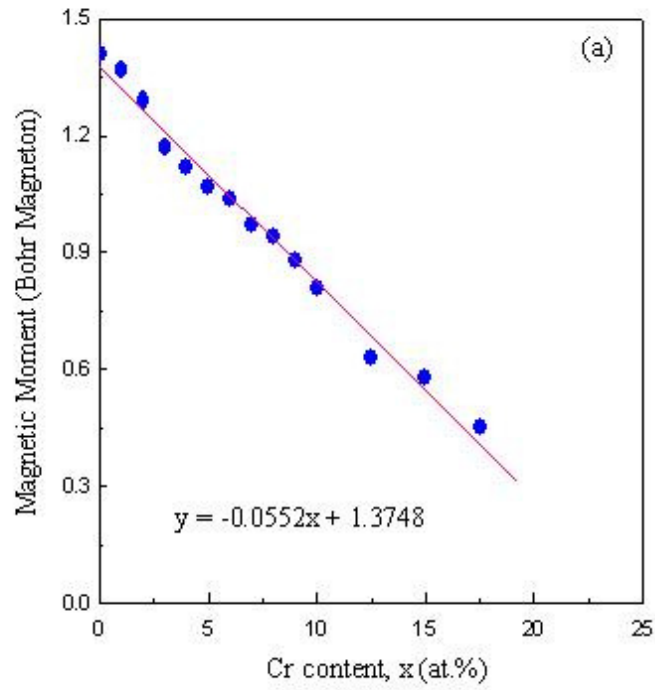


Fig. 5.15 Variation of (a) magnetic moment and (b) Curie temperature with the x content of amorphous $\text{Fe}_{73.5-x}\text{Cr}_x\text{Cu}_1\text{Nb}_3\text{Si}_{13.5}\text{B}_9$ ribbons

Magnetic moment for the entire composition range has been found to decrease linearly with the increase of Cr concentration. The decrease of magnetic moment is $0.055\mu_B$ for each atomic percent of Cr substitution. Compare with the Curie temperatures (T_c) is also found to depend linearly with the increasing Cr concentration. A least-square fitting of the experimentally determined T_c values against Cr concentration give a linear equation of the form $T_c = 596.76 - 26.337x$ from which a decrease of T_c by about 26°C per atomic percentage of Cr substitution has been determined. Kovac *et al.* [5.28] studied the dependence of magnetic moment and Curie temperature of Finemet alloys where Fe has been substituted for Cr with Cr = 4, 8, 11, 14, 17, 25). The authors found a linear decrease of magnetic moment at the rate of $0.047\mu_B / \text{Cr atom}$, while T_c decreased 25K per atomic percent of Cr. Our results are comparable with the result of Krishnan *et al.* [5.29] in their study of magnetic properties of $\text{Fe}_{40-x/2}\text{Ni}_{x/2}\text{Cr}_x\text{Si}_{10}\text{Mo}_2\text{B}_8$ alloys ($0 \leq x \leq 5$), found that decrease of magnetic moment is $0.053 \mu_B / \text{at.}\% \text{ Cr}$ while that of T_c is $40\text{K} / \text{at.}\% \text{ Cr}$. The rate of decrease of T_c is much higher than our results while compatible with results of Inomata *et al.* [5.30].

The critical concentration for the onset of ferromagnetism in this alloy system has been estimated to be $x_c = 24 \pm 1$ at % Cr by linear exploration of $n_B = 0$ and $T_c = 0$ as a function of Cr concentration. This value is in reasonable agreement with the value of $x_c = 26 \pm 1$ at % Cr reported by Kovac *et al.*[5.28].

5.2.5 Field Cooled and Zero Field Cooled Magnetization Behavior of Higher Cr Content Amorphous Alloys

Effect of magnetic field on a ferromagnetic material is dependent on the state of ordering of magnetization. Zero-field-cooled magnetization curves as a function of field and temperature $M_{ZFC}(H, T)$ of a magnetic material are the reflection of the domain structure of the individual material. When an ordered magnetic material is cooled in a zero external dc magnetic field from above its Curie temperature (T_c) and magnetization is measured during heating the sample with the application of low dc magnetic field, zero-field-cooled magnetization (M_{ZFC}) is obtained. In zero-field-cooled situation magnetic specimens are spontaneously magnetized under the influence of

internal molecular field and associated competition between exchange energy, anisotropy energy etc. which determines the formation of domains. So, $M_{ZFC}(T)$ gives the temperature dependence of virgin domain magnetization. In the field-cooled magnetization (M_{FC}), the sample is cooled through the Curie temperature with the application of a magnetic field and the magnetization is measured during cooling it to the desired temperature keeping the magnetic field applied throughout the measurement. In the case of field-cooled magnetization (M_{FC}) the external magnetic field greatly influences the domain formation since the magnetic moments are loosely coupled to each other above T_c . Therefore the virgin domain magnetization as effected by exchange and anisotropy energies is smeared out. It has been well demonstrated that M_{ZFC} curve below the Curie temperature is mainly determined by the magnetic anisotropy of the specific materials [5.31, 5.32] Therefore, it is expected that magnetically ordered materials will show divergence ($M_{FC} \neq M_{ZFC}$) below the Curie temperature between FC and ZFC magnetization when measured with a magnetic field less than the anisotropy field (H_k) associated with the specific material. This is associated with a corresponding change in the temperature dependence of coercivity, which in turn is proportional to the temperature dependence of anisotropy field.

M_{ZFC} and M_{FC} have been measured with an applied magnetic field of $H = 10\text{e}$ for the samples $x = 10, 12.5, 15 \text{ \& } 17.5$. Fig. 5.16 (a) and 5.16 (b) shows the representative curves for $x = 15 \text{ \& } 17.5$. The divergence between the M_{ZFC} and M_{FC} just below the T_c is observed for all the studied alloys, which increases with the decrease of temperature and also with the increase of Cr content. This phenomenon may be attributed to the increase of coercivity at low temperature, which is controlled by the magnetic anisotropy energy. It is noticed that the divergence between M_{FC} and M_{ZFC} at low enough temperature for $x = 17.5$ is higher than that of $x = 15$. From these measurements, the sharp fall of magnetization at $T = T_c$ is well demonstrated implying good homogeneity of the prepared samples. At the Curie temperature and above, the divergence between M_{FC} and M_{ZFC} is eliminated due to the vanishing of the magnetic anisotropy at $T = T_c$.

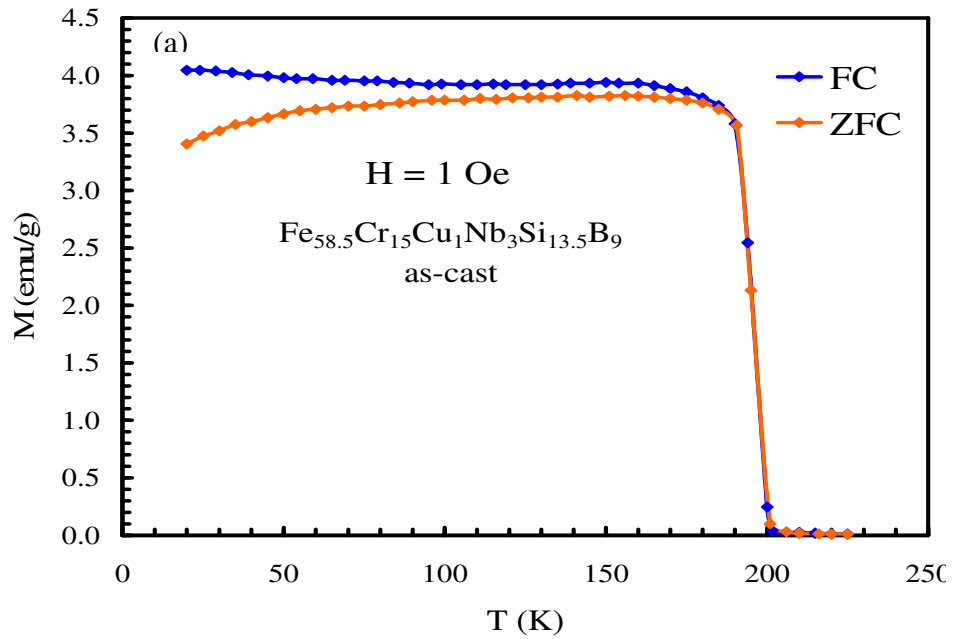


Fig. 5.16(a). Field-cooled (FC) and Zero Field-cooled (ZFC) magnetization curves with an applied field of 1 Oe for the amorphous ribbon with composition $\text{Fe}_{58.5}\text{Cr}_{15}\text{Cu}_1\text{Nb}_3\text{Si}_{13.5}\text{B}_9$

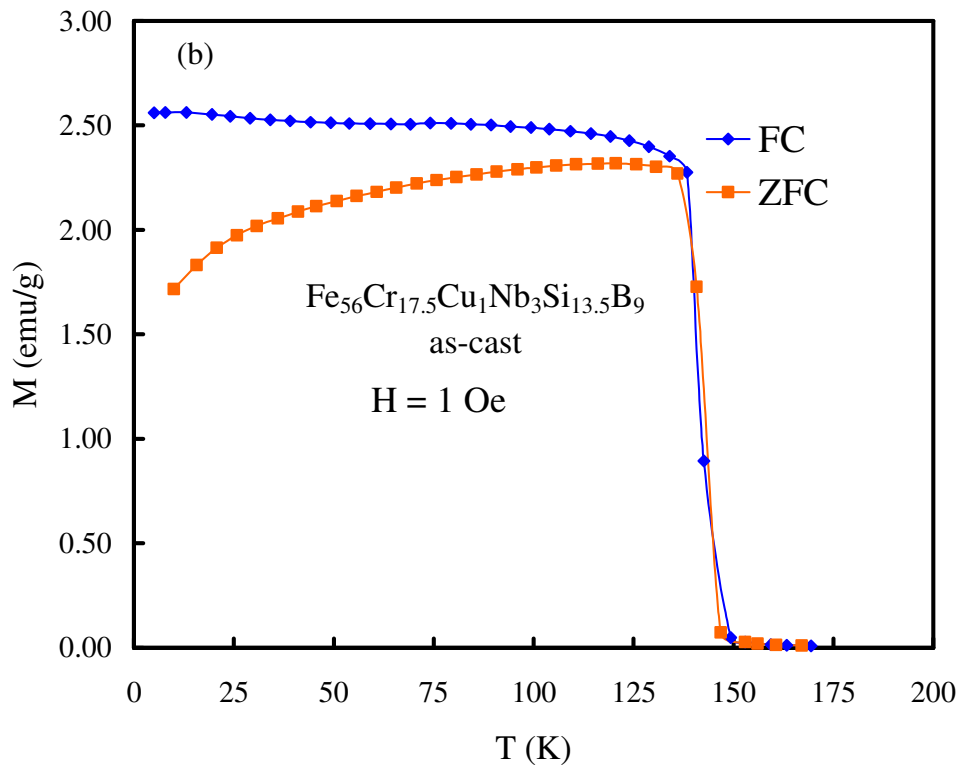


Fig. 5.16(b). Field-cooled (FC) and Zero Field-cooled (ZFC) magnetization curves with an applied field of 1 Oe for the amorphous ribbon with composition $\text{Fe}_{56}\text{Cr}_{17.5}\text{Cu}_1\text{Nb}_3\text{Si}_{13.5}\text{B}_9$

5.2.6 Low Temperature Magnetic Behavior of the Amorphous Alloys

It is well known that metallic glasses (amorphous) exhibit spin wave excitation [5.33-5.35]. The alloys under study are FINEMET type of amorphous alloys with composition $\text{Fe}_{73.5-x}\text{Cr}_x\text{Cu}_1\text{Nb}_3\text{Si}_{13.5}\text{B}_9$ ($x = 0, 1, 2, 3, 4, 5, 6, 7, 8, 9, 10, 12.5, 15 \text{ \& } 17.5$) in the as-prepared condition. In order to verify whether these alloys also exhibit spin wave excitation, the low temperature magnetization measurement as a function of temperature from 5K to 300K with an applied magnetic field of 1 Tesla has been carried out. The experimental behavior of the saturation magnetization at low temperature was found to follow the Bloch's spin-wave theory according to the following equation [5.36, 5.37]:

$$M(T) = M_0 \left(1 - BT^{\frac{3}{2}} - CT^{\frac{5}{2}} \right) \quad (5.8)$$

where M_0 is the saturation magnetization extrapolated at 0 K, B & C are the constants. Generally, the low temperature behavior of the saturation magnetization of crystalline ferromagnetic materials can be described within reasonable errors by the first two terms of equation (5.8) covering narrow range of temperature i.e. $0.2 T_c$.

Fig. 5.17 (a, b) shows the temperature dependence of magnetization from 5K to 300K for all the samples. It is observed that the magnetization relaxes gradually with the increase of the Cr content and temperature.

Fig. 5.18 (a, b) demonstrates reduced magnetization $\frac{M(T)}{M(0)}$ vs. $T^{\frac{3}{2}}$ in the temperature

range of 5K to 200 K. It is observed that Bloch's $T^{\frac{3}{2}}$ law is generally obeyed by all the compositions and the temperature range of the fitting has been extended to much higher temperature ($0.6 T_c$ to $0.8 T_c$) than found in conventional crystalline ferromagnet. The data were fitted with a straight line by a linear regression. The slop of the line gives the constant B which was used to calculate D from the equation (3.29).

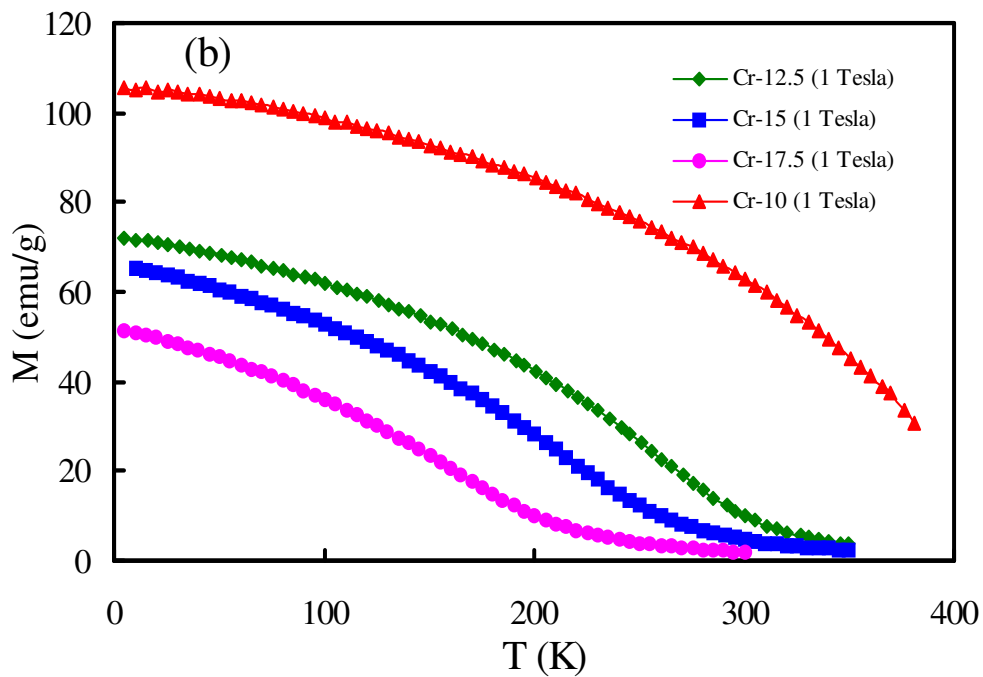
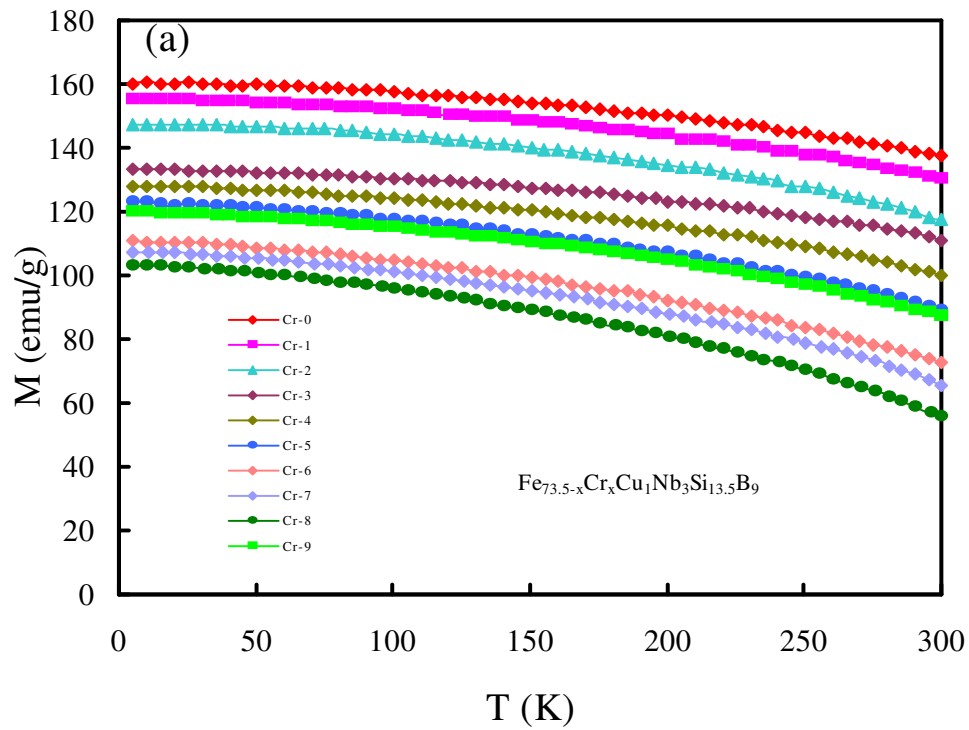


Fig. 5.17 Temperature dependence of magnetization of amorphous $Fe_{73.5-x}Cr_xCu_1Nb_3Si_{13.5}B_9$ ribbons with an applied field 1 Tesla for (a) $0 \leq x \leq 9$ and (b) $10 \leq x \leq 17.5$

However, inclusion of higher temperature term $T^{\frac{5}{2}}$ of the equation (5.8) an attempt has been taken to fit the experimental data of $M(T)$ up to $0.6 \leq \frac{T}{T_c} \leq 0.8$ for all the samples which show also quite good fitting as shown in Fig. 5.19 (a, b) using the relation

$$\frac{\Delta M}{M_0} = \frac{M_0 - M(T)}{M_0} = BT^{\frac{3}{2}} + CT^{\frac{5}{2}} \quad (5.9)$$

This indicates that the contribution to magnetization in this temperature range is from low and high-energy spin density waves.

The values of the coefficients B determined from the curves in fig. 5.18 have been used to fit the nonlinear curves in fig.19 (a, b) considering the high temperature term $T^{5/2}$ by adjusting the value of B and C for best fitting. The spin wave stiffness constant D and the mean square value of the range of exchange interaction $\langle r^2 \rangle$ was calculated by using equation (3.31) [5.35].

The values of the coefficient B, C, spin-wave stiffness constant D, the mean square value of the range of exchange interactions $\langle r^2 \rangle$, $\frac{C}{B}$ ratio and M_0 are shown in table-5.3 together with the value of crystalline Fe.

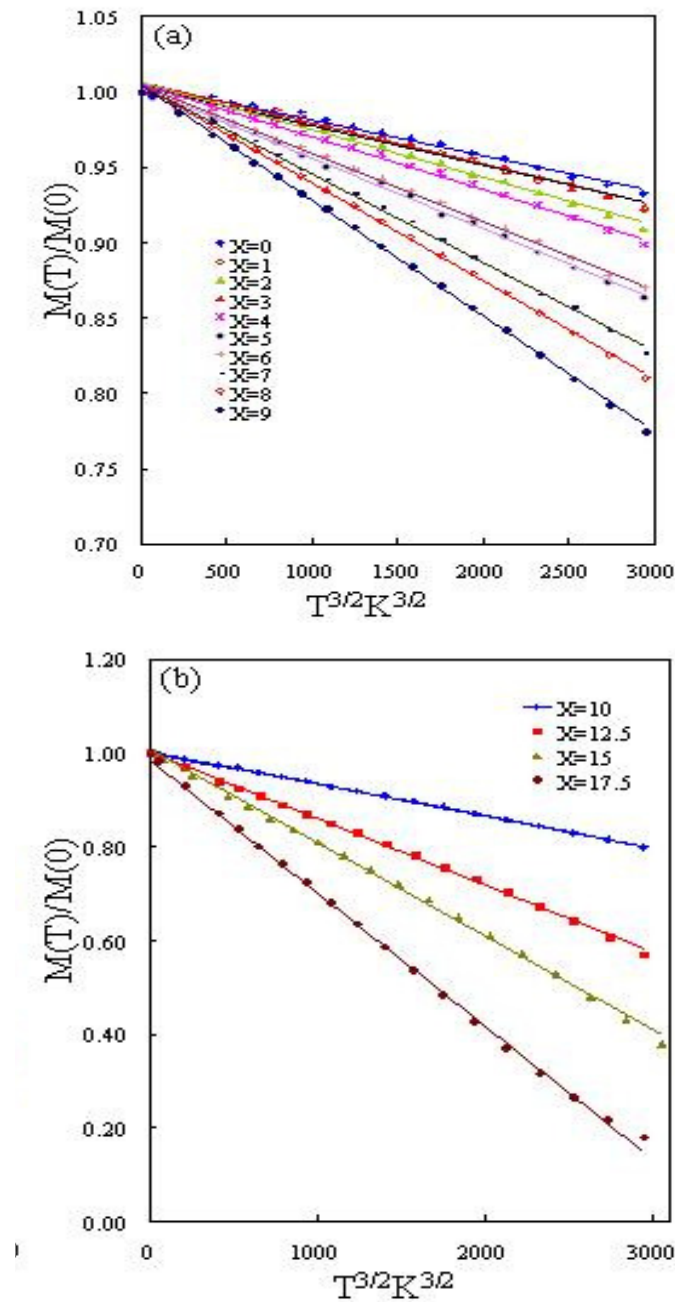


Fig. 5.18 The dependence of reduced magnetization $\frac{M(T)}{M(0)}$ as a function of $T^{\frac{3}{2}}$ of amorphous ribbons with composition $\text{Fe}_{73.5-x}\text{Cr}_x\text{Cu}_1\text{Nb}_3\text{Si}_{13.5}\text{B}_9$ (a) $x = 0, 1, 2, 3, 4, 5, 6, 7, 8$ & 9 and (b) $x = 10, 12.5, 15$ & 17.5 Symbol: Experimental data and full line fitted with the equation (5.8)

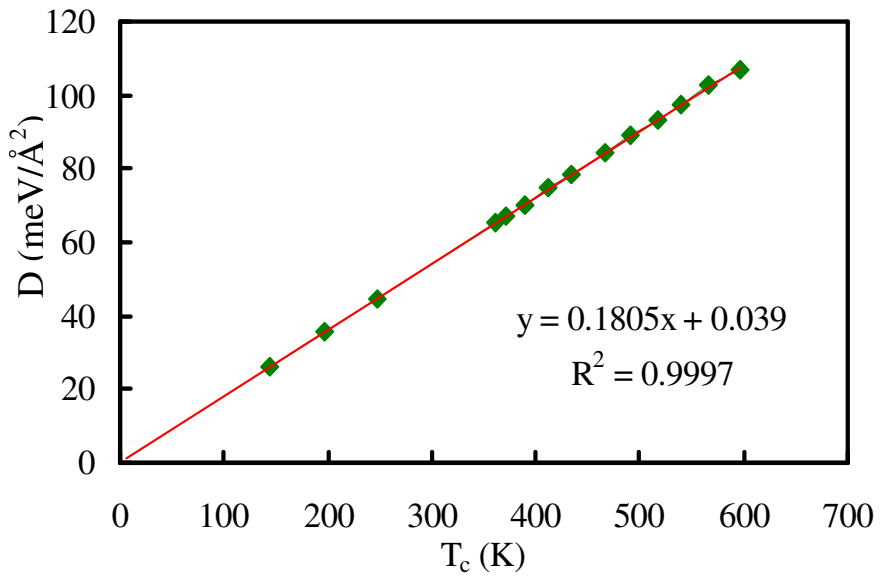
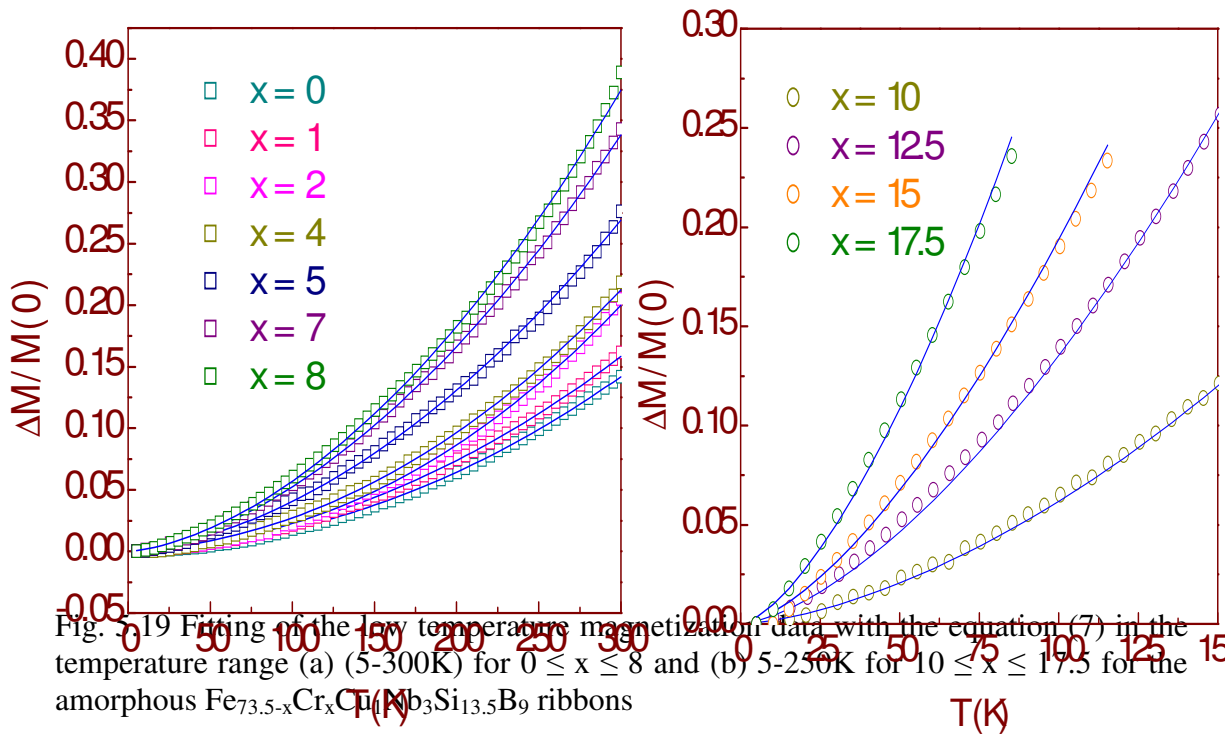


Fig. 5.20 Spin wave stiffness constant (D) as a function of Curie temperature (T_c)

Table-5.3 parameters describing the temperature dependence of magnetization of the amorphous ribbons with composition $\text{Fe}_{73.5-x}\text{Cr}_x\text{Cu}_1\text{Nb}_3\text{Si}_{13.5}\text{B}_9$

Cr content x at. %	B (K ^{-3/2})	C(K ^{-5/2})	C/B (K ⁻¹)	M(O) emu/g at 0 K	D _{SP} meV Å ²	<r ² > Å ²	Temp. range of fitting
0	18.3x10 ⁻⁶	3.85x10 ⁻⁸	2.10x10 ⁻³	160.3	107	27.0	0 < T/T _C < 0.6
1	20.0x10 ⁻⁶	4.10x10 ⁻⁸	2.05x10 ⁻³	155.3	103	25.4	0 < T/T _C < 0.6
2	22.7x10 ⁻⁶	4.62x10 ⁻⁸	2.04x10 ⁻³	147.6	98	24.0	0 < T/T _C < 0.6
3	27.0x10 ⁻⁶	5.02x10 ⁻⁸	1.86x10 ⁻³	133.4	93	21.0	0 < T/T _C < 0.6
4	30.0x10 ⁻⁶	5.50x10 ⁻⁸	1.83x10 ⁻³	127.8	89	20.0	0 < T/T _C < 0.7
5	34.0x10 ⁻⁶	6.00x10 ⁻⁸	1.76x10 ⁻³	122.9	84	18.0	0 < T/T _C < 0.7
6	39.0x10 ⁻⁶	6.30x10 ⁻⁸	1.62x10 ⁻³	119.7	78	15.2	0 < T/T _C < 0.7
7	45.0x10 ⁻⁶	6.25x10 ⁻⁸	1.39x10 ⁻³	111.2	75	12.5	0 < T/T _C < 0.8
8	51.0x10 ⁻⁶	6.80x10 ⁻⁸	1.33x10 ⁻³	107.8	70	11.2	0 < T/T _C < 0.8
9	57.0x10 ⁻⁶	7.32x10 ⁻⁸	1.28x10 ⁻³	103.1	67	10.3	0 < T/T _C < 0.8
10	58.0x10 ⁻⁶	6.80x10 ⁻⁸	1.17x10 ⁻³	92.8	65	9.2	0 < T/T _C < 0.8
12.5	152.0x10 ⁻⁶	15.00x10 ⁻⁸	0.987x10 ⁻³	72.6	44	5.3	0 < T/T _C < 0.8
15	234.0x10 ⁻⁶	6.50x10 ⁻⁸	0.278x10 ⁻³	67.2	35	1.2	0 < T/T _C < 0.6
17.5	480.0x10 ⁻⁶	12.00x10 ⁻⁸	0.250x10 ⁻³	52.8	26	0.8	0 < T/T _C < 0.6
Fe	3.4x10 ⁻⁶	0.10x10 ⁻⁸	0.294x10 ⁻³	220	286	16a ²	-

It is observed that the values of B, C for the studied samples increases gradually as the Cr content is increased. These values are much larger than the crystalline Fe, which is characteristic of amorphous ferromagnet [5.37, 5.38]. The mean-square value of the range of exchange interaction <r²>, decreases gradually with the increase of Cr content having a value of 27 Å² for x = 0 to 0.8 Å² for x = 17.5. These values are much smaller

than that of crystalline ferromagnet. The low value of $\langle r^2 \rangle$ as compared with the Fe indicates that the range of exchange interaction is shorter in the Finemet type of amorphous alloys in comparison with that in crystalline ferromagnets in agreement with the previously published reports [5.36, 5.38]. The values of spin-wave stiffness constant (D) decreases monotonically from 107 meV Å² for x = 0 to 26 meV Å² for the sample x = 17.5. These values are much lower than crystalline Fe, which is 286 meV Å². The smaller values of spin-wave stiffness constant (D) in the studied system is an indication of the softening of the exchange interaction according to Varga *et al.* [5.39]. Our experimental values of D are very typical for amorphous materials and agree reasonably well with the values reported earlier in the literature [5.29, 5.37, 5.38, 5.40 -5.43]. The $\frac{D}{T_c}$ for the amorphous ferromagnets is generally smaller in comparison to the value of 0.27 for crystalline Fe which is indicative of the short-range nature of interactions in our studied system [5.37, 5.39, 5.41]. Our experimental $\frac{D}{T_c} = 0.18$ for the whole series of alloys which corresponds well with the value of $\frac{D}{T_c} = 0.21$ [5.29], 0.18 [5.41] for the amorphous alloys. The reduction in the value of D with the substitution of Fe by Cr may be interpreted as due to an increase in the distance between Fe atoms. This leads to the weakening of exchange interaction between Fe atoms resulting in the lowering of Curie temperature. Fig. 5.20 shows the exchange stiffness constant D, as a function of T_c. A linear dependence of D with T_c is observed for the entire composition range, which passes through the origin. The value of $\frac{D}{T_c} = 0.18$ remains constant (table-5.3) for all the compositions studied which indicates that the range of exchange interaction is not modified when Fe is substituted by Cr.

5.2.7 Variation of Magnetization and Curie temperature with Isothermal Annealing of Higher Cr Content Amorphous Alloys

This is well known that amorphous state is metastable. Metastability of amorphous or glassy metal alloys offers the possibility of phase separation diffusion of various species and structural relaxation even though the alloys remains amorphous when they are annealed at temperature well below the crystallization temperature. All these changes have effect on the intrinsic magnetic properties such as Curie temperature (T_c) saturation magnetization (M_s) and magnetostriction. It has been demonstrated that saturation magnetization, M_s and Curie temperature (T_c) of FINEMET alloys in the amorphous state increase on annealing up to the annealing temperature (T_a) corresponding to the early stage of crystallization, beyond which M_s and T_c both decrease [5.14, 5.16, 5.44].

The FINEMET is ferromagnetic at room temperature. It is observed in the present investigation that the amorphous alloys $Fe_{73.5-x}Cr_xCuNb_3Si_{13.5}B_9$ with $x = 10, 12.5, 15$ & 17.5 , which are paramagnetic (except $x = 10$) at room temperature show an increase of M at room temperature when annealed below the onset of crystallization temperature. Fig. 21 (a, b) and 5.22 (a, b) clearly demonstrates an increase of magnetization upon annealing temperature (T_a) for all these four samples. For sample $x = 17.5$, M increases substantially only at $T_a = 600^\circ C$ which is close to the onset of crystallization temperature $T_{x1} = 620^\circ C$ for this alloy according to DSC data of table-5.1. This increase of M with T_a up to $580^\circ C$ is connected to the structural relaxation and varying degrees of chemical disorder concomitant with the previous published results on typical FINEMET alloy [5.16 - 5.18]. Similar increase in M_s due to structural relaxation has been detected in Fe-based metallic glass [5.44]. With reference to the enhancement of magnetization of annealed samples, DSC thermograms have been taken on samples annealed at $T_a = 520^\circ C, 540^\circ C, 560^\circ C$ along with as cast samples and depicted Fig. 5.23. It is seen in fig 5.23 (a, b, c, d) that the area under the first crystallization event Fe(Si) phase slightly diminishes for $x = 10$ and 12.5 implying that initiation of crystallization seems to take place and accordingly M vs. H curves sharply rises and looks like ferromagnetic for $x = 12.5$ which is paramagnetic in the amorphous condition with $T_c = 247$ K. This increase of magnetization for the sample $x = 12.5$ is due to the evolution of ferromagnetic Fe(Si) crystallites. This has also been confirmed by X-ray

diffraction pattern as shown in fig. 5.4 (d) with the appearance of Fe. Note that $x = 10$ is ferromagnetic at room temperature. For $x = 15$ up to $T_a = 560^\circ\text{C}$, M increases only due to structural relaxation, while for $x = 17.5$ at $T_a = 600^\circ\text{C}$ a sharp rise of M correspond to initiation of crystallization of Fe(Si) phase and has been detected in XRD pattern shown in fig. 5.4 (f). The influence of partial substitution of Fe by Cr on the soft magnetic properties of $\text{Fe}_{73.5-x}\text{Cr}_x\text{Cu}_1\text{Nb}_3\text{Si}_{13.5}\text{B}_9$ ($x = 1, 2, 3, 4 \& 5$) have been studied through the measurement of magnetic hysteresis loops of amorphous and annealed samples at room temperature. Fig 24 (a, b, c, d) shows low field (≈ 1.5 Oe) hysteresis loop for the samples $x = 1, 3, 4, 5$. It is clearly observed that the as cast amorphous samples have low magnetic induction B_{max} value for all the samples which increases substantially on annealing at 540°C for 30 min. This annealing temperature is close to the onset of crystallization temperature.

Therefore an increase in magnetization M at room temperature is expected on annealed samples according to ref. [5.14, 5.16, 5.18, 5.45]. With the increase of magnetic induction on annealing, a subsequent decrease of coercive force (H_c) is noticed for all the samples implying magnetic softening of these alloys upon annealing. Amorphous alloys clearly show rectangular shaped hysteresis loops, the origin of which may be related to the magnetoelastic anisotropy contribution as a result of stress induced during rapid quenching process. But after annealing the shape of the hysteresis loops changes to normal form with the manifestation of enhanced soft magnetic properties i.e. high magnetic induction and low coercivity. Table-5.4 shows the value of B_{max} and H_c for the samples annealed at 540°C for 30 min and as cast condition. The data shows that H_c decreases substantially on annealing and the maximum magnetic induction B_{max} , at $H \approx 1.5$ Oe also increases rapidly for all the annealed samples as compared with the amorphous precursor. Similar low field hysteresis behavior has been observed in Cr substituted FINEMET with Au instead of Cu [5.46]. The observed improvement of soft magnetic characteristic of the annealed samples at $T_a = 540^\circ\text{C}$ for 30 min is likely due to the formation of α -Fe(Si) phase with optimum nanometric grains, their appropriate volume fraction and strong exchange coupling among them.

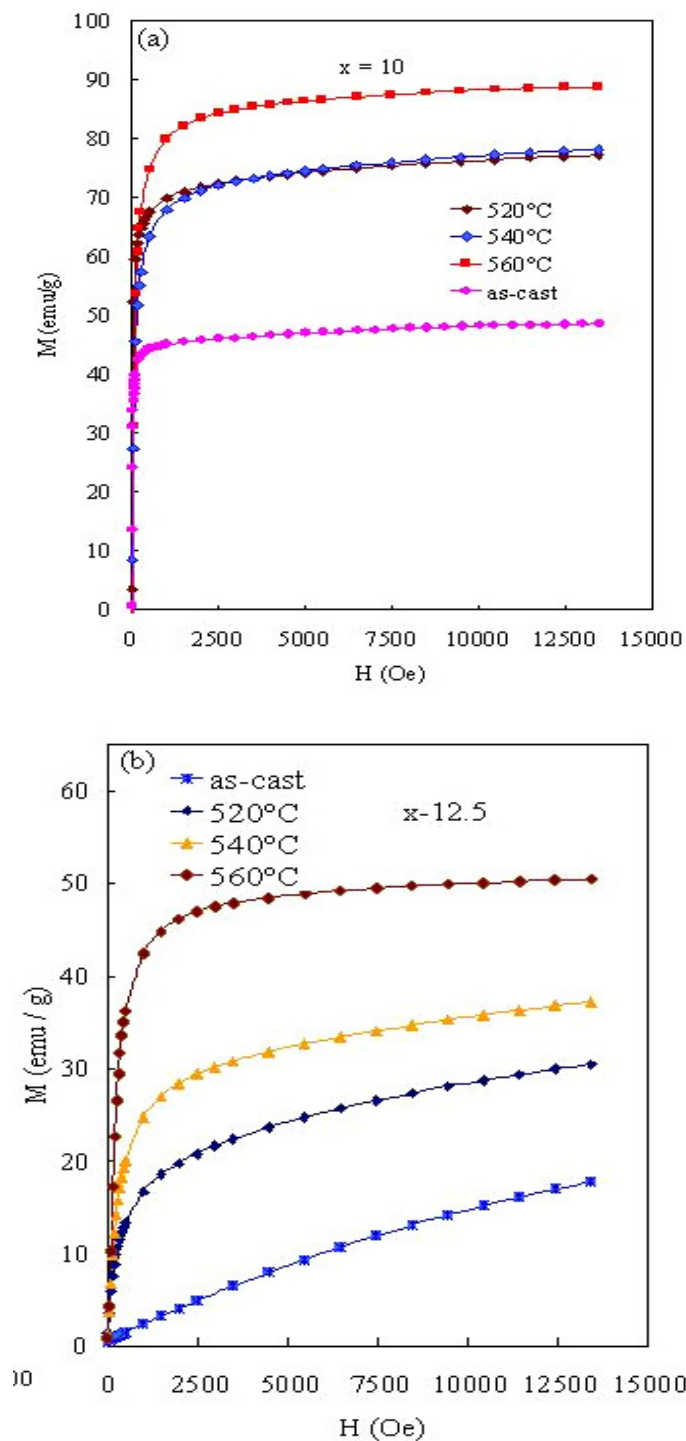


Fig. 5.21 field dependence of magnetization curves of ribbons $\text{Fe}_{73.5-x}\text{Cr}_x\text{Cu}_1\text{Nb}_3\text{Si}_{13.5}\text{B}_9$ with (a) $x = 10$ (b) $x = 12.5$ in the ascast and annealed at different frequencies

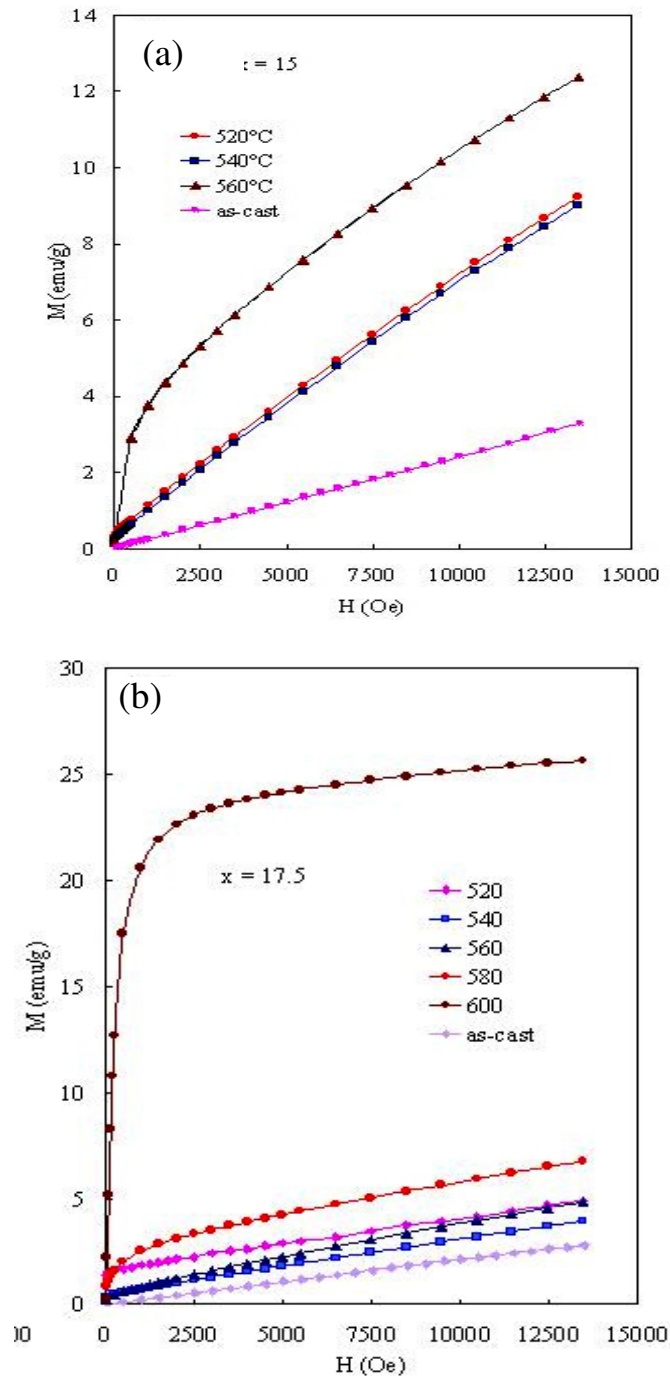


Fig. 5.22 Field dependence of magnetization curves of ribbons $\text{Fe}_{73.5x}\text{Cr}_x\text{Cu}_1\text{Nb}_3\text{Si}_{13.5}\text{B}_9$ with (a) $x = 15$ (b) $x = 17.5$ in the as cast and annealed at different temperatures

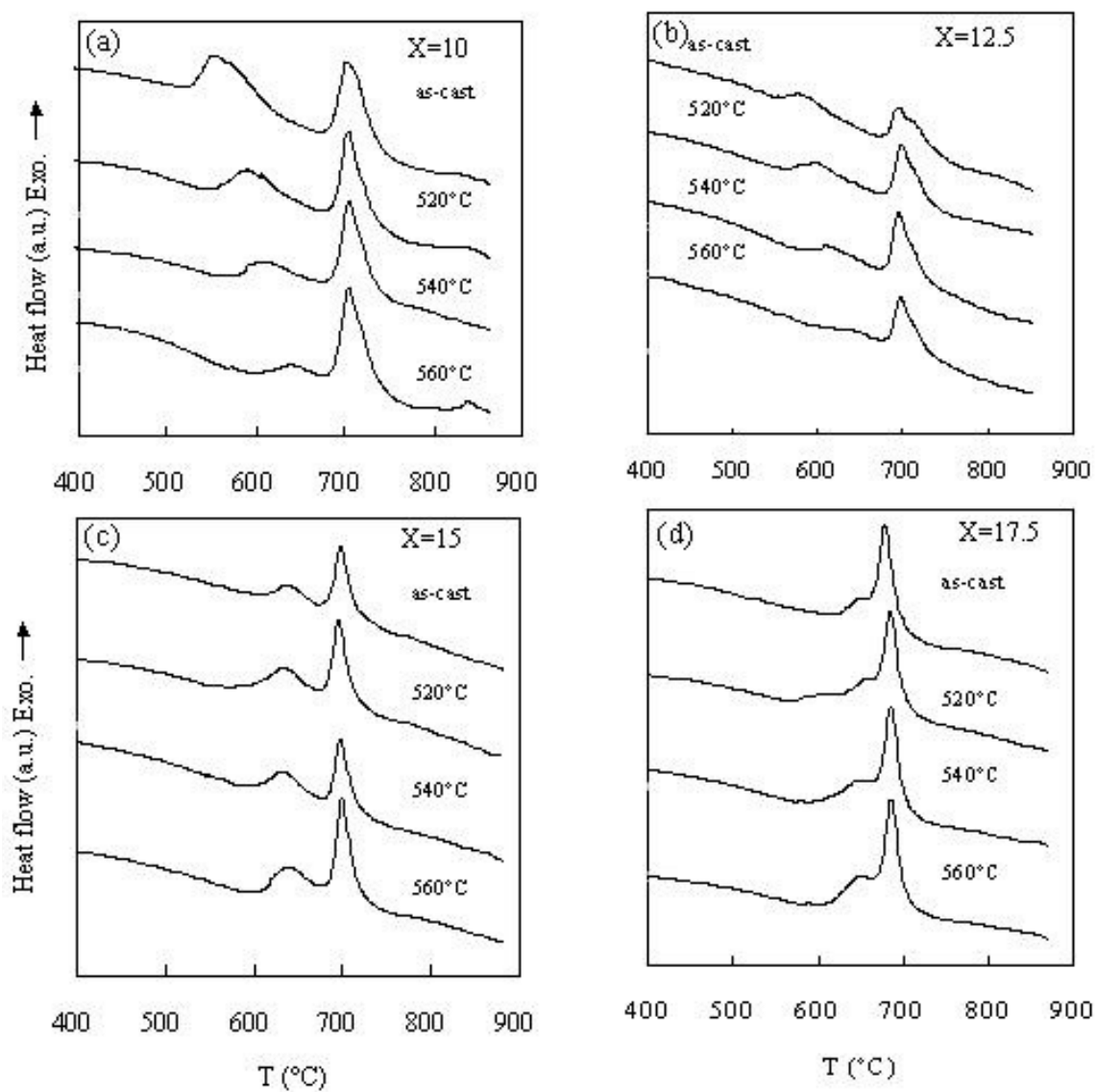


Fig. 5.23 DSC curves of the ribbons with composition $\text{Fe}_{73.5-x}\text{Cr}_x\text{Cu}_1\text{Nb}_3\text{Si}_{13.5}\text{B}_9$ (a) $x = 10$ (b) $x = 12.5$ (c) $x = 15$ (d) $x = 17.5$ in the as cast and annealed at different temperatures

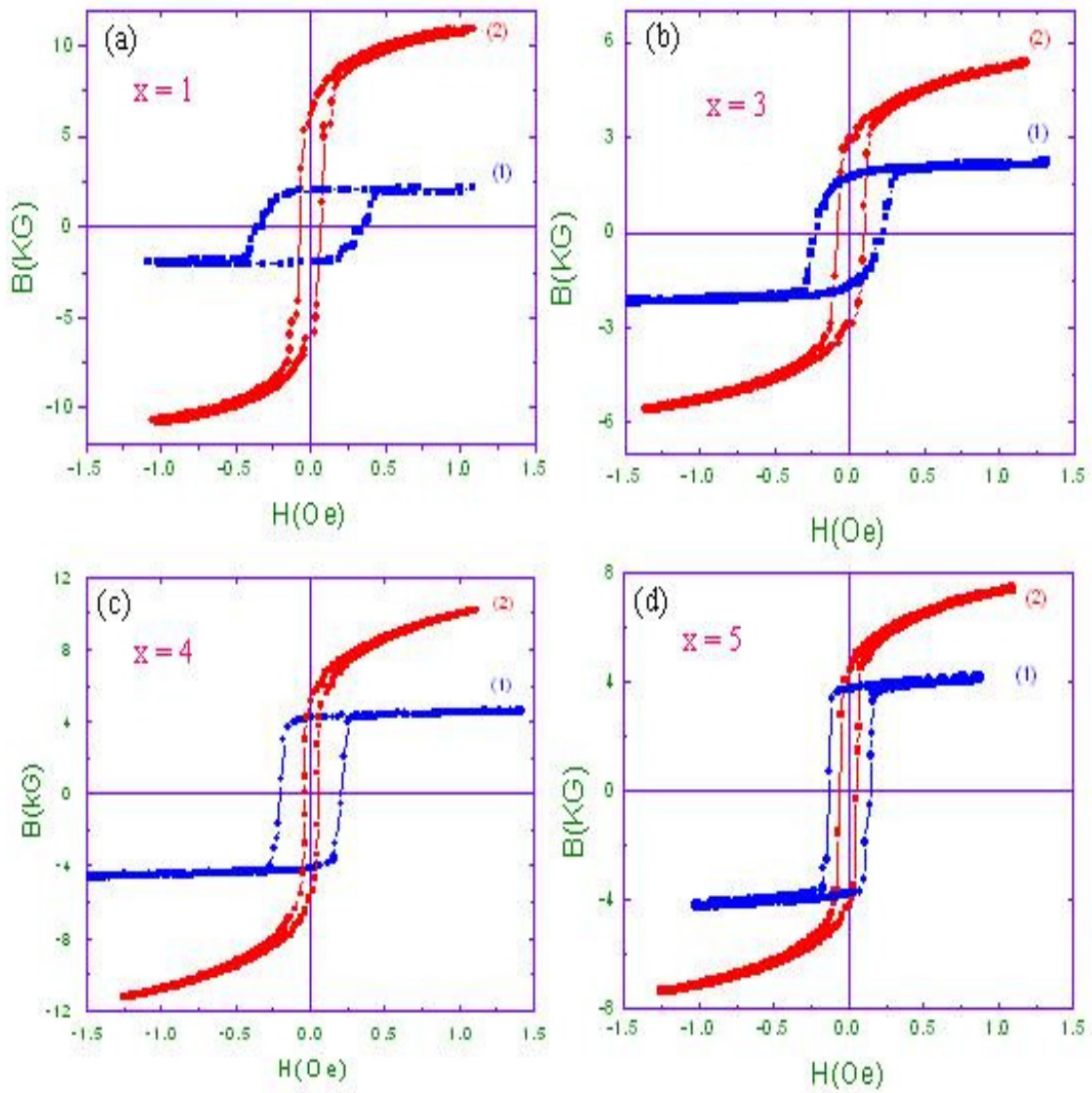


Fig. 5.24 Hysteresis loops of amorphous ribbon with composition $\text{Fe}_{73.5-x}\text{Cr}_x\text{Cu}_1\text{Nb}_3\text{Si}_{13.5}\text{B}_9$ ribbons with $x = 1, 3, 4$ & 5 in the as-cast (curve 1) and annealed (curve 2) at 540°C for 30 min.

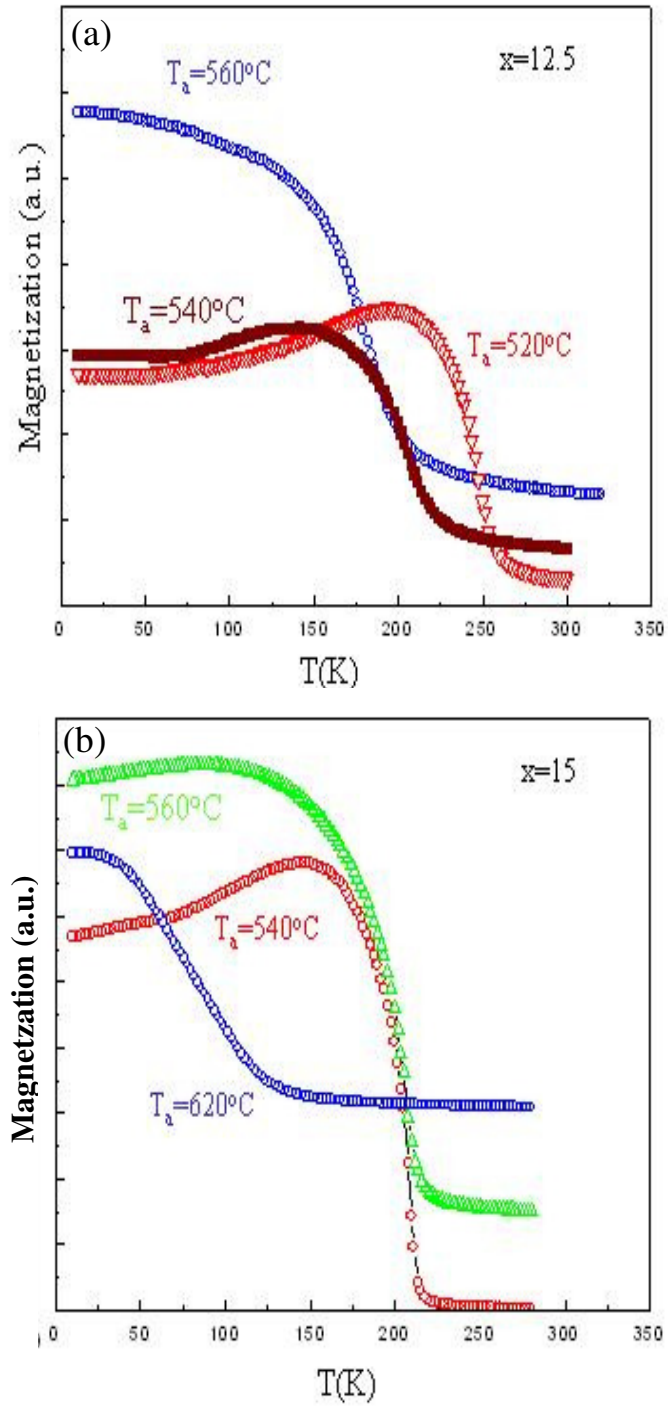


Fig. 5.25 Dependence of Curie temperature on annealing temperature of the amorphous ribbons with composition (a) $\text{Fe}_{61}\text{Cr}_{12.5}\text{Cu}_1\text{Nb}_3\text{Si}_{13.5}\text{B}_9$ (b) $\text{Fe}_{58.5}\text{Cr}_{15}\text{Cu}_1\text{Nb}_3\text{Si}_{13.5}\text{B}_9$

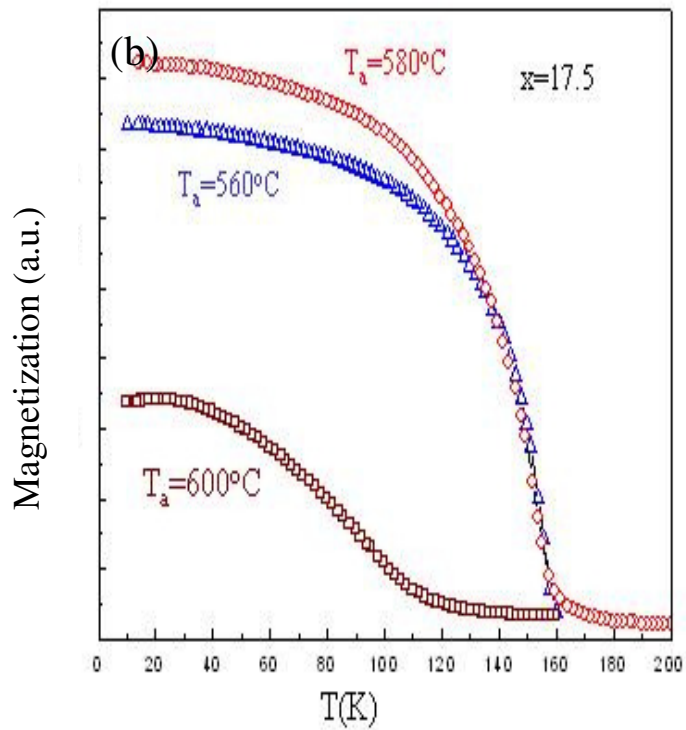
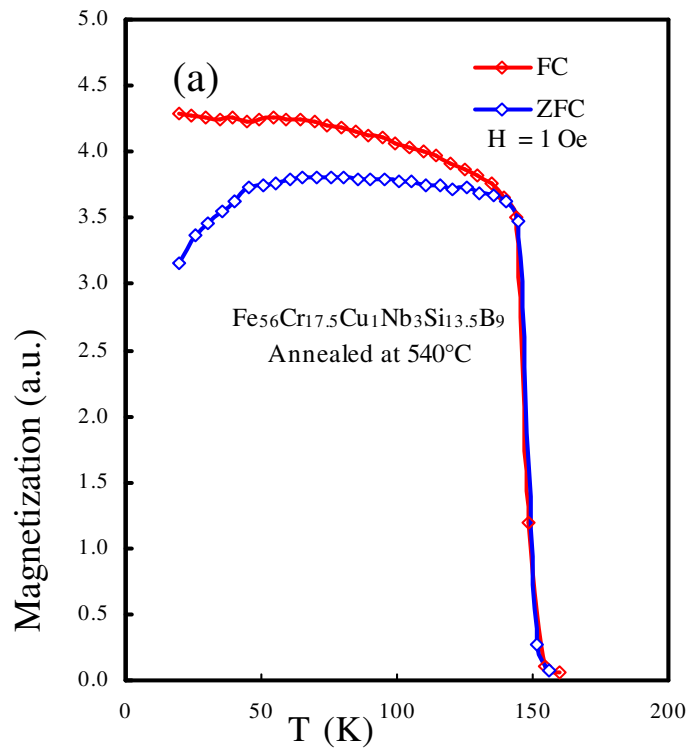


Fig. 5.26 (a) FC and ZFC magnetization curve with an applied field 10e and (b) dependence of Curie temperature on annealing temperature with composition $\text{Fe}_{56}\text{Cr}_{17.5}\text{Cu}_1\text{Nb}_3\text{Si}_{13.5}\text{B}_9$

Table-5.4 Maximum magnetic induction B_{\max} and coercivity H_c for the as cast and annealed samples measured at $H = 1$ Oe of the amorphous ribbon with composition $Fe_{73.5-x}Cr_xCu_1Nb_3Si_{13.5}B_9$ alloys

Cr content x at. %	As Cast		Annealed at 540°C for 30 min	
	B_{\max} (KG)	H_c (Oe)	B_{\max} (KG)	H_c (Oe)
1	2.0	0.35	10.8	0.069
3	2.3	0.23	5.8	0.080
4	4.5	0.20	10.2	0.054
5	4.2	0.14	7.7	0.057

Table-5.5 Effect of annealing on the Curie temperature of the amorphous ribbon with composition $Fe_{73.5-x}Cr_xCu_1Nb_3Si_{13.5}B_9$ ($x = 12.5, 15$ & 17.5)

Cr content x at. %	Annealed condition	Curie temperature, T_c (K)
12.5	As-cast	247
	520 ⁰ C (30 min)	250
	540 ⁰ C (30 min)	≈ 198
	560 ⁰ C (30 min)	≈ 180
15	As-cast	196
	540 ⁰ C (30 min)	204
	560 ⁰ C (30 min)	208
	620 ⁰ C (30 min)	≈ 102
17.5	As-cast	143.5
	540 ⁰ C (30 min)	147
	560 ⁰ C (30 min)	152
	580 ⁰ C (30 min)	150
	600 ⁰ C (30 min)	≈ 92

It has been well understood from our discussions above that Curie temperature (T_c) of FINEMET alloys in the amorphous state changes with the annealing temperature (T_a) dependent on the state of crystallization. In the forthcoming discussion it will be demonstrated how the Curie temperatures of higher Cr content alloys, $Fe_{73.5-x}Cr_xCuNb_3Si_{13.5}B_9$ with $x = 12.5, 15$ & 17.5 are affected on annealing temperature T_a . The Curie temperatures of these alloys are below room temperature. The samples were annealed between between $520^{\circ}C$ and $620^{\circ}C$. Fig. 5.25 (a, b) and 5.26 (b) shows the low field (10 Oe) dc magnetization of annealed samples with $x = 12.5, 15$ & 17.5 as a function of temperature from 10 K to above the Curie temperature of individual samples. While fig. 5.26 (a) demonstrates the Field-cooled (FC) and Zero Field-cooled (ZFC) magnetization of sample $x = 17.5$ annealed at $540^{\circ}C$. The Curie temperature of the sample $x = 12.5$ in the amorphous state is $T_c = 247$ K which increases to 250 K when annealed at $520^{\circ}C$ for 30 minutes. However, annealing at higher temperature i.e. $T_a = 540^{\circ}C$ and $560^{\circ}C$ for 30 minutes, T_c decreases to 198 K and 180 K respectively. For the sample $x = 15$, T_c increases from 196 K in the as-cast state to a maximum value of $T_c = 208$ K corresponding to annealing at $T_a = 560^{\circ}C$ (30 min) which again decreases to $T_c \approx 102$ K at $T_a = 620^{\circ}C$ (30 min). The T_c of the sample $x = 17.5$ increases from 143.5 K in the as-cast state to a maximum value of $T_c = 152$ K at $T_a = 560^{\circ}C$ (30 min) and thereafter to $T_c = 92$ K for annealing at $T_a = 600^{\circ}C$. From the measurement of ZFC/FC magnetization with $H = 1$ Oe shown in fig. 26 (a), Curie temperature $T_c = 147$ K has been revealed for the sample $x = 17.5$ when annealing has been performed for 30 minutes at $T_a = 540^{\circ}C$. This value of T_c is slightly higher than that of the amorphous counterpart. The variation of T_c of the amorphous precursors with annealing temperature T_a is demonstrated in table-5.5. From the measurement it is clear that the effect of annealing on the T_c of higher Cr content in the FINEMET alloys behave similarly as found in the Finemet composition reported by previous investigators [5.2, 5.14, 5.16, 5.45]. The increase of T_c during the annealing of the amorphous precursor at a temperature well below the initiation of crystallization temperature is caused by the irreversible relaxation of microstructural quantities like long-range internal stress, topological and chemical short-range order.

All these microstructural effects bring about a change in the interatomic distances which affect directly the strength of the exchange interaction resulting in a change of Curie temperature, T_c . Blachowicz *et al.* [5.47] found from the analysis of the Mossbauer spectra for the quenched and annealed samples of $\text{Fe}_{74}\text{Cu}_1\text{Nb}_3\text{Si}_{12}\text{B}_{10}$ below T_{x1} (at 400°C) that the packing density of atoms has been increased in the case of annealed samples as compared with the amorphous one. The authors observed the enhancement of T_c dependent on annealing temperature as well as time. It is observed from the present investigation that the fall of magnetization at $T=T_c$ is reasonably sharp when annealed at lower temperature and in particular when magnetization is measured with very low field as shown in fig. 5.26 (a). The annealing temperature (T_a) corresponding to which enhancement of T_c takes place for the samples $x = 12.5, 15, 17.5$, no XRD peaks related crystallization have been detected in our experiments (see Fig. 5.4 (d, e, f) which again confirms that the enhancement of T_c^{am} of the amorphous precursor is connected with the structural relaxation. With the increase of T_a close to onset of crystallization temperature and above Curie temperature (T_c) decreases for all the samples in agreement with the previous published reports. The reason for the decrease of T_c of the amorphous phase with annealing at higher temperature, i.e. around T_{x1} and above is probably connected with the depletion of Fe and subsequent increase of Nb and Cr in the amorphous $(\text{Fe-Nb-Cr})_2\text{B}$ matrix. This causes a weaker exchange interaction among the Fe magnetic moments resulting in a decrease of Curie temperature.

This happens because with the increase in annealing temperature results mainly in an increase of the volume fraction of $\alpha\text{-Fe}(\text{Si})$ crystallites. This is worthwhile to note that the decrease of magnetization with temperature for the samples annealed at higher T_a is relatively smeared out as shown in fig.5.25 (a, b) and 5.26 (b). It is very difficult to find out an unique value of T_c from such diffused M vs. T measurements. The more diffuse character of the ferro-paramagnetic transition in the residual amorphous matrix for the samples annealed at higher temperature is attributed to the higher degree of compositional and structural disorder in the residual amorphous phase [5.48, 5.49]. Varga *et al.* [5.50] have interpreted this type of reduction of T_c in FINEMET alloys

after annealing at higher temperature as due to compositional gradients within the remaining amorphous phase. Within the inhomogeneous amorphous phase there is basically no longer a unique Curie temperature, but a distribution of T_c . As a consequence instead of a single $M(T)$ curve, the combination of a family of curves with distribution of Curie temperature is obtained. Therefore the T_c values mentioned in the present study related to the samples annealed at relatively high temperatures should be taken with cautious. However, the decrease of T_c shown in the table-5.5 is a general trend of the alloys under investigation since $\frac{dM}{dT}$ has been taken to estimate the T_c from these measurements.

5.3 Permeability Measurements on Amorphous and Annealed Samples of $\text{Fe}_{73.5-x}\text{Cr}_x\text{Cu}_1\text{Nb}_3\text{Si}_{13.5}\text{B}_9$ Alloys

Permeability and coercivity are the most important parameters for the evaluation of soft magnetic materials. The criteria for the softest magnetic materials demand very high permeability and / or extremely low coercivity and these properties necessitate the anisotropy energy and the magnetoelastic energy tend towards zero. These unique demands are fulfilled when the FINEMET type of nanocrystalline materials are thermally treated around their primary crystallization temperature which facilitates the evolution of nanometric size of the Fe(Si) grains (10-12 nm) that are exchanged couple through the remaining thin residual amorphous interface.

In order to correlate the microstructural features with soft magnetic properties of the alloys under study, initial permeability of the toroidal shaped samples annealed at different temperatures are measured at room temperature with an applied ac field of 10^{-3} Oe.

Fig 5.27 (a, b) shows the variation of initial permeability as a function of frequency from 1kHz-500kHz for the samples $\text{Fe}_{73.5-x}\text{Cr}_x\text{Cu}_1\text{Nb}_3\text{Si}_{13.5}\text{B}_9$ with $x = 1$ & 3 in the as cast and annealed at various temperatures up to 625°C . The magnetic properties of the soft magnetic materials are mainly determined by the domain wall mobility especially in the range of reversible magnetization. It is observed that μ' increases with the increase of annealing temperature T_a for both the sample $x = 1$ & 3 attaining a maximum value of μ' at $T_a = 545$ and 565°C respectively, when T_a is increased beyond these temperatures, μ' rapidly decrease to a very low value as indicated by both the samples. It is also observed that μ' decrease slowly with the increase of frequency initially and then decrease rapidly due to the increase of loss component μ'' attains its' maximum value at a certain frequency at which μ' falls to half of its value at $f = 1\text{kHz}$ (not shown in fig.5.27 (a, b) for clarity). With the increase of annealing temperature, T_a , μ' increase rapidly in the low frequency region and also falls faster with simultaneous shift of the maxima of μ'' forwards lower frequency side. These effects are the typical

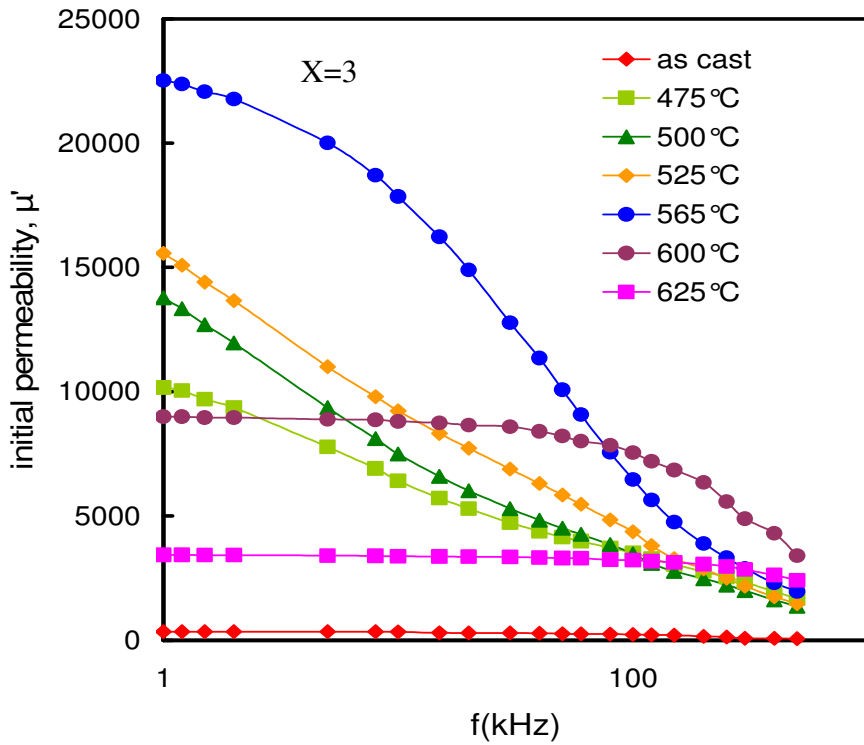
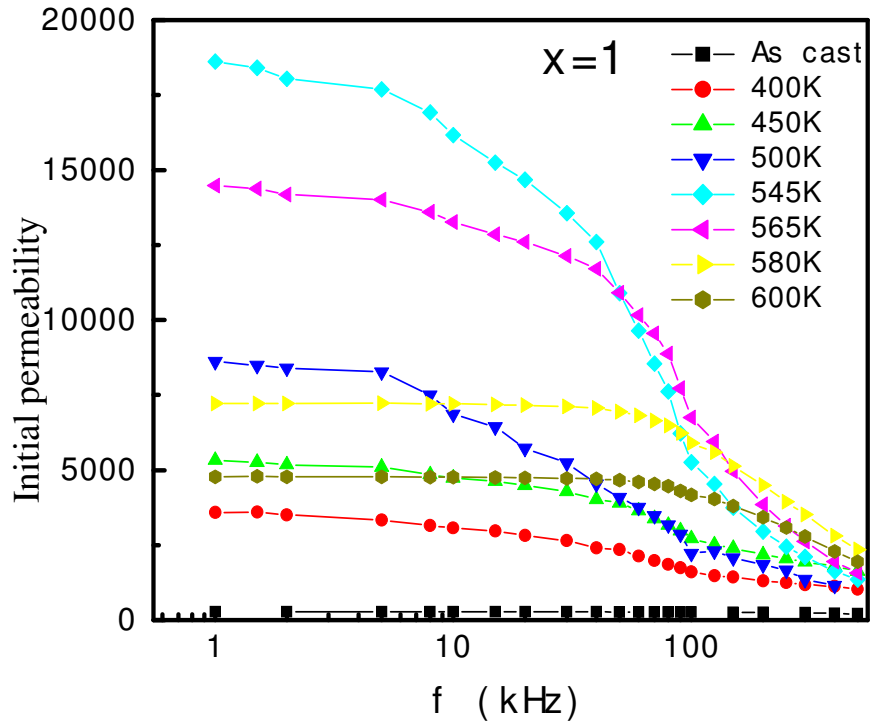


Fig. 5.27 Variation of initial permeability with frequency of the amorphous ribbon with composition $Fe_{56}Cr_{17.5}Cu_1Nb_3Si_{13.5}B_9$ with $x = 1$ and $x = 3$ alloys

features of domain wall relaxation dispersion. This signifies that the high permeability nanocrystalline materials are suitable for low frequency applications. All other samples show the similar frequency characteristics. The results show that the initial permeability of the amorphous sample has been enhanced by two order of magnitude at low frequency when appropriately annealed.

The values initial permeability and the relative loss factor as function of T_a measured at 1 kHz are collected and shown in fig. 5.28 (a, b), 5.29 (a, b), and 5.30 (a, b) for the samples with composition $Fe_{73.5-x}Cr_xCu_1Nb_3Si_{13.5}B_9$ where $x = 1, 2, 3, 4, 5$ & 8. A remarkable dependence of initial permeability and the relative loss factor on T_a is observed. For all the studied samples the initial permeability increases up to a certain annealing temperature attaining a maximum value and thereafter sharply decreases to a very low value. The temperature of annealing corresponding to the maximum value of the permeability may be considered as the optimum annealing temperature for the evolution of the appropriate size of nano grains and their volume fractions. The increase of permeability up to the annealing temperature, $T_a=325^{\circ}C$ is comparatively small and may be attributed to irreversible structural relaxation of the amorphous state. While the annealing temperature exceeds $325^{\circ}C$ a sharp increase of initial permeability takes place, which is associated with the nanocrystallization of α -Fe(Si) phase. These nanograins are strongly coupled via exchange interaction with the increase of volume fraction of α -Fe(Si) nano grains as the annealing temperature increases resulting in a sharp reduction of average anisotropy energy. As a consequence steep increase of initial permeability is manifested. An enhancement of initial permeability by two orders of magnitude compared with its amorphous precursors is observed for the sample annealed at optimum annealing temperature. A drastic decrease of permeability above the optimum temperature for all the samples is evidenced which is associated with the evolution of Fe-B phase. This detrimental boride phase increases the magnetocrystalline anisotropy, which reduces the exchange correlation length weakening the magnetic coupling between the Fe(Si) nanograins resulting in magnetic hardening. It is clearly evidenced from the curves are shown in fig. 5.28 (a, b), fig. 5.29 (a, b) and fig. 5.30 (a, b) that the relative loss factor decreases with T_a attaining a minimum value at a

particular temperature of annealing at which μ' attains its maximum value. This is really what is required for soft magnetic materials from its application point of view i.e. high permeability and simultaneous low losses.

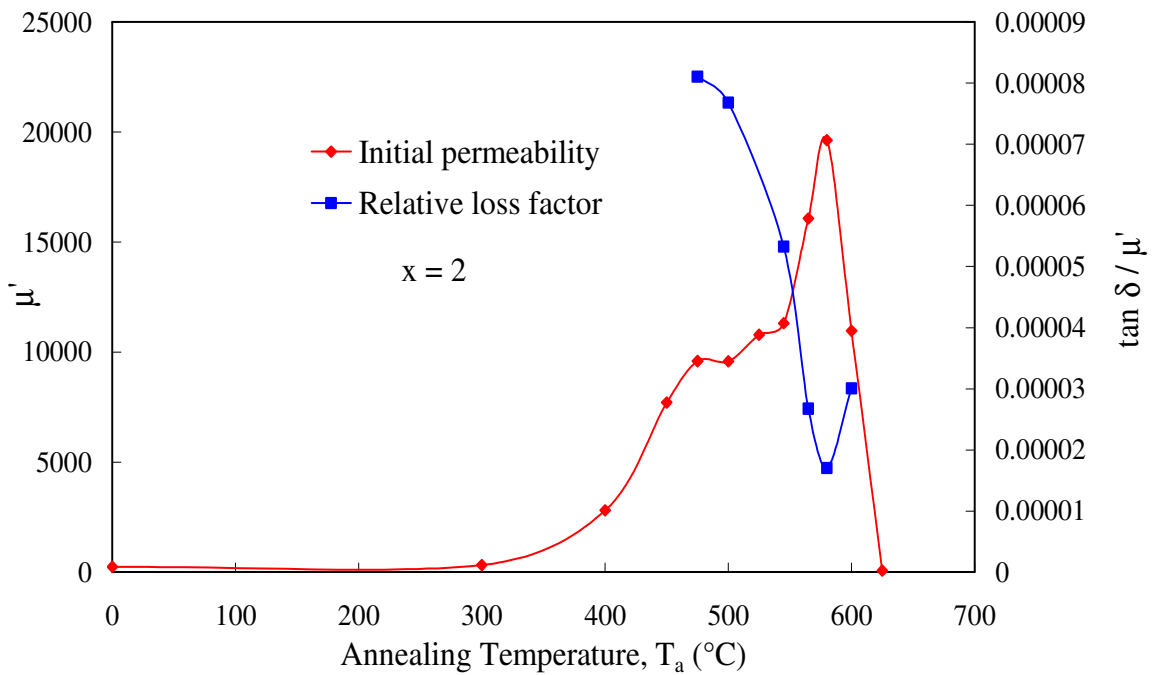
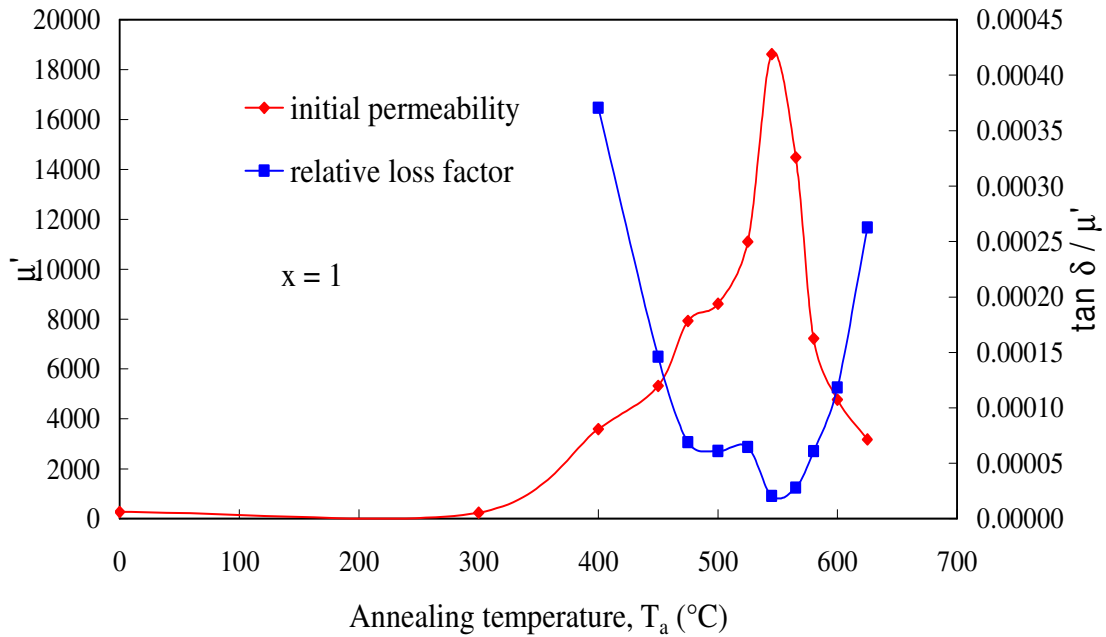


Fig. 5.28 (a, b) Annealing temperature (T_a) dependence of initial permeability (μ') and relative loss factor, $\tan \delta / \mu'$ for samples of $\text{Fe}_{73.5-x}\text{Cr}_x\text{Cu}_1\text{Nb}_3\text{Si}_{13.5}\text{B}_9$ with (a) $x = 1$ (b) $x = 2$

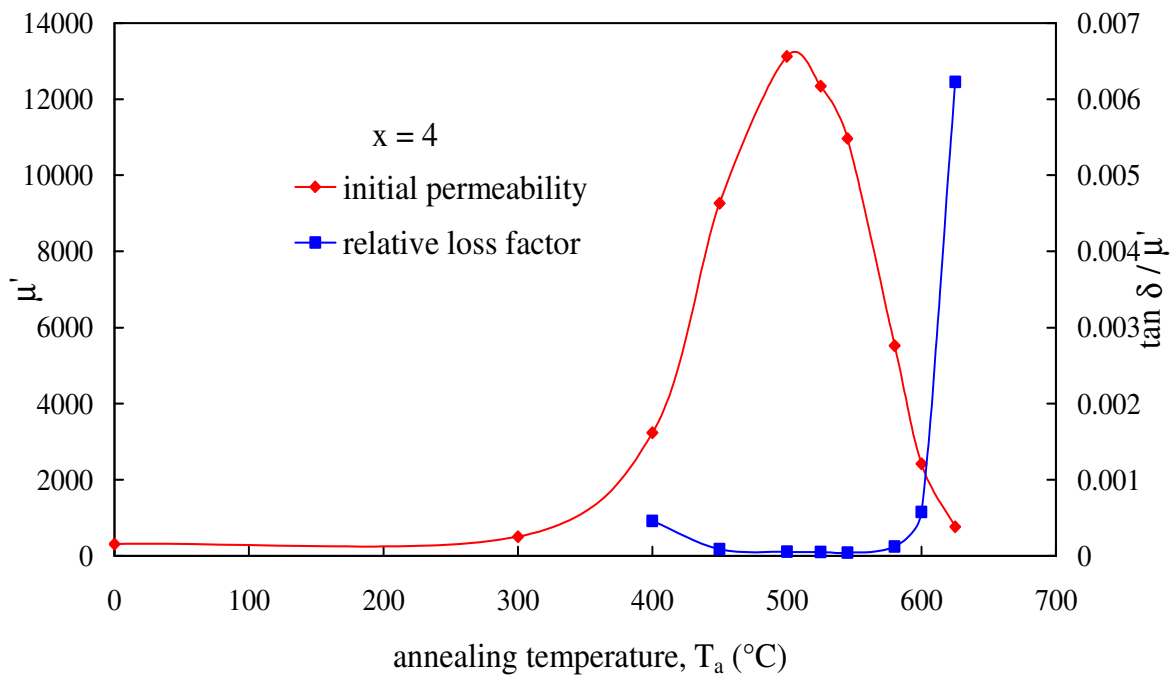
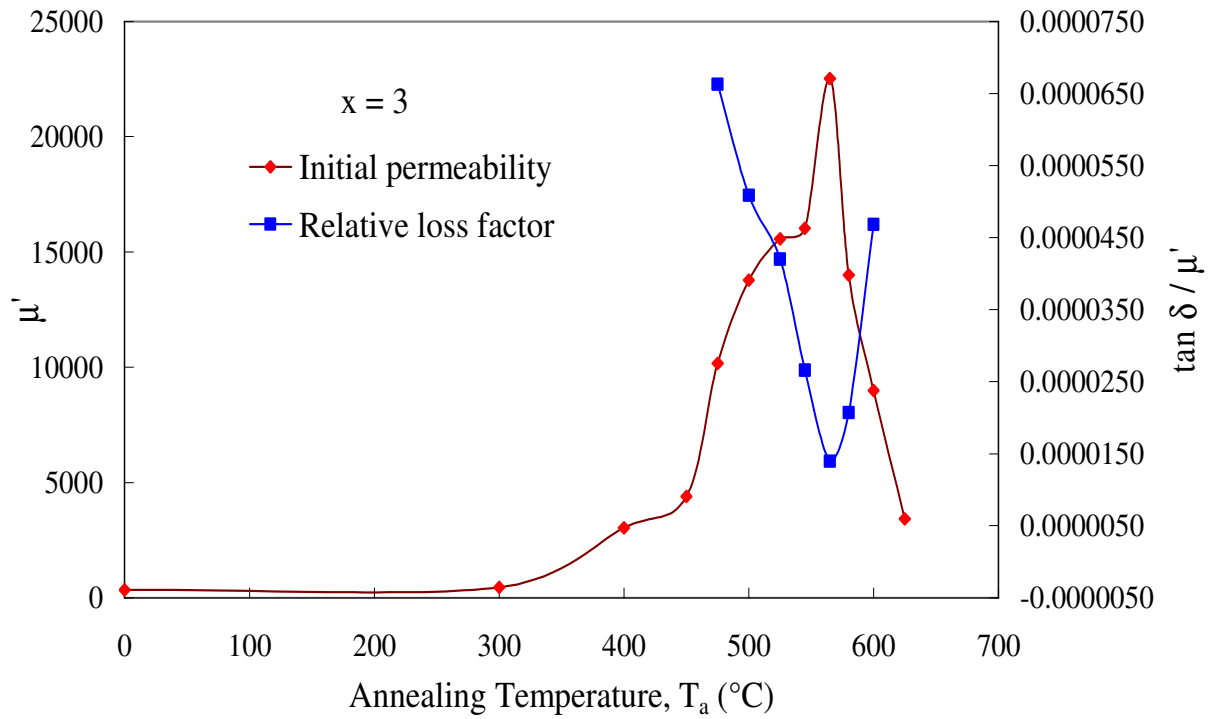


Fig. 5.29 (a, b) Annealing temperature (T_a) dependence of initial permeability (μ') and relative loss factor $\frac{\tan \delta}{\mu'}$ for samples of $\text{Fe}_{73.5-x}\text{Cr}_x\text{Cu}_1\text{Nb}_3\text{Si}_{13.5}\text{B}_9$ with (a) $x = 3$ (b) $x = 4$

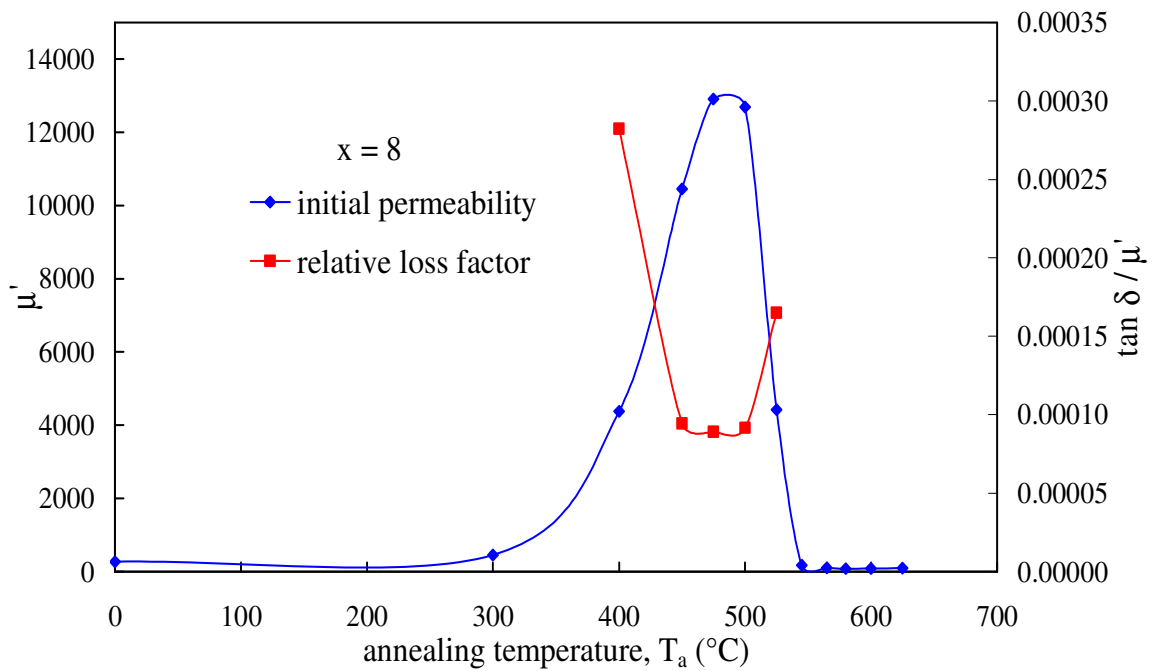
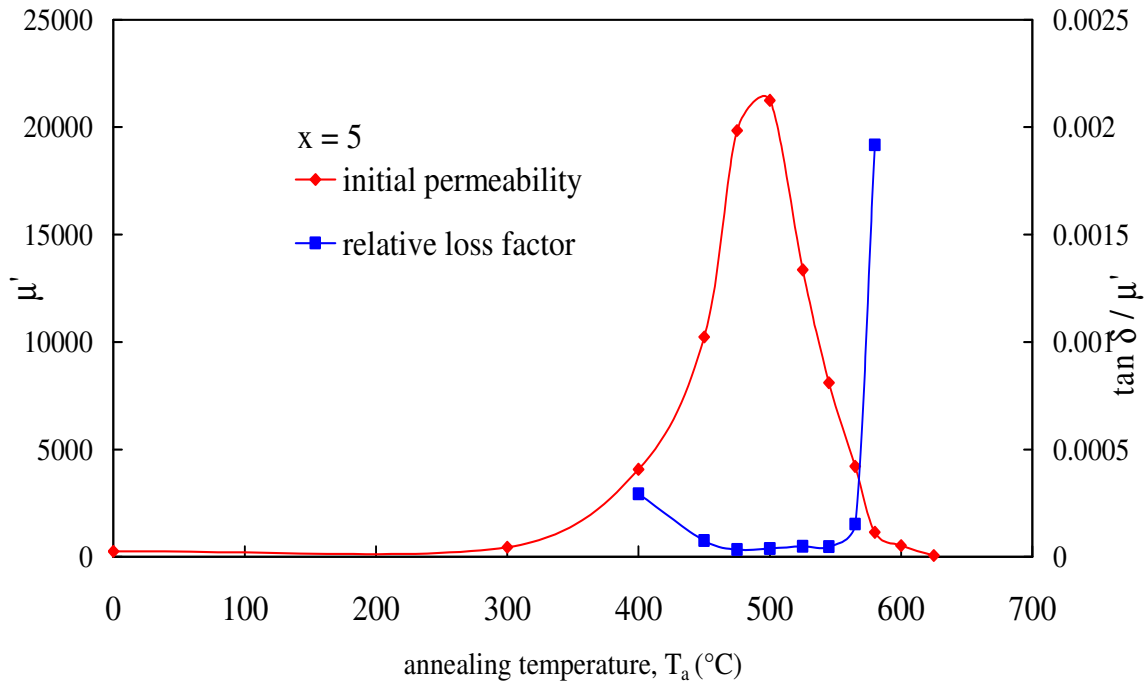


Fig. 5.30 (a, b) Annealing temperature (T_a) dependence of initial permeability (μ') and relative loss factor $\frac{\tan \delta}{\mu'}$ for samples of $\text{Fe}_{73.5-x}\text{Cr}_x\text{Cu}_1\text{Nb}_3\text{Si}_{13.5}\text{B}_9$ with (a) $x = 5$ (b) $x = 8$

Conclusions

A series of amorphous ribbons with the nominal composition $\text{Fe}_{73.5-x}\text{Cr}_x\text{Cu}_1\text{Nb}_3\text{Si}_{13.5}\text{B}_9$ ($x = 0, 1, 2, 3, 4, 5, 6, 7, 8, 9, 10, 12.5, 15 \text{ \& } 17.5$) were prepared by melt-spinning technique and heat treated at various temperatures; below and above the crystallization temperatures. The crystallization behaviour of the samples was investigated by DSC. The amorphous and annealed samples were examined by X-ray diffractometer. Magnetization measurement as a function of temperature and field were performed by SQUID magnetometer, VSM, Permagraph and LCR meter. From the systematic investigation on the crystallization, structural and magnetic properties of the present system the following conclusions can be outlined.

From the DSC thermogram with continuous heating, two well-defined exothermic peaks corresponding to different crystallization products have been revealed. From the thermogram, the onset and peak temperature corresponding to primary and secondary crystallization phenomena have been estimated. The primary crystallization temperature depends sensitively on Cr concentration which shifts to high temperature as the Cr concentration is increased. However, for higher Cr content alloys, the two crystallization temperatures are almost merged with each other since the secondary crystallization temperature of higher Cr content alloys are hardly affected by Cr content. The activation energy of crystallization has been determined from the heating rate dependence of DSC thermogram using Kissinger method, which slightly increases with Cr content. From these experimental findings, it can be concluded that substitution of Fe by Cr enhances the thermal stability of the amorphous alloys against crystallization. The knowledge of the crystallization temperatures is important to determine the appropriate annealing temperature for nanocrystallization, which finally controls the magnetic properties of the Finemet type of alloys.

X-ray diffraction confirmed the amorphous state of all the as prepared ribbons. The evolution of primary phase on annealed samples has been confirmed as bcc-Fe(Si) from XRD pattern. The temperature corresponding to the onset of crystallization obtained from

the XRD pattern is slightly lower than that of DSC data. The reason might be the two different methods of measurements. X-ray diffraction (XRD) measurement has been carried out on isothermal annealed samples while that of DSC on anisothermal. The grain size calculated from the line broadening of X-ray peak is found to decrease from 9 nm for $x = 1$ to 6.5 nm for $x = 5$ when annealed at 540°C for 30 minutes. The higher Cr content alloys do not show any sign of crystallization in their XRD pattern even at an annealing temperature of 580°C for 30 min. This is quite reasonable since their crystallization onset temperature is 600°C and higher.

Magnetic moment μ in Bohr magneton of the amorphous alloys calculated from the saturation magnetization data at 5 K is found to decrease linearly with the increase of Cr concentration throughout the whole concentration range having a value of 1.41 μ_B and 0.45 μ_B for $x = 0$ and $x = 17.5$ respectively. From the least-square fitting of the magnetization as a function of Cr concentration, a decrease of magnetic moment of 0.055 μ_B for each atomic percent of Cr substitution has been determined.

The Curie temperatures of all the amorphous alloys have been determined by various methods like temperature dependence of low and high field dc magnetization, temperature dependence of permeability, ac susceptibility and Arrott plots from magnetic isotherm around T_c . The determined Curie temperatures by various methods are in good agreement within ± 2 K. The Curie temperature of the sample $x = 0$ has been determined to be $T_c = 596$ K which decreases to $T_c = 143.5$ K for $x = 17.5$. A least-square fitting of the experimentally determined T_c values against Cr concentration shows a linear dependence, which decreases 26°C per atomic percentage of Cr substitution. The critical concentration for the onset of ferromagnetism in this alloy system has been estimated to be $x_c = 24 \pm 1$ at.% Cr by linear extrapolation of magnetic moment $n_B = 0$ and $T_c = 0$ as a function of Cr concentration.

The field-cooled (M_{FC}) and zero-field-cooled (M_{ZFC}) magnetization is a function of temperature for higher Cr content alloys, shows divergence below T_c . The divergence

increases with the decrease of temperature and with the increase of Cr content in the amorphous alloys. This effect is associated with the increase of coercivity as the temperature is decreased and controlled by the temperature dependence of magnetic anisotropy energy.

The temperature dependence of magnetization of all the amorphous $\text{Fe}_{73.5-x}\text{Cr}_x\text{Cu}_1\text{Nb}_3\text{Si}_{13.5}\text{B}_9$ ($0 \leq x \leq 17.5$) alloys apparently follows the predictions of Bloch's Spin-wave theory including $T^{5/2}$ term in the temperature range $0.6 \leq \frac{T}{T_c} \leq 0.8$.

The mean-square value of the range of exchange interaction $\langle r^2 \rangle$ and the values of spin-wave stiffness constant (D) decreases monotonically with the increase of Cr content. The values of $\langle r^2 \rangle$ are much smaller than that of crystalline ferromagnet implying that the range of exchange interaction is shorter in amorphous alloys. The smaller values of D in the studied system indicate weakening of the exchange interaction due to an increase in the distance between Fe atoms as the substitution of Fe by Cr occurs.

A linear dependence of D with T_c is observed for the entire composition range, which passes through the origin. The $\frac{D}{T_c} = 0.18$ has been determined from the slope of the

straight line which is much smaller than the crystalline Fe $\left(\frac{D}{T_c} = 0.27 \right)$ and gives further indication regarding the short range nature of interaction in our studied amorphous system as expected.

The metastable nature of amorphous alloys provide the possibility of relaxation of some intrinsic properties like magnetization (M) and Curie temperature (T_c) when heat treated. The magnetization (M) of the amorphous alloys increase with the increase of annealing temperature corresponding to the early stage of crystallization due to irreversible structural relaxation. The room temperature M values for the high Cr content alloys ($x = 12.5, 15 \text{ \& } 17.5$), which are paramagnetic at room temperature are found to increase substantially when annealed below the crystallization onset temperatures. The Curie

temperatures T_c of the amorphous phase of the high Cr content alloys increase with the increase of annealing temperature (T_a) initially and thereafter decrease when annealed at higher temperature close to the crystallization temperature and above. The initial rise of the T_c with T_a is related to the irreversible relaxation of microstructural quantities like long-range internal stress and chemical short-range order. The reduction of T_c values are due to compositional gradients and high degree of chemical disorder with the remaining amorphous phase which is depleted with Fe and subsequent increase of nonmagnetic Nb and Cr in the amorphous (Fe-Nb-Cr)₂B matrix resulting from the initiation of Fe(Si) nanocrystallites. This is to note that the ferro-paramagnetic transition of the samples annealed at higher T_a is more diffused and smeared out from which a unique value of T_c is difficult to estimate. Therefore these T_c values are a rough estimation and should be taken with cautions.

Strong dependence of initial permeability (μ') and relative loss factor $\frac{\tan \delta}{\mu'}$ as a function of annealing temperature (T_a) and Cr concentration is evidenced in the present study. The increase of initial permeability measured at $f=1$ kHz at room temperature is very sluggish up to an annealing temperature, T_a , corresponding to the temperature below the initiation of crystallization. A sharp increase of μ' is observed when the T_a is close to onset of crystallization temperature and above. The μ' passes through a maximum corresponding to the optimum T_a , beyond which μ' sharply falls to a very low value. The relative loss factor $\left(\frac{\tan \delta}{\mu'}\right)$ behave in a reverse way having its minimum value corresponding to maximum value of μ' . All the alloys show similar behavior with the manifestation of good soft magnetic properties i.e. high μ' and low $\frac{\tan \delta}{\mu'}$ corresponding to low Cr content alloys up to $x = 5$ at.% Cr.

An enhancement of initial permeability by two orders of magnitude and a subsequent decrease of relative loss factor have been observed for the optimum annealed samples. This outstanding soft magnetic properties of the studied samples have been achieved due

to averaging out of the magnetic anisotropy energy by exchange interaction between the nanometric Fe(Si) grains with appropriate volume fraction transmitted through thin intergranular amorphous layer. Nanocrystalline FINEMET type of alloys offer the unique opportunity for tailoring ultrasoft magnetic properties that can be technologically exploited for the potential applications in many electronic and electrical devices.

Bibliography:

CHAPTER 1

- 1.1 H. Gleiter, Progress in Materials Science, 33, 223 (1989)
- 1.2 M.E.Mc Henry, S.A. Majetich, De Graef, M. Artman, J.O. and S.W.Staley, Phys. Rev. B, 49, 11358 (1994)
- 1.3 M.E.Mc Henry, M.A. Willard, H.Iwanabe, R.A. Sutton, Z.Turgut, A. Hsiao and D.E.Laughlin, Bull. Mater. Sci., 22, 495 (1999)
- 1.4 D.Appell, "Nanotechnology: Wired for success," Nature (2002)
- 1.5 Judit Kopniczky, " Nanostructures studied by atomic force microscopy", Ph. D Thesis Uppsala University, Sweden (2003)
- 1.6 R.C. O'Handley, Modern Magnetic Materials: Principles and Applications, John Wiley and Sons, New York (2000)
- 1.7 Z. Turgut, M. Q. Huang, K. Gallagher, S. A. Mayelich and M. E. Mc Henry, J. Appl. Phys., 81, 4039 (1997)
- 1.8 Z. Turgut, N. T. Nuhfer, H. R. Piehler and M. E. Mc Henry, J. Appl. Phys., 85, 4406 (1999)
- 1.9 F. W. A. Dirne and M. Brouha, IEEE Trans. Magn, MAG-24, 1862 (1988)
- 1.10 H. J. de Wit, J. Magn. Magn. Mat., 79, 167 (1989)
- 1.11 Y. Yoshizawa, S. Oguma and K. Yamauchi, J. Appl. Phys., 64, 6044 (1988)
- 1.12 Y. Yoshizawa, and K. Yamanchi, Materials Transaction, JIM, Vol. 31, No. 4, 307-314 (1990)
- 1.13 G. Herzer, J. Magn. Magn. Mat., 157/158, 133-136, (1996)
- 1.14 R. Alben, J. J. Becker and M. C. Chi, J. Appl. Phys. 49, 1653-1658 (1978)

CHAPTER 2

- 2.1 W.Klement, R.H.Willens, P.Duwes, *Nature* 187, 869 (1960)
- 2.2 A.L.Greer, *Science*, 267, 1947 (1995)
- 2.3 W.L.Johnson, *Prog. Mater. Sci.* 30, 81 (1986)
- 2.4 H.A.Daveis, in: F.E.Lubrosky (Ed.), *Amorphous Metallic Alloys*, Butterworths, London, P.8. (1983)
- 2.5 S.Kavesh, in: J.J.Gillman, H.L. Leamy (Eds.) *Metallic Glasses*, ASM International, Metals Park, OH, chapter 2 (1978)
- 2.6 D.Turnbull, *Trans. AIME* 221, 422 (1961)
- 2.7 H.S.Chen, D.Turnbull, *J.Chem.Phys.* 48, 2560 (1964)
- 2.8 H.S.Chen, D.Turnbull, *Acta Metall*, 17, 1021 (1969)
- 2.9 D.Turnbull, J.C. Fisher, *J.Chem. Phys.* 17, 71 (1949)
- 2.10 D.Turnbull, *Contemp.Phys.*10, 437 (1969)
- 2.11 W.L.Johnson, *MRS Bull.* 24(10), 42 (1999)
- 2.12 T.D.Shen, R.B.Schwarz: "Bulk ferromagnetic glasses prepared by flux melting and water quenching" *Appl.Phys.Lett.* 75, 49 (1999)
- 2.13 R.C.O'Handley, "Physics of ferromagnetic amorphous alloys," *J.Appl.Phys.* 62, R15-R49 (1987)
- 2.14 Y.Yoshizawa, Ogma, S. and Yamauchi, K. New Fe-based soft magnetic alloys composed of ultrafine grain structure, *J. Appl. Phys.* 64, 6044-6046 (1988)
- 2.15 Y. Yoshizawa and K-Yamauchi; *Mat.Sci. and Engg. A*133, 176-179 (1991)
- 2.16 Y.Yoshizawa, and K-Yamauchi, *Materials Transaction, JIM*, Vol.31, No.4, 307-314 (1990)
- 2.17 G. Herzer, *IEEE Trans.Mag.* 26, 1397 (1990)
- 2.18 G.Herzer, H.Warlimont, *Nanostructured materials*, 1, 263-268 (1992)
- 2.19 A. Makino, A. Inoue, T. Masumoto, *Mat. Trans. JIM*, 36, 924 (1995)
- 2.20 Suzuki, K.Kataoka, N., Inoue, A. and Masumoto, T. High Saturation Magnetization and soft magnetic properties of bcc Fe-Zr-B alloys with ultrafine grain structure, *Mater.Trans. JIM* 31, 743-746 (1990)

- 2.21 Willard, M.A., Laughlin, D.E., McHenry, M.E., Thoma, D., Sickafus, K., Cross, J.O. et al. Structure and magnetic properties of $(\text{Fe}_{0.5}\text{Co}_{0.5})_{88}\text{Zr}_7\text{B}_4\text{Cu}_1$ nanocrystalline alloys, *J. Appl. Phys.* 84 (12), 6773-6777 (1998)
- 2.22 G. Herzer, HR. Hilzinger, *J. Mag. Mag. Mat.* 62, 143 (1986)
- 2.23 G. Herzer, HR. Hilzinger, *Physica, Scripta*, 39, 639 (1989)
- 2.24 G. Herzer, *IEEE Trans. Mag*, 25, 3327 (1989)
- 2.25 G. Herzer, *J. Mag. Mag. Mat.*, 112, 258 (1992)
- 2.26 JMD. Coey, *Rare earth iron permanent magnets*, Oxford Science publications, clarendon press (1996)
- 2.27 EF. Kneller, Hawing. R. *IEEE Trans. Mag*, 27, 3588 (1991)
- 2.28 R. Skomski, JMD. Coey, *Phys. Rev. B*, 48, 15812 (1993)
- 2.29 C.Suryanarayana, *C.Int.Mater Rev.* 40, 41 (1995)
- 2.30 C.Kuhrt, and L. Schultz, *J.Appl.Phys.* 73, 6588-6590,(1993)
- 2.31 R.Birringer, H.Gletier, *Encyclopedia of Materials Science and Engineering*, ed. W.Cahn (Pergamon Press) Suppl.1 p.339 (1998)
- 2.32 Yoshizawa and K. Yamauchi, *Mat. Res. Soc. Symp. Proc.* 232, 183 (1991)
- 2.33 K. Hono and T. Sakurai, *Appl. Surf. Sci.*, 87-88, 166 (1995)
- 2.34 K. Hono, K. Hiraga, Q. Wang, A. Inoue and T. Sakurai, *Acta Metall. Mater*, 40, 2137 (1992)
- 2.35 U. Köster, U. Schönemann, M. Blank-Bewersdorff, S. Brauer, M. Sutton and G. B. Stephenson, *Mat. Sci. Eng. A* 133, 611(1991)
- 2.36 G. Herzer, In: Buschow KHJ, editor, *Handbook of magnetic materials*, Amsterdam: Elsevier Science,10, 415 (1997)
- 2.37 N. Murillo, J. Gonzalez, JM Blanco, JM Gonzalez, *J. Appl. phys.* 79, 5465 (1996)
- 2.38 P. Kwapulinski, J. Rasek, Z. Stoklosa, G. Haneezok, *J. Magn. Magn. Mat.*, 136, 79(1994)
- 2.39 M. Müller, N. Mattern, U. Kühn, *J. Magn. Magn. Mat.* , 157-158, 209 (1996)
- 2.40 M. Müller, N. Mattern, *J. Magn. Magn. Mat.*, 36, 79 (1994)
- 2.41 Zhi Jing, He Kai-yuan, Li-Zhi Cheng, Yu-jun Fu, *J. Magn. Magn. Mat.*, 153, 315-319 (1996)

- 2.42 A. Inoue, K. Kobayashi, J. Kaneira and T. Masumoto, Sci. Rep.Inst. Tohoku Univ. A 29, 331 (1981)
- 2.43 N. Chau, N. X. Chien, N.Q. Hoa, P.Q Niem, N. H. Luong, N.D. Tho, V. V. Hiep, J. Magn. Magn. Mat., 282 174-179 (2004)
- 2.44 M. Ohnuma, D. H. Ping, T. Abe, H. Onodera, K. Hono and Y. Yoshizaqa, J. Appl. Phys. 93, 9186 (2003)
- 2.45 J. Zbroszceyk, H. Fukanaga, J. Olszewski, WH. Ciurzynska, A. Hasiak, J. Magn. Magn. Mat., 160, 277 (1996)
- 2.46 J. Zbroszceyk, K. Narita, J. Olszewski, WH. Ciurzynska, W. Lijun, B. Wyslocki, et al. J. Magn. Magn. Mat.,160, 281 (1996)
- 2.47 J. Zbroszceyk, LK. Varga, J. Olszewski, W. Ciurzynska, B. Wyslocki, S. Szymura, et al. J. Magn. Magn. Mat., 160, 279 (1996)
- 2.48 Maria Neagu, H. Chiriac, M. Lozovan, Sensors and Actuators A 106, 73-75 (2003)
- 2.49 S. C. Yu, K.S. Kim, Y. S. Cho, T. K. Kim, IEEE Trans. Magn. 28, 2421 (1992)
- 2.50 Todd, H. A. Davies, M. R. J. Gibbs, D. Kendall and R. V. Major, Materials Research Society Symposium Proceedings, 577, 492 (1999)
- 2.51 Manh- Huong, Hua-Xin peng, and Michael R. Wisnom, J. Appl. Phys. 98, 014316 (1-6) (2005)
- 2.52 S.H. Lim, W. K. Pi, T. H. Noh, H. J. Kim and I. K. Kang, J. Appl. Phys., 73, 6591 (1993)
- 2.53 A. Zorkovska, J. Kovac, P. Sovak, P. Petrovic, M. Konc, J. Magn. Magn. Mat. , 215-216, 492-494 (2000)
- 2.54 BJ. Tate, BS. Parmar, I Todd, H. A. Davies, MRJ. Gibbs, RV. Mayor, J. Appl. Phys., 83, 6335 (1998)
- 2.55 X-Y Xiong, K-Y Ho, J. Appl. Phys. 77, 2094 (1995)
- 2.56 AR Yavari, PJ Desre. Mat. Sci. Forum, 88-90, 43 (1992)
- 2.57 M.A.Hakim, S.Manjura Hoque, J.Magn.Magn.Mat.,284, 395-402 (2004)
- 2.58 Pritish Kumar Roy, M.Phil.thesis, Khulna University of Engineering & Technology (KUET), Bangladesh (2007)

- 2.59 Saroat Noor, M.Phil.thesis, Khulna University of Engineering & Technology (KUET), Bangladesh (2005)
- 2.60 A.Slawska-Waniewska,M.Gutowski,H.Lachowicz,T.Kulik,H.Matyia.,Phys.Rev.B 46, 14594 (1992)
- 2.61 H.K.Lachowicz, A.Slawska-Waniewska, J. Magn. Magn. Mat., 133, 238 (1994)
- 2.62 Md.Sultan Mahmud,S.S.Sikder and M.A.Hakim, Journal of Science & Arts, 1, 33 (2004)
- 2.63 N.Chau, P.Q.Thanh, N.Q.Hoa, N.D.The, J. Magn. Magn. Mat.,304, 36-40 (2006)
- 2.64 N.Q.Hoa, N.Chau, H.D.Anh, N.H.Luong, M.A.Asgar, S.S.Sikder, Md.Sultan Mahmud, Proceedings of the seventh Vietnamese-German Seminar on Physics and Engineering,Halong City, from March 28 to April 5 (2004)
- 2.65 J.Kovac, O.Dusa, M.Konc, T.Svec, P.Sovak, J. Magn. Magn. Mat., 157/158, 197-198(1996)
- 2.66 D.K.Saha and M.A.Hakim, J. Bangladesh Academy of Sciences, 30, 177-187 (2006)
- 2.67 N.D.Tho, N.Chau, S.C.Yu,H.B.Lee, L.N.D.The, N.Q.Hoa, J. Magn. Magn. Mat., 304, c871-c873 (2006)
- 2.68 N.Chau, N.Q.Hoa,N.H.LuongThe, J.Magn.Magn.Mat., 290-294, 1547 (2005)
- 2.69 F.A.Khan,Suprya Choudhury,M.A.Hakim,S.Manjura Hoque,Nuclear Science and Application,15,58 (2006)
- 2.70 C.Gomez-Polo, J.I.Perez-Landazabal, V.Recarte, P.Mendoza. Zelis,Y.F.Li and M.Vazquez, J.Magn.Magn.Mat., 290-291, 1517-1519 (2005)
- 2.71 N.D.Tho, N.Chau, S.C.Yu, H.B.Lee,L.A. Tuan, N.Q.Hoa, J. Magn. Magn. Mat., 304, c868-c870 (2005)
- 2.72 D.Holzer, I.Perez de Albeniz, R.Grossinger, H.Sassik, J. Magn. Magn. Mat., 203, 82-84 (1999)
- 2.73 A.Lovas, L.F.Kiss, I.Balogh, J. Magn. Magn. Mat., 215-216, 463-465 (2000)
- 2.74 N.Ponpandian, A.Narayanassamy, K.Chattopadhyay, M.ManivelRaja, K.Ganesan, C.N. Chinnasammy and B.Jeyadevan, J.Appl.Phys., 93, 6182 (2003)
- 2.75 D.Prabhu,A.Narayanassamy,K.Chattopadhyay,Journal of Non-cryatalline solids, 353, 1577-1581 (2007)

- 2.76 S.M.Bhagat, M.L.Spano, K.V.Rao, J.Appl.Phys., 50, 1580 (1979)
2.77 E.Pulido, P.Crespo,A. Hernando, IEEE Trans.Magn.28, 3189 (1992)

CHAPTER 3

- 3.1 D.Turnbull, Contemp.Phys.10, 473 (1969)
3.2 H.A.Davies,J.Aucote,J.B.Hull,Nature Phys.Sci., 246, 13 (1973)
3.3 W.L.Johnson, progress in materials science 30, pp.81-134 (1986)
3.4 D.Louca, K.Ahn,V.Ponnambalam and S.J. Poon, Mat.Res.Soc.Proc.Vol.754, pp.CC7.7.1-CC7.7.6.(2003)
3.5 J.W.,Martin,R.D.Doherty,B.Canter,stability of microstructure in metallic systems, Cambridge, UK (1997)
3.6 W.Kauzmann, Chem.Rev.,vol.43,pp.219-256 (1948)
3.7 The IUPAC Compendium of Chemical Terminology, 66, 583 (1997)
3.8 H.Jones Rep.Prog.Phys.36, 1425 (1973)
3.9 D.Turnbull, J.de Physique, 35, C4-1 (1974)
3.10 S.Takayama,J.Materials Sci.11,164 (1976)
3.11 K. Lu, J.T. Wang and W. D. Wei, J. Appl. Phys., 69, 522, (1991)
3.12 H. Y. Tong, J. T. Wang, B. Z. Ding, H. G. Jiang and K. Lu, J. Non-Cryst. Solids, 150, 444, (1992)
3.13 X. D. Liu, J. T. Wang and B. Z. Ding, Scr. Metall. Mater., 28, 59, (1993)
3.14 X. D. Liu and J. T. Wang, Nanostruct. Mater., 2, 63, (1993)
3.15 N. Zarubova, N. Moser and H. Cronmuller, Mater. Sci. Eng. A, 151,205 (1992)
3.16 K. Lu, W. D. Wei and J. T. Wang, Scr. Metall. Mater., 22, 2319, (1990)
3.17 M. L. Sui, L.Y. Xiong, W. Deng, K. Lu, S. Patu and Y.Z. He, J. Appl. Phys., 69, 4451 (1991)
3.18 K. Lu, R. Luck and B. Predel, J. Alloys Comp., 201, 229 (1993)

- 3.19 K. Lu, R. Luck and B. Predel, *Acta. Metall. Mater.*, 42,2303, (1994)
- 3.20 K. Lu, R. Luck and B. Predel, *Scr. Metall. Mater.*, 28, 1387, (1993)
- 3.21 A.Inoue, A.Takeuchi, A.Makino, *Sci Rep RITU*, A42, 143-56 (1996)
- 3.22 XH Lin,WL Johnson,WK Rhim, *Mater Trans JIM*, 38, 473-7 (1997)
- 3.23 R Trivedi, *Mater Sci Eng*, A178, 129-35 (1994)
- 3.24 H.E.Kissinger, *Anal.Chem.*, 29, 1702 (1957)
- 3.25 R.Luck,K.Lu and W.Frantz,*Scrip.Metall.Mater.*, 28, 1071 (1993)
- 3.26 K.Lu.andJ.T.Wang,*Sci.China A* ,35,1266 (1992)
- 3.27 W. Heisenburg, *Z. Phys.* 619 (1928)
- 3.28 S. Chikazumi, *Physics of ferromagnetism-second eddition*, Clarendon Press, Oxford (1997)
- 3.29 G. Bertotti, E. Ferrara, F. Fiorillo, P. Tiberto, *Mat. Sci. Eng. A*, 226-228, 603 (1997)
- 3.30 JMD Coey, *Rare earth iron permanent magnets*, Oxford: Oxford science publications, Clearendon Press, (1996)
- 3.31 G.Herzer,HR.Hilzinger,*Physica Scripta*, 39, 639 (1989)
- 3.32 G.Herzer,*IEEE Trans Mag*, 26, 1397 (1990)
- 3.33 G.Herzer, *Mat.Sci.Eng A* 133, 1 (1991)
- 3.34 G.Herzer,*IEEE Trans Mag*, 25, 3327 (1989)
- 3.35 G.Herzer, *Scripta.Metall.Mater*, 33, 1741 (1995)
- 3.36 R.,Alben,J.J.Becker and M.C.Chi,*J.Appl.Phys.* 49, 1653 (1978)
- 3.37 R.,Schafer,A.Hubert and G.Herzer, *J.Appl.Phys.*, 69, 5325 (1991)
- 3.38 G. Herzer, “Nanocrystalline soft magnetic alloy” in *Hand book of Magnetic Materials*, chap. 3 vol.8, ed, K.H.J Buschow (Elsevier Science B. V. pp 417-483, (1997)
- 3.39 Z. Stoklosa, P. Kwapulinski, G. Haneczok, J. Rasek, *J. Phys. IV* 8, pp 51, (1998)
- 3.40 Y. Yoshizawa, S. Oguma and K. Yamauchi, *J. Appl. Phys.* 64 6044, 6047, (1988)
- 3.41 F.Keffer,in:*Ferromagnetism*,ed.H.PJ.Wijn(Springer,Berlin),Vol.XVIII,2,p.1 (1966)
- 3.42 C.L.Chien and R.Hasegawa, *Phys.Rev.B*16, 2115 (1977)
- 3.43 R.W.Cochrane and G.S.Cargill, III, *Phys.Rev.Lett.*32, 476 (1974)

- 3.44 S Ramasamy, Leif Lundgren, K Ganesan and Narayanasamy, *J. Phys. F: Met. Phys.*, 17, 753-765 (1987)
- 3.45 N. Ponpandian, A. Narayanasamy, K. Chattopadhyay, M. Manivel Raja, K. Ganesan, C.N. Chinnasamy and B. Jeyadevan, 93, 6182 (2003)
- 3.46 K. Handrich, S. Kobe: *Amorphe Ferro-und Ferrimagnetica*, Akademie-Verlag Berlin, Germany (1980)
- 3.47 S.M. Bhagat, M.L. Spano and K.V. Rao, *J. Appl. Phys.* 50 (3), 1580 (1979)
- 3.48 S.N. Kaul, *J. Magn. Magn. Mat.*, 53, 5 (1985)

CHAPTER 4

- 4.1 JMD Coey and H Sun, *J. Magn. Magn. Mater.*, 87, L251 (1991)
- 4.2 K Schnitzke, L Schultz, J Wecker and M Katter, *Appl. Phys. Lett.*, 57, 2853 (1990)
- 4.3 M Endoh, M Iwata and M Tokunaga, *J. Appl. Phys. Lett.*, 70, 6030 (1991)
- 4.4 M Katter, J Wecker and L Schultz, *J. Appl. Phys.*, 70, 3188 (1991)
- 4.5 C N Christodoulou and T Takeshita, *J. Alloys & Comp.*, 196, 161 (1993)
- 4.6 PJ McGuinness, XJ Zhang, H Forsyth and IR Harris, *J. Less-Common Met.*, 162, 379 (1990)
- 4.7 B Gebel, M Kubis and K-H Muller, *J. Magn. Magn. Mat.*, 174, L1-L4 (1997)
- 4.8 MQ Huang, LY Zhang, BM Ma, Y Zbeng, JM Elbicki, WE Wallace and SG Sankar, *J. Appl. Phys.*, 70, 6027 (1991)
- 4.9 T Takeshita and R Nakayama, *Proc. 11th Int. W'shop on RE Magnets & their Appl.*, 49 (1991)
- 4.10 Pungor, Erno. *A Practical Guide to Instrumental Analysis*. Boca Raton, Florida. pp. 181-191 (1995)
- 4.11 Dean, John A. *The Analytical Chemistry Handbook*. New York. McGraw Hill, Inc. pp. 15.1-15.5 (1995)
- 4.12 Skoog, Douglas A., F. James Holler and Timothy Nieman. *Principles of Instrumental Analysis*. Fifth Edition. New York. pp. 905-908 (1998)

- 4.13 B.D. Cullity, Elements of X-ray diffraction, Reading, MA:Addision-Wesley,(1972)
- 4.14 Foner, S., Rev. Sci. Instr., 30, 548 (1959)
- 4.15 Foner, S., Rev. Sci. Instr., 27, 578 (1955)

CHAPTER 5

- 5.1 M.E. McHenry, M. A. Willard and D. E. Laughlin, Prog. Mat. Sci. 44, 29-433 (1999)
- 5.2 S. Manjura Hoque, M.A Hakim, F.A. Khan, N. Chau, Mat. Chem. Phys. 101, 112-117 (2007)
- 5.3 D. K. Saha & M. A. Hakim, Jornal of Bangladesh Academy of Sciences, vol. 30, no. 2, 177-187 (2006)
- 5.4 Y.Yoshizawa and K.Yamauchi, Mat. Res. Soc .Symp. Proc., 183 (1991)
- 5.5 Manfred.Muller,N.Mattem and L.Illgen,Z.Metallkde, 82, 895 (1991)
- 5.6 Tadeusz.Kulik,Mater.Sci.Eng. A 159, 95 (1992)
- 5.7 K.Hono, K.Hiraga, Q.Wang, A.Inoue and T.Sakurai,Acta Metall.Mater, 40, 2137 (1992)
- 5.8 P.Gorria, V.M.Prida, M.Tejedor, B.Hanando, M.L.Sanchez,Physica B 299, 215-224 (2001)
- 5.9 H.Kissinger, Anal.Chem., 29, 1702-1706 (1957)
- 5.10 N. Chau, N. X. Chein, N. Q. Hoa, P. Q. Niew, N. H. Luong, N. D. Tho, V. V. Hiep, JMM 282, 174-179 (2004)
- 5.11 A. M. Tonejc, N. Ramsak, A. Prodan, A. Tonejc, A Khalladi, S. Surinach, M. D. Baro, Nanostructureed Materials, 12,677-680 (1990)
- 5.12 A.Rosales-Rivera, V.H.Valencia, D.L.Quintero, P.Pineda-Gomez, M.Gomez, Physica B 384,169-171 (2006)
- 5.13 P.Marin, M.Lopes, Hernando, Y.Iqbal,M.A.Davies, M.R.J.gobs., J.Appl. Phys., 92, 374 (2002)

- 5.14 M.A.Hakim, S.Manjura Haque, J. Magn. Magn. Mat. 284, 395-402 (2004)
- 5.15 D.K.Saha, M.A.Hakim, J.Bangladesh Academy of Science, 30, 177-187 (2006)
- 5.16 A.Lovas, L.F.Kiss, I.Balogh, J. Magn. Magn. Mat. 215-216,463-465 (2000)
- 5.17 D.Holzer, I.Perez de Albeniz,R.Grossinger,H.Sassik, J. Magn. Magn. Mat. 203, 82-84 (1999)
- 5.18 M.A.Hakim. Nuclear Science and Application, 13, 36-43 (2004)
- 5.19 S. Chikazumi, Physics of Magnetism, New work: Willey P. 273 (1964)
- 5.20 L. Neel, Ann. Phys. (Paris), 18, 1 (1932)
- 5.21 P. J. Wojtcwicz and M. Rayl, Phys. Rev. Lett: 20, 1489 (1968)
- 5.22 I.Maartense and G.Williams, J.Phys.F: Metal Phys.6L 121-6, 2363 (1976)
- 5.23 A. Arrott Phys. Rev., 108, 1394 (1957)
- 5.24 K.P.Belov, Magnetic transitions, Consultants Bureau, New York (1961)
- 5.25 J.S, Kouvel and M.E.Fisher, Phys.Rev.,136 A, P.1626 (1964)
- 5.26 K.Knobel, J.P.Sinnecker, R.Sato Turteli, N.R.Rechenberg, R.Grossinger, J. Appl. Phys., 73, 6603-6605 (1993)
- 5.27 A. Zorkovska, J. Kovac, P. Sovak, P. Petrovic, M. Konc, J. Magn. Magn. Mat. , 215-216, 492-494 (2000)
- 5.28 J.Kovac, O.Dusa, M.Konc, T.Svec, P.Sovak., J. Magn. Magn. Mat. , 157/158, 197-198 (1996)
- 5.29 R.Krishnan, M.Dancygier, M.Tarhouni., J.Appl.Phys.,63,7768 (1982)
- 5.30 K.Inomata, M.Hasegawa,S.Shimanuki,IEEE.Trans.on Mag.Mag.17,3076 (1981)
- 5.31 P.S.A. Kumar, P.A. Joy, S.K. Date, J. Phys. Condens. Matter, 10, L 487 (13) (1998)
- 5.32 P.S.A. Kumar, P.A. Joy, S.K. Date, Bull. Mater Sci. 23, 101 (2000)
- 5.33 C. L. Chien, and R. Hasegawa, Phys. Rev. B16, 2115 (1977)
- 5.34 K. Handrich, S. Kobe, Amorphe Ferro and Ferrimagnetica, Akademie- Verlag Berlin, Germany (1980)
- 5.35 N. Ponpandian, A. Narayanasamy, K. Chattopadhyay and M. Manivel Raja, J. Appl. Phys. 93, No. 10, 6182 (2003)
- 5.36 S. M. Bhagat, M. L. Spano and K. V. Rao, J. Appl. Phys. 50(3), 1580 (1979)

- 5.37 S. N. Kaul, *Phys. Rev. B* 24(11), 6550 (1981)
- 5.38 S. Ramasamy, Leif Lundgren, K Ganesan and A Narayanasamy, *J. Phys. F: Met Phys.* 17, 753-765 (1987)
- 5.39 L. K. Varga, F. Mazaleyrat, J. Kovac, and A. Kakay, *Mat. Sci. Engg. A*, 304-306, 946 (2000)
- 5.40 E. Pulido, P. Crespo and Hernando, *IEEE Transactions on Magnetics*, 28, 3189 (1992)
- 5.41 D. Prabhu, A. Narayanasamy, K. Chattopadhyay, *Journal of Non-Crystalline Solids*, 353, 1577-1581 (2007)
- 5.42 Kyeong-Sup Kim, Seong-Cho Yu, Suhk-Kum Oh, Yong-Soocho, Taik-Kee Kim, *JMMM* 133, 283-286 (1994)
- 5.43 K. S. Kim, S. C. Yu, K. Y. Kim, T. H. Noh and I. K. Kang, *IEEE Trans. Magn.* 29, 2679 (1993)
- 5.44 A. E. Berkowitz, J. L. Walter, K. F. Wall, *Phys. Rev. Lett.* 46, 1484-1487 (1981)
- 5.45 J. Bigot, N. Lecaude, J. C. Perron, C. Milan, C. Ramiarinjaona, J. F. Rialland., *J. MMM*, 133, 299-302 (1994)
- 5.46 Anh-Tuan Le, Chong-Oh Kim, N. Chau, N. D. Cuong, N. D. Tho, N. Q. Hoa, Heebok Lee, *J. Magn. Magn. Mat.*, 2007 (in press)
- 5.47 A. Blachowicz, J. Zbroszczyk, J. Olszewski, W. H. Ciurzynska, H. Fukanaga, K. Narita, B. Wyslocki, M. Hasiak, *J. Magn. Magn. Mat.*, 215-216, 422-424 (2000)
- 5.48 I. Skorvanek, J. Kovac, J. Kotzler, *Phys. Stat. Solidi (b)* 236, 303-309 (2003)
- 5.49 I. Skorvanek, J. Kovac, J. M. Greneche, *J. Phys. Condens. Matter*, 12, 9085 (2000)
- 5.50 L. K. Varga, K. V. Rao, *NanoStructured Materials.*, 12, 1157-1160 (1999)